External cavity diamond Raman lasers for high-power continuous-wave beam conversion

By

Ondřej Kitzler

A thesis submitted to Macquarie University
for the degree of
Doctor of Philosophy
Department of Physics
November 2014

MACQUARIE
UNIVERSITY
FACULTY OF SCIENCE

Typeset in LaTeX 2$_\varepsilon$.

This thesis is submitted in fulfilment of the requirements of the degree of Doctor of Philosophy at Macquarie University and has not been submitted for a higher degree to any other university or institution. I certify that, to the best of my knowledge, all sources used and assistance received in the preparation of this thesis have been acknowledged. This thesis does not contain any material which is defamatory of any person, form or corporation and is not in breach of copyright or breach of other rights which shall give rise to any action at Common Law or under Statute.

Ondřej Kitzler

Acknowledgements

I would like to express my profound gratitude to the various persons who supported me in one way or another during my PhD candidature. Without their care and assistance, this would not have been as enjoyable a journey as it has been.

First and foremost to my supervisor Rich Mildren: thank you for giving me this opportunity and for your great guidance and support during my PhD. The freedom you gave me in formulating our goals and designing experiments significantly expanded my research skills and knowledge, which I will value for years to come. I would like to thank my Postdoc and a great friend Aaron McKay for always being ready to help me in the lab, read and correct my writing and discuss all the everyday issues. I have particularly relished the friendly and stimulating discussions with both of you during our lunches in Oporto.

I would also like to thank other academics from the department, namely Brian, Dave and Dave, David, Deb, Helen, Jim, Judith, Mike and Mick for creating a very friendly and stimulating environment here at Macquarie. Special thanks to Judith and Mick for always supporting the OSA Student Chapter outreach activities I had the pleasure to be part of. I am also grateful to administrative staff Carol, Laura, Lisa and Liz for their support and help with paperwork and Walter and his cohort from METS for creating the bits and pieces necessary for my experiments from my sloppy drawings.

To all my office mates and friends I have met here in Australia I am infinitely indebted. It would have not been so much fun without the Friday footy, Wednesday soccer, Oztag, weekend hikes, canyoning, surfing, BBQs and beers, and games nights. So thank you Adam, Ali, Alex, Andy, Anne, Annemarie, Barbara, BJ, Christine, Chris, Dennis, Dough, Gerald, Graham, Guido, Henrique, Huwa, Iza, Jacob, Jana, Jipeng, Jocelin, Josh, Katja, Marty, Nem, Nick, Paul, Peter, Rob, Simon, Thom, ThanhPhong, Tim, Tristan, Varun, Vincent and Zach.

I would like to sincerely thank my family. Mum, Dad I love you for raising me and your continuous support. Your trust and encouragement are invaluable for me. Martin, thanks for being such a great brother!

Finally, I wish to thank may lovely girlfriend Monika. Thank you for loving me even over such a great distance. Thank you for always supporting my stupid ideas. Thank you for being here for me, the life with you is beautiful.

This project was supported by the Australian Research Future Fellowship (FT0990622) and Discovery Grant (DP130103799) Schemes, the US Air Force Research Laboratory (FA2386-12-1-4055) and Macquarie University.

To all friends from Beer o'clock.
Cheers!

Abstract

Solid-state Raman lasers represent a convenient way of shifting the output of lasers to longer wavelengths with enhanced brightness. In the continuous-wave (CW) regime, the conversion is challenging due to the inherently low gain of the third-order nonlinear process. High pump intensities are needed to reach threshold, and thus many CW Raman lasers utilize cavity architectures in which the pump and Stokes beams are resonated. However, the power-scaling of such devices becomes challenging due to thermal effects in the Raman medium and potentially other intra-cavity elements.

This thesis presents a novel approach to the power-scaling problem. It is shown that a combination of optical quality diamond with an external-cavity Raman oscillator design enables efficient CW Raman conversion and high-power output. Diamond Raman lasers (DRLs) were studied under continuous and quasi-continuous-wave high-power pumping using conventional Nd and Yb laser technologies. A fourfold increase in output power of crystalline Raman lasers (up to 22 W) was achieved with a good conversion efficiency (45% optical-to-optical), and the first demonstration of a fibre laser pumped DRL is also presented.

Theoretical models were derived in order to describe the DRL performance. The models were used to determine optimization procedures to maximise power and efficiency as a function of design variables of the laser cavity, pump laser, and diamond size and quality. Diamond polarization properties, in particular the birefringence, were found to be crucial to achieving efficient and predictable performance. The models were also used to predict design when scaling output power and to determine performance limiting factors.

The investigated DRL architecture was found to be well suited for the examination of the fundamental aspects of frequency broadening in Raman lasers. A DRL was investigated using a single-frequency fibre laser system as the pump laser. The observed laser dynamics, which include some unexpected observations of amplitude and frequency instabilities, highlight some key areas for future development of stimulated Raman scattering theory.

This study of power-scaling of Raman lasers shows that the developed DRL systems have the potential to operate efficiently with any high-power high-spectral-density laser technology. The superior thermal properties of diamond make the design constraints more flexible and help to mitigate loss mechanisms. This thesis shows that there are excellent prospects for highly efficient operation when power scaling well-beyond the 100 W level, and greatly narrowing the power gap between Raman lasers and other high-power laser technologies.

Contents

1 Introduction

Throughout the 50 years of laser development a broad family of gases, liquids and solids have been used as laser active media. Dye lasers are still used in spectroscopy due to their very broad wavelength tuning range. Gas CO_2 lasers are frequently used in industrial applications for cutting and welding, and the helium-neon laser remains popular for alignment of optics, interferometers and also serves as an optical frequency standard. Due to the practical difficulties with handling fluids the focus is continually shifting towards solid-state technologies. In an attempt to find the ideal material, the lasing properties of many crystals, ceramics and glasses doped with active rear-earth or transition metal ions [1] have been investigated. However, only a small number of these have found their way into widespread use and commercial products. The best known are neodymium-doped YAG, YVO_4, YLF and glass; ytterbium-doped YAG and glass; erbium and thulium-doped YAG and glass; and titanium-doped sapphire [2]. The main advantages are their low production and maintenance costs, the ability to generate high average and peak power and brightness, and in some cases wide tunability (Ti:Sapphire and Yb lasers).

Lasers operate over a massive range of timescales, offering pulse durations from less than a femtosecond up to continuous wave (CW) output. Lasers providing long pulses or CW output are often necessary for applications requiring large quantities of photons over time without necessarily high peak intensities. CW lasers are also often more convenient for generating highly monochromatic radiation. Therefore, CW lasers are in demand for a host of applications such as materials processing, spectroscopy, atom cooling, directed energy, interferometry, and surgical and medical treatments. However, the laser wavelengths that best suit an application often lie outside the emission spectrum of mature laser technologies. The output wavelengths of solid-state lasers, which are dictated by the limited choice of effective fluorescent dopant ions, are mainly restricted to a few choices in the vicinity of 1 µm (Nd, Yb), 1.5 µm (Er), and 2 µm (Tm), especially for lasers generating high average power and high brightness. Therefore nonlinear frequency conversion is of major interest for broadening the wavelength coverage of CW lasers.

Harmonic generation uses the second-order ($\chi^{(2)}$) nonlinearity of crystals to generate shorter wavelengths in the visible and ultraviolet parts of the spectrum. Conversion to longer wavelengths is achieved using parametric conversion schemes such as optical parametric oscillators (OPOs) and Raman lasers. In OPOs, pump photons are split into two photons (called the signal and the idler) in a χ^2 nonlinear medium with an energy sum equal to the input pump photon. The energy ratio (and thus the wavelengths) and conversion efficiency are defined by the phase-matching condition in which the

complex amplitudes of the waves interact in phase to achieve efficient coupling. The OPO output wavelengths are continuously tunable as phase-matching is continuously tuned by, for example, varying incident angles or temperature. Various OPO laser systems cover the optical spectrum from the ultraviolet to the mid-infrared with CW output power up to about 25 W [3–5].

Raman lasers utilize the third-order ($\chi^{(3)}$) nonlinear interaction of a pump laser with phonon vibrations of the Raman media, to generate an output Stokes beam. The three waves have to interact in phase, as in OPOs; however, because momentum is readily conserved through the material vibration, the process is automatically phase-matched [6]. This important characteristic of Raman lasers enables designs to be simplified, more robust and with relaxed constraints on thermal management. The wavelength shift is defined by the natural frequency of the material's phonon oscillations, which is typically around 1000 cm^{-1} for crystals. By cascading the nonlinear interaction, Raman lasers are able to generate multiple wavelengths in discrete steps separated by the Raman shift. A further important consequence of automatic phase-matching is the ability for Raman lasers to bring about an improvement in the beam quality of the incoming beam. One disadvantage of Raman lasers, however, arises due to the inevitable decay of the generated phonons into heat. Thus thermal effects are important considerations in high power Raman laser design.

1.1 Review of CW Raman laser technologies

Being a third-order nonlinear interaction, attaining threshold in Raman lasers generally requires large field intensities. In order to reduce threshold the CW pump field is generally either resonated together with the Stokes field, as utilized in intracavity and resonantly-enhanced pump Raman lasers, or the interaction length is long as in Raman fibre lasers.

Raman laser designs can be divided into the categories shown in Fig. 1.1. The lasers are arranged according to the degree of separation between the inversion and Raman gain processes. Gas Raman lasers are mostly resonantly-pumped systems due to the low Raman gain coefficient [7], and fibre Raman lasers can be considered externally pumped [8]. Crystalline Raman lasers, however, can fall into any of these categories [9, 10].

Self-Raman lasers consist of crystals (or glass) that have a high Raman gain and are doped with laser active ions and placed in a cavity resonant for both the fundamental and Stokes wavelength [11]. They benefit from a monolithic design and thus a small footprint, inherent stability and robustness. On the other hand, power-scaling is limited due to the combined heat load caused by the quantum defects of the inversion and inelastic Raman scattering. The material choice, and therefore the available Raman shift, is also limited as not all Raman crystals are suitable hosts for laser active ions. In many cases the Stokes field is out-coupled via harmonic generation or frequency mixing, resulting in output in the lime-yellow-orange spectral region [12–14]. Self-Raman conversion has also been used to generate radiation at the sodium resonance

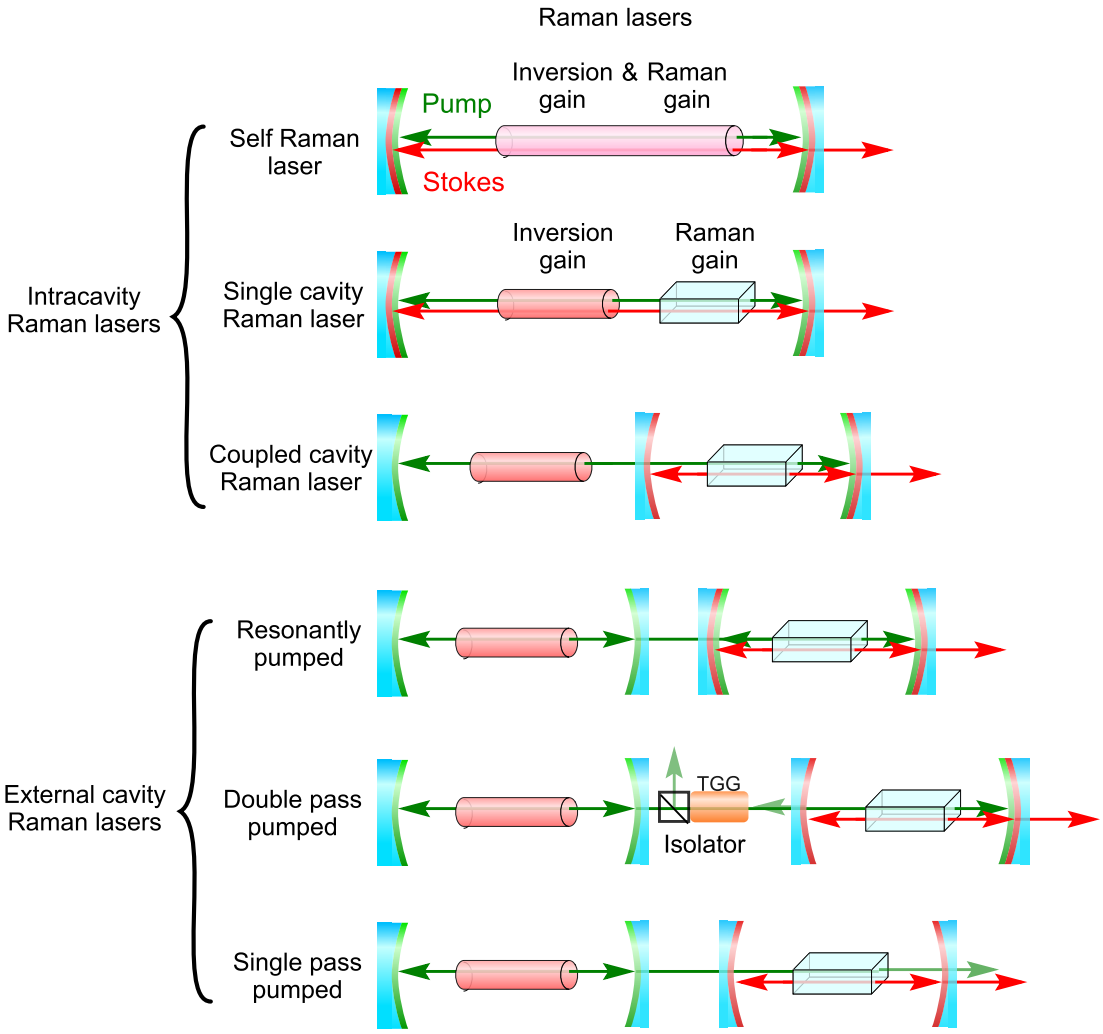

Figure 1.1: Different configurations and pumping schemes of Raman lasers. The mirror coating color, green and red, corresponds to high reflectivity at respective pump and Stokes wavelength.

line at 589 nm [15].

The heat load is better distributed for separated Raman crystal [9, 16–18]. Lasers based on this configuration and using various Raman crystals have been demonstrated with several watts of visible output power [19–21]. Due to the increased number of permutations of Raman crystals and laser media, the range of accessible wavelengths is broader than for self-Raman lasers. However, thermal lensing in the laser and Raman crystal forms a dynamic system that requires careful balancing, and places some restrictions on the cavity design and maximal power, hence the output powers have been limited to approximately 5 W [10, 22, 23].

The interaction between the fundamental and Raman gain media is further reduced in the case of the so-called external cavity Raman laser. Whereas pulsed pumping has been investigated in detail [10, 23], the development of CW-pumped external cavity Raman lasers has proved to be challenging. In order to reduce the threshold to values

accessible by common CW lasers (below 10 W), strong focusing, low intra-cavity loss, and low output-coupling are essential. Grabtchikov et al. [24] and Lisinetskii et al. [25] first demonstrated a CW Raman conversion in external cavity setup. A $Ba(NO_3)_2$ crystal, which had the highest Raman gain amongst the readily available crystals at the time, was pumped by a green argon-ion laser emitting at 514 nm in order to reduce lasing threshold. However, even when operated at double the threshold of 2.5 W, the output power was only 164 mW, yielding a conversion efficiency of 3.3%. Severe thermal loading prevented any further increase in power and efficiency. The only second example is a continuously-pumped silicon waveguide laser [26]. In this case, losses due to two-photon-induced free-carrier absorption limited the output power to only about 10 mW, with 1.5% conversion efficiency.

Another method which substantially reduces the threshold, but adds significant complexity, is by resonantly-enhanced pumping. When a high-finesse cavity, resonant for the pump and Stokes wavelengths, is frequency-locked to a single-frequency pump laser, the pump field builds up in the resonator increasing to up to several orders of magnitude, thus providing the intensity needed to reach the Raman lasing threshold. This technique has been demonstrated to reduce the threshold to the 10 mW level in gaseous Raman media, but has not been widely used due to its intricacy . Brasseur, Repasky, Roos and Carlsten demonstrated a H_2 and D_2 Raman laser pumped by a conventional Nd:YAG laser [7, 27–29] and directly by a diode laser [30]. The output power of these devices was at the several mW level. In deuterium, higher power operation up to 300 mW has been reported by Green et al. [31].

Raman fibre lasers are a technology combining the robustness and high power of fibre lasers with Raman scattering in mostly silica glass. Due to optical confinement over long distances, thresholds are reduced; however, the main focus of research to date has been on amplification of telecommunications signals and laser generation in the mid-infrared [3]. As in inversion fibre lasers, the heat distribution over a long length has allowed up to 150 W and 301 W of CW Stokes output to be demonstrated [8], [32], respectively. However, substantial linewidth broadening at elevated power levels prevents efficient harmonic conversion to the visible spectrum. A frequency-doubled Raman fibre laser has been demonstrated generating 3 W at 589 nm [33]. The linewidth of the Stokes output increased from 22 to 85 GHz over the Stokes output power range from 5 to 25 W. Since the Raman shift in glass fibres is shorter than in crystals ($400 - 600\,cm^{-1}$), the cascaded Stokes orders are more closely spaced. A cascaded Raman fibre laser with subsequent frequency-sum mixing was demonstrated with output at six visible wavelength from 550 to 625 nm [34]. The power, however, was only a few milliwatts. Other advanced glasses, such as GeO_2 pumped by Tm lasers, have been used to convert laser radiation in the 2 μm region at watt level powers [35].

A relatively recent concept is stimulated Raman scattering in gas filled hollow core photonic crystal fibres. Output powers in the first Stokes component have reached 55 W [36], which contrasts with the resonantly pumped gas Raman lasers with milliwatt output. Although this technology is likely to suffer from many of the usual impracticalities of gas handling, there is a significant potential for investigating of a variety of nonlinear interactions including stimulated Raman scattering [37, 38].

1.2 The route to CW high power Raman conversion

An external cavity, singly-resonant Raman architecture is a highly attractive concept as it is applicable to a large selection of mature and off-the-shelf CW solid-state lasers including high power Nd and Yb doped crystalline and fibre lasers.

The use of crystalline Raman media is desired because of their higher Raman gain coefficients compared to gases and glass (see Tab. 1.1) and smaller spectral broadening then in fibres [23]. However, thermal problems in conventional molecular-ion crystals (and two-photon-induced free-carrier absorption in the case of silicon) hinders efficient Raman conversion at high powers [25, 39]. The tight focusing needed to reach a moderate lasing threshold results in strong thermal lensing in conventional Raman crystals and prevents efficient Raman conversion [24]. Therefore, in order to substantially increase output power, the requirements on the Raman crystal are high Raman gain, high damage threshold and excellent thermal properties, especially thermal conductivity and thermal expansion [40].

Table 1.1: Physical and Raman properties of selected materials [7, 10, 41].

	Gas (H_2, D_2)	Molecular xtals (WO_4, VO_4, NO_3)	Bulk glass (SiO_2, GeO_2)	Group IV Silicon	**Diamond**
Raman gain coeff. @ 1064 nm [cm/GW]	1	4–10	0.01–0.1	15	**10**
Material length [cm]	7	1–5	3000	4	**1**
Thermal cond. [$Wm^{-1}K^{-1}$]	0.2	5–10	1	150	**2000**
dn/dT [$10^{-6}\,K^{-1}$]	-4	-20–10	8	215	**15**
Transp. range [µm]	broad	0.3–5	< 2.5	1–6	$>$ **0.23**
Raman shift [cm^{-1}]	4000	400–1000	400–600	521	**1332.3**
FoM (1.1)	≈0.04	≈2–40	≈5–50	≈70	≈**760**

1.3 Diamond properties

Diamond, the most famed and fabled of all gemstones, is unique in many ways. Renowned for being the hardest substance on earth, its durability, and "inner fire" has captivated people's imagination since ancient times. Until only recently, however, the rarity of natural diamond limited its use in science to only a few niche applications, such as microscope lenses and spacecraft windows [42].

The chase for artificial synthesis of diamond was a dream similar to the search for the Philosophers' Stone. The supposedly first successful synthesis in 1880 by J. B. Hannay [43] could not be repeated under the conditions he described. Diamonds produced by Sir Ch. A. Parsons in 1888 were not preserved, and thus could not be confirmed by the later-developed X-ray diffraction techniques. Samples synthesized by H. Moissan in 1893 were similarly lost [44]. There is a strong belief based on an X-ray powder diffraction measurement that C. V. Burton in 1905 first successfully prepared synthetic diamond [45]. However, the first reproducible experiment in diamond synthesis was reported in 1955 by the General Electric Company [46].

Today the extreme properties of artificial diamonds are harnessed in a large variety of applications, from cutting and drilling tools reinforced by micro-diamonds, to advanced detectors in particle accelerators [47]. In optics the focus is shifting from diamond windows [48–50] and lenses [41, 49, 51] towards cutting-edge quantum and nano-sensing technologies [52].

In lasers, the two order-of-magnitude higher thermal conductivity of diamond compared to most other optical materials makes it well suited for effective heat dissipation, and the wide transparency range allows its use as optical elements across many parts of the spectrum [41, 51]. Incorporation of rare-earth laser ions into diamond is problematic, however, due to the extremely dense lattice [53] (diamond being the most dense lattice known to man [41]), and lead to deteriorated optical properties at large doping concentrations. Laser action in diamond using stimulated Raman scattering currently represents a more viable approach.

Although Raman scattering has been observed in diamond as early as 1963 [54], poor optical quality of available natural and synthetic diamond prevented its use as a practical Raman laser material. In the last decade, however, advances in synthesis techniques have led to the manufacturing of single-crystal (SC) diamond slabs of length one centimetre or more [50], with quality that is in many ways higher than what can be found in nature.

It is the combination of high Raman gain and excellent thermal properties that sets diamond apart (see Tab. 1.1 for comparison). The Raman gain is amongst the highest observed in crystals, and the thermal conductivity of $2000\,\mathrm{Wm^{-1}K^{-1}}$ at room temperature is second only to graphene [55] amongst all materials known to man. Together with a small thermal expansion coefficient and moderate thermo-optic coefficient, these characteristics greatly reduce the severity of thermally-induced effects. For example, the thermal fracture limit is a critically important parameter. Adopting a formula for the stress fracture limit for an end-pumped crystal [40], the critical amount of heat which can be deposited into diamond is $\mathrm{P_{limit}} = 1$ MW [41], which is four orders of magnitude higher than YAG (<100 W) in an end-pumped rod configuration [56] .

One way to gain an approximate measure of the relative ability of a material to power scale is to use figure of merit (FoM) as derived by Lubeigt et al. [57]. The thermal lens strength in a Raman medium is proportional to the heat deposited due to the Raman shift $\Delta\lambda$ and thermo-optic coefficient $\mathrm{d}n/\mathrm{d}T$ and is inversely proportional to the thermal conductivity K and beam area S. The lasing threshold is proportional to the mode size S and inversely proportional to the gain coefficient g_r and crystal

length l. The FoM defined as

$$\mathrm{FoM} = \left| \frac{K g_r l}{\frac{\mathrm{d}n}{\mathrm{d}T} \Delta\lambda} \right|, \tag{1.1}$$

which is inversely proportional to the thermo-optic induced lens strength for a given heat load. A comparison of diamond with other important Raman media given in Tab. 1.1 shows that diamond has a FoM 760, or 10-20 times larger than other crystals. Interestingly, a FoM of silicon has similar value to glass, due to its high thermal conductivity. The potential for power-scaling is impaired, however, by the two-photon-induced free-carrier absorption.

The estimated potential of individual CW Raman technologies for power-scaling is summarized in Fig. 1.2. Gas-based systems are relatively sophisticated systems requiring single-frequency pump sources, frequency locking, pressure management and handling of gaseous media. However, the very narrow single-frequency operation is desired in many spectroscopic applications where output power is not essential. Solid-state Raman lasers are relatively simple devices with a small footprint and with potential for delivering higher output power. Raman fibre lasers have excelled in output power to date (up to 301 W [32]), but exhibit substantial frequency broadening (unless actively managed) due to the broad inhomogeneous Raman linewidth and due to frequency mixing processes [58]. In some applications, the spectral width of the generated laser radiation is less important than the output power. However, applications such as atom cooling, guide stars, and long distance ranging are examples where substantial laser power at narrow, specific wavelengths is necessary and for which external CW diamond Raman technology is more suitable.

1.4 Diamond Raman lasers

Maturing of single-crystal diamond synthesis has sparked new interest from laser scientists. Since the emergence of good quality material since 2005, several different diamond Raman lasers have been reported to date.

1.4.1 Pulsed pumping

The first observation of stimulated Raman scattering in synthetic diamond of nanosecond and picosecond pulses is attributed to Kaminskii et al. [59, 60]. A total of 45% energy conversion from the pump to up-to four Stokes components was obtained.

To exploit the naturally-higher Raman gain at shorter wavelengths, Mildren et al. focused the second harmonic output of a Q-switched Nd:YAG laser (at 532 nm) into an external diamond Raman cavity [61, 62]. The output power increased linearly with a 75% slope efficiency up to 1.2 W. With conversion efficiency of 63.5%, the diamond Raman laser took its place alongside the most efficient Raman converters. A year later, Sabella et al. [63] demonstrated nearly quantum limited (84%) conversion and 2 W of

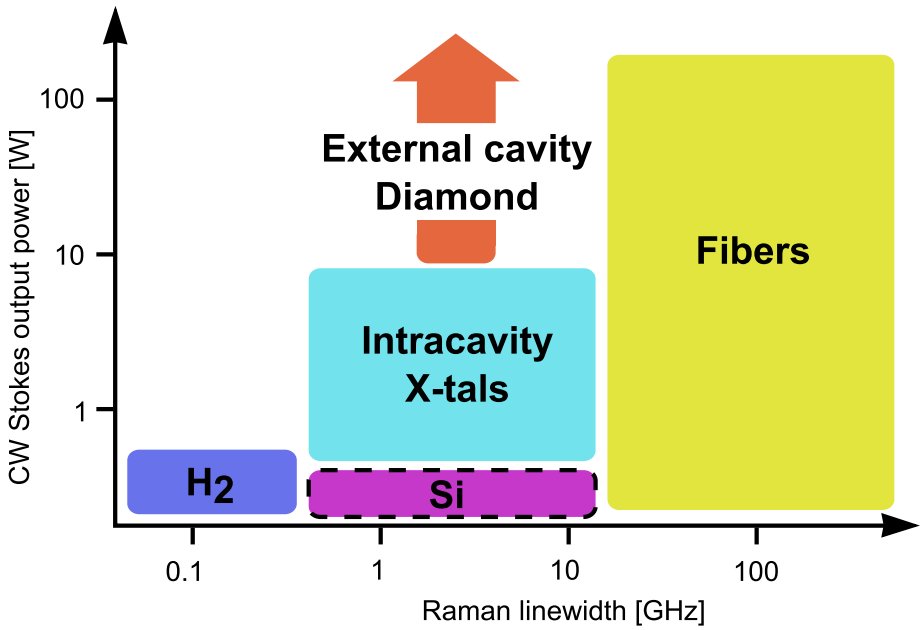

FIGURE 1.2: Comparison of CW Raman laser technology as functions of Raman linewidth and output power. External cavity DRLs are promising for increasing the power capabilities of crystal Raman converters to the level currently obtained using Raman fibres.

output power at 1240 nm. A pulsed diamond Raman laser, employing the intracavity design, was also investigated by Lubeigt et al. [64]. The generated wavelengths were further extended to "eye-safe" wavelengths (1485 nm Sabella et al. [65] and 1630 nm Jelinek et al. [66]) and to mid-IR [67].

On the short-wave side of the spectrum, pulsed operation of a diamond Raman laser in the deep-UV was investigated by Granados et al. [68]. The diamond was synchronously-pumped by the fourth harmonic of a mode-locked Nd:YVO_4 laser. The maximal pulse energy of 1 nJ was limited only by the available pump power.

Picosecond Raman scattering and pulse shortening in diamond has been demonstrated by Spence et al. [69]. A mode-locked 532 nm laser with 26 ps pulse duration synchronously-pumped an external cavity diamond Raman laser. The average output power reached up to 2.2 W with pulse durations of 21 ps at the yellow wavelength of 573 nm. By varying the cavity length, the pulse duration was decreased to a minimum of 9 ps.

1.4.2 High average power operation

Power scaling of pulsed diamond Raman lasers and possible cryogenic operation has been investigated by Feve et al. [70, 71]. The total output power from both ends of the Raman cavity summed to 24.5 W and the slope efficiency was 57%. They demonstrated experimentally that cryogenic cooling of a diamond does not lead to a performance enhancement for short-pulse pumping.

Power scaling with dual output at first and second Stokes wavelengths 1240 and 1485 nm has been demonstrated by McKay, Liu, this author, and Mildren [72] (see

App. A 3). The dual output power reached 14.5 W with slope efficiency of 65%. During both of these experiments, and in the work of Feve et al, no power roll-off was observed as expected given the excellent heat-handling capabilities of diamond.

1.4.3 Continuous wave operation

Prior to the work presented in this thesis, CW operation of DRLs has been reported only in intracavity or coupled-cavity arrangements. The first demonstration of 200 mW output used a Nd:YVO_4 laser and a diamond Raman crystal within a simple oscillator resonant at the fundamental and Stokes wavelengths [57]. Due to the cavity arrangement, thermal effects in the Nd:YVO_4 limited the efficiency.

To demonstrate continuously-tunable Stokes output Parrota et al. [73] utilized a diode-pumped InGaAs semiconductor disk laser, with diamond in a coupled-cavity Raman oscillator. The output power and efficiency were 1.3 W and 14.4% (with respect to absorbed diode-laser pump light), respectively. Due to tunability of the pump laser, the Stokes output wavelength was continuously tuned from 1217 nm to 1244 nm.

Multi-watt CW output has been reported by Savitski et al. [74, 75] and the diamond performance compared to that of a KGW. A coupled-cavity Raman resonator with a diode pumped Nd:YLF pump laser was utilized. The Stokes output reached 5 W at the maximal laser diode pump power of 150 W with 12% diode-to-Stokes slope efficiency. Since no saturation behaviour was observed, the laser was limited by the available pump power.

So far a CW Raman conversion in diamond has been shown only in an intracavity laser configuration with several watts of output power and conversion efficiency below 30%. While the results are promising a true highly efficient high power conversion is yet to be demonstrated. The aim of this thesis is to determine the external-cavity diamond Raman architecture potential for high power beam conversion.

1.5 Thesis outline

To provide necessary background the reader is introduced with the theory for Raman scattering in Chap. 2, with particular reference to diamond. The quantum and classical description presented leads to Raman rate equations and a derivation of the Raman threshold. The pertinent Raman and optical properties of diamond are reviewed.

Chap. 3 presents the first demonstration of efficient conversion in external cavity Raman laser and subsequent power-scaling. The Raman resonator is designed to provide a moderate threshold of about a third of the available pump power. The experiments reveal that diamond outperforms all other Raman crystals in terms of CW output power and efficiency. The main factors limiting conversion and slope efficiency are identified. After these demonstrations, a second higher power quasi-CW pump laser is designed to study Raman lasing at higher powers. No power roll-off was observed suggesting further increases in output are likely using increased pump powers.

An analytical model is derived in Chap. 4 for optimizing performance and predicting behaviour at higher powers. The model is used to optimize design parameters for

efficiency and output power. Strategies to increase of the conversion efficiency near the quantum limit are outlined. Model predictions show that diamond's properties are highly promising for order-of-magnitude power-increase beyond demonstrated 10 W level.

Due to characteristic isolation of the Raman and fundamental pump generation processes intrinsic to the external cavity design, the investigated DRL is an ideal test-platform for studying the polarisation and longitudinal mode properties in detail. In Chap. 5 the influence of a pump polarisation and diamond birefringence on DRL performance is investigated. The impact of these factors is elucidated and design considerations for further experiments, in particular at increased power levels are presented and discussed.

In Chap. 6, spectral broadening in a DRL pumped using a single-frequency is investigated in detail. The results are compared and contrasted with broadening in inversion lasers and the expected broadening properties of Raman scattering. The implications of the results on future single-mode DRL development are discussed.

Chap. 7 summarizes all results and key findings. The implications of discoveries made during the project for various future DRL systems are presented and discussed, along with suggestions for future work.

2

Theory of stimulated Raman scattering in diamond

The Raman effect was independently predicted by several scientists between 1923 and 1927 ([76, 77] among others) but first observed by C. V. Raman and K. S. Krishnan in 1928 [78]. Five years later an early semi-classical theory was developed by G. Placzek [79]. A year after the realisation of the laser by Maiman [80] in 1960, stimulated Raman scattering (SRS) was first observed by Woodbury and Ng [81]. Since then many scientists have contributed to the development of the theoretical description.

This chapter describes the theory of stimulated Raman scattering in the context of diamond. First, a quantum description of Raman interaction is given to show the origin of spontaneous scattering and its transition to the stimulated process. Important quantities such as scattering cross-section are defined at an atomic level. A classical description is also provided as the macroscopic nonlinear interaction of waves forms a more intuitive picture of the stimulated Raman scattering interaction. Maxwell's equations are introduced as a foundation of the light propagation and interaction with matter. Assumptions leading to derivation of a paraxial wave equation are explained and used to describe third order nonlinear processes. Their general form describes the pump and scattered Stokes-wave interaction through a phonon wave excited in the material.

The Raman scattering theory is then applied to diamond as the material of choice in this thesis. Diamond's physical and optical properties are reviewed, and the crystallographic structure of diamond and its significance for Raman lasers is explained.

2.1 Quantum description of Raman scattering

The theoretical background given here is based mainly on the reviews given by Penzkofer [6] and Boyd [82]. Quantum mechanics treats Raman scattering as an interaction between an electromagnetic field and a two-level molecular system. The Raman scattering process, together with absorption and Rayleigh scattering for comparison, is shown in Fig. 2.1. The two level quantum system transits, with a certain probability, from its initial state $|\mathrm{i}\rangle$ to the final state $|\mathrm{f}\rangle$ by absorbing a photon with energy equal to the difference between the two levels. There is also a probability to transit from $|\mathrm{i}\rangle$ to $|\mathrm{f}\rangle$ through a virtual level $|\mathrm{v}\rangle$ by scattering a photon of much higher energy. Raman scattering leads to an energy level transition and thus to a change in energy (frequency) of the incoming photon (inelastic scattering) as opposed to Rayleigh scattering (elastic

scattering).

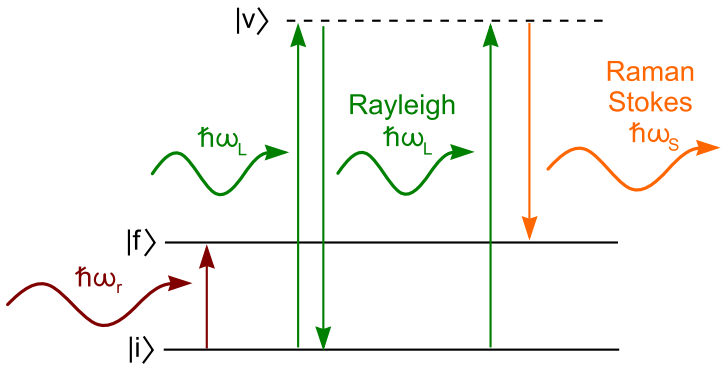

FIGURE 2.1: Interaction of a two level quantum system with photons. The molecule can transit from an initial state $|\mathrm{i}\rangle$ to a final state $|\mathrm{f}\rangle$ either by absorbing a photon with energy equal to the energy difference between the two states ($\hbar\omega_\mathrm{r}$), or by scattering a photon of much higher energy (Raman scattering). For Rayleigh scattering, the final state of the molecule is the same as the initial state.

The total physical system can by assigned a Hamiltonian H which contains the energy contributions of the molecular system H_m electromagnetic field H_em and the interaction between the electric fields and molecular vibrations H_int.

$$H = H_\mathrm{m} + H_\mathrm{em} + H_\mathrm{int}. \tag{2.1}$$

The Hamiltonian of the uncoupled two level molecular system contains kinetic and potential energy summed over all molecules (index i)

$$H_\mathrm{m} = \sum_i \frac{1}{2m}\left(\dot{q}_i^2\right) + \omega_\mathrm{r}^2 q_i^2, \tag{2.2}$$

where q is the local coordinate, m reduced mass and ω_r transition frequency. The Hamiltonian of the electromagnetic field is given as

$$H_\mathrm{em} = \frac{1}{8\pi}\int\left(\epsilon E^2 + \frac{1}{\mu}B^2\right)\mathrm{d}V, \tag{2.3}$$

where, E is the electric field, B is the magnetic field, μ is permeability of the material and V is the integration volume.

The interaction Hamiltonian responsible for Raman scattering is treated by an electric dipole approximation. The Placzek approximation is used to expand the polarisability α as a function of coordinate q

$$\alpha(t) = \alpha_0 + \left(\frac{\partial\alpha}{\partial q}\right)_0 q(t). \tag{2.4}$$

The term linear in q enters the interaction Hamiltonian

$$H_\mathrm{int} = -\frac{1}{2}\sum_i \left(\frac{\partial\alpha}{\partial q}\right)_0 q(r_i)E(r_i)E(r_i), \tag{2.5}$$

where r_i denotes the position of the ith molecule. The Raman coupling between the electromagnetic field with arbitrary frequency and the molecular transition is non-resonant as shown in Fig. 2.1.

After a second quantization of the field variables is applied, the Hamiltonians of the molecular system and the radiation are represented by ensembles of harmonic oscillators

$$\hat{H}_{\mathrm{m}} = \sum_{k_{\mathrm{m}}} \hbar\omega_{\mathrm{r}} \left(b^{+}_{k_{\mathrm{m}}} b_{k_{\mathrm{m}}} + \frac{\hat{I}}{2} \right), \tag{2.6}$$

$$\hat{H}_{\mathrm{em}} = \sum_{k_{\mathrm{em}}} \hbar\omega_{k_{\mathrm{em}}} \left(a^{+}_{k_{\mathrm{em}}} a_{k_{\mathrm{em}}} + \frac{\hat{I}}{2} \right), \tag{2.7}$$

where the subscripts the subscripts m and em stands for material and electromagnetic quantities, respectively, a^{+}, b^{+} are creation and a, b are annihilation operators, the $\hat{H}, \hat{I}$ stand for Hamiltonian and identity operators, ω_{r} is material resonance frequency (i.e., the Raman frequency) and $\omega_{k\mathrm{em}}$ frequency of the electromagnetic radiation with wave vector k and $\hbar$ the Planck's constant divided by 2π.

And the interaction Hamiltonian is given as

$$\begin{aligned} \hat{H}_{\mathrm{int}} = \left(\frac{\partial\alpha}{\partial q} \right)_0 \frac{\pi\sqrt{N_0\hbar^3}}{n_{\mathrm{S}} n_{\mathrm{P}} V\sqrt{m}} \sum_{k_{\mathrm{S}},k_{\mathrm{P}}} \sqrt{\frac{2\omega_{\mathrm{P}}\omega_{\mathrm{S}}}{\omega_{\mathrm{r}}}} \left(\vec{e}_{\mathrm{S}}\vec{e}_{\mathrm{P}}\right) \left(b^{+}_{k_{\mathrm{m}}} a^{+}_{k_{\mathrm{S}}} a_{k_{\mathrm{P}}} \right. \\ \left. + \; b_{k_{\mathrm{m}}} a_{k_{\mathrm{S}}} a^{+}_{k_{\mathrm{P}}} \right) \partial\left(\vec{k}_{\mathrm{P}} - \vec{k}_{\mathrm{S}} - \vec{k}_{\mathrm{m}} \right), \end{aligned} \tag{2.8}$$

where N_0 is the number of molecules, $n_{\mathrm{S,P}}$ are the indices of refraction for the Stokes and pump, respectively, $\vec{e}_{\mathrm{S,P}}$ are the polarisation vectors for the Stokes and pump, respectively, and $\vec{k}_{\mathrm{S,P,m}}$ are the wave vectors for Stokes, pump and material waves, respectively and m is reduced mass.

The quantum system can be described in terms of occupation numbers m_{S}, m_{P}, and m_{m}. Then the interaction Hamiltonian is used to calculate the total rate of Stokes photon generation. The increase in the number of Stokes photons is the difference between the rate of scattered Stokes photons at the expense of pump photons, and the inverse process. Applying Fermi's golden rule and energy conservation, the rate of Stokes photon generation is expressed as

$$\frac{\mathrm{d}m_{\mathrm{S}}}{\mathrm{d}t} = N \left(\frac{\partial\alpha}{\partial q} \right)_0^2 \frac{4\pi^3}{n_{\mathrm{S}}^2 n_{\mathrm{P}} m c_0} I_{\mathrm{P}} \sum_{k_{\mathrm{S}}} \frac{\omega_{\mathrm{S}}}{\omega_{\mathrm{r}}} \left(\vec{e}_{\mathrm{S}}\vec{e}_{\mathrm{P}}\right)^2 \left(1 + m_{\mathrm{S}} + m_{\mathrm{m}}\right) \partial\left(\omega_{\mathrm{S}} - \omega_{\mathrm{P}} + \omega_{\mathrm{r}}\right), \tag{2.9}$$

where $N = N_0/V$ is the number density of molecules, $I_{\mathrm{P}} = \hbar\omega_{\mathrm{P}} c_0/(n_{\mathrm{P}} V) \sum_{k_{\mathrm{P}}} m_{\mathrm{P}}$ is the pump laser intensity and the term $m_{\mathrm{S}} m_{\mathrm{m}}$ has been neglected since $m_{\mathrm{S}}, m_{\mathrm{m}} \ll m_{\mathrm{P}}$.

It can be seen from Eq. (2.9) that three terms contribute to Raman scattering into the Stokes component. The first term grows linearly with pump intensity and represents spontaneous Raman scattering. The second term is proportional to the number of Stokes photons m_{S} already present, and thus causes m_{S} to increase exponentially with the pump intensity. This term represents stimulated Raman scattering. The last

contribution corresponds to parametric coupling between the Stokes field and the material excitation m_m. Since the occupation number of the vibrational state is close to the value of thermal equilibrium it is negligible in many cases [6].

Raman scattering in a two energy level molecular gas explicitly depends on the dot product of the pump laser and Stokes polarisation vectors ($\vec{e}_\mathrm{S}\vec{e}_\mathrm{P}$). In crystals however, the polarisability in Eq. (2.4) is a tensor and the expansion is a function of relative displacement between two sub-lattices of the crystal (only diatomic crystals are assumed). The normalized tensor part of the polarisability determines the relative Stokes scattering efficiency (anti-Stokes Raman tensor can be derived in similar manner [6]), and is called the Raman scattering tensor. This can be obtained by treating the scattering process by third-order time-dependent perturbation theory, which for diamond and zinc-blende structures has been performed by Loudon [83].

In general the polarisability tensor can be simplified by assuming that the Raman frequency ω_r is sufficiently small compared to the pump laser and Stokes frequencies. The shift of a typical crystalline Raman media is about $1000\,\mathrm{cm}^{-1}$ (i.e., frequency of 30 THz) and the wavelength of the electromagnetic fields around 1 µm (i.e., frequency of 300 THz). Therefore, in crystals, this approximation holds for scattering of light with wavelengths much shorter than about 10 µm. The polarisability $\alpha_{zy,x}$ then depends on electronic charge e and mass m of the atoms as

$$\alpha_{zy,x} = -\frac{e^2}{m^2\omega_\mathrm{P}^2\hbar^2 d} R^x_{zy}(-\omega_\mathrm{P}, \omega_\mathrm{P}, 0), \tag{2.10}$$

where d is the lattice constant, and the Raman tensor R^x_{zy} has the same symmetry properties as $\alpha_{zy,x}$.

The Raman tensor describes the probability amplitude for Raman scattering as function of input and output polarisations of a particular crystallographic group. The phonon can participate in Raman scattering if its irreducible representation is equal to one of the reduced representations of the polarisability tensor. The irreducible Raman tensors for most of the crystallographic groups can be found in [84].

When the Raman tensor is known, the Raman scattering efficiency S is given as

$$S = A\left(\sum_{\rho,\sigma=x,y,z} e^\sigma_\mathrm{P} R_{\sigma,\rho} e^\rho_\mathrm{S}\right)^2, \tag{2.11}$$

where A is a proportionality constant, e^σ_P and e^ρ_S are the components of the laser and Stokes unit vectors along the principal axes σ and ρ.

When the pump and Stokes polarisation vectors are aligned with the maximum change in polarisability tensor, the scattering efficiency reaches a maximum and the vector dependance in Eq. (2.9) can be eliminated.

The Stokes power $P_\mathrm{S} = \hbar\omega_\mathrm{S}\,\mathrm{d}m_\mathrm{S}/\,\mathrm{d}t$, spontaneously scattered in a solid angle $\Delta\Omega$ is given as

$$\begin{aligned} P_\mathrm{S} &= VN\left(\frac{\partial\alpha}{\partial q}\right)^2_0 \frac{\omega_\mathrm{S}^4\hbar n_\mathrm{S}}{2c_0^4 m\omega_\mathrm{r} n_\mathrm{P}} I_\mathrm{P}\Delta\Omega \\ &= VN\frac{\partial\sigma}{\partial\Omega} I_\mathrm{P}\Delta\Omega, \end{aligned} \tag{2.12}$$

where c_0 is speed of light in vacuum and integrated scattering cross-section is defined as

$$\frac{\partial\sigma}{\partial\Omega} = \left(\frac{\partial\alpha}{\partial q}\right)_0^2 \frac{\omega_S^4 \hbar n_S}{2c_0^4 m\omega_r n_P}. \tag{2.13}$$

Equation (2.12) clearly shows the linear dependance of spontaneous Stokes power on pump laser intensity.

In the case of stimulated scattering when $m_S \gg 1$, the growth of an individual Stokes mode k_S is given as

$$\frac{\mathrm{d}m(k_S)}{\mathrm{d}t} = N\left(\frac{\partial\alpha}{\partial q}\right)_0^2 \frac{4\pi^3}{n_S^2 n_P m c_0} I_P \sum_{k_S} \frac{\omega_S}{\omega_r} \left(\vec{e}_S\vec{e}_P\right)^2 (1+m(k_S))\,\rho\left(\omega_S - \omega_P + \omega_r\right). \tag{2.14}$$

Equation (2.9) has been generalized by the introduction of the spectral line-shape distribution $\rho(\omega)$. Its width is determined by the molecular damping processes and the finite frequency width of the incident pump laser. For a laser linewidth narrower than the Raman linewidth and a homogeneously broadened molecular transition, a Lorentzian line shape is expected

$$\rho(\omega_S - \omega_P + \omega_r) = \frac{\Gamma_r/2\pi}{\left(\omega_S - \omega_P + \omega_r\right)^2 + \left(\Gamma_r/2\right)^2}. \tag{2.15}$$

The linewidth Γ_r is inversely proportional to the dephasing time T_2 of the physical system and represents full-width-half-maximum (FWHM) of the homogeneous Raman line.

Once $m_S \gg 1$, the solution of Eq. (2.14) predicts exponential growth of the Stokes photons. The peak gain coefficient g_S at the center of the Raman line $\omega_S = \omega_L - \omega_r$ is

$$\begin{aligned} g_S &= N\left(\frac{\partial\alpha}{\partial q}\right)_0^2 \frac{4\pi^2\omega_S}{n_S n_P c_0^2 m\omega_r\Gamma_r} \\ &= N\frac{\partial\sigma}{\partial\Omega}\frac{8\pi c_0^2}{n_S^2\hbar\omega_S^3\Gamma_r}. \end{aligned} \tag{2.16}$$

The Raman gain coefficient thus depends on the integrated scattering cross-section and the Raman linewidth.

The quantum theory explains the origin of Raman scattering as the interaction of a quantized electromagnetic field with a two energy-level quantum system. At first, the Stokes power grows linearly. However, once a sufficient number of Stokes photons are present the exponential solution dominates the Stokes output. The small-signal Raman gain coefficient depends on the Raman linewidth and the scattering cross-section of the material. Once the process becomes stimulated the large number of Stokes photons can be described as a classical electromagnetic field.

2.2 Classical theory of Raman Scattering

In the classical description the propagation and macroscopic interaction of electromagnetic waves in media is described by Maxwell's equations in the form

$$\nabla \times E = -\frac{\partial B}{\partial t}, \tag{2.17}$$

$$\nabla \times H = J + \frac{\partial D}{\partial t}, \tag{2.18}$$

$$\nabla \cdot D = \rho, \tag{2.19}$$

$$\nabla \cdot B = 0, \tag{2.20}$$

which specify the generation of electric and magnetic fields E and H and their interaction with charges ρ and currents J. The interaction is described by constitutive relations

$$D = \epsilon_0 E + P = \epsilon E, \tag{2.21}$$

$$B = \mu_0(H + M) = \mu H, \tag{2.22}$$

$$J = \sigma E. \tag{2.23}$$

The electric displacement D and magnetic induction B are related to their respective field strengths through the permittivity $\epsilon = \epsilon_0\epsilon_\mathrm{r}$ and permeability $\mu = \mu_0\mu_\mathrm{r}$, where subscript 0 denotes free space and subscript r denotes the relative value of a material. The polarisation P of a material depends on the electric field as

$$P = \epsilon_0(\epsilon_\mathrm{r} - 1)E = \epsilon_0\chi_\mathrm{e}E, \tag{2.24}$$

where the electric susceptibility χ_e is a measure of how easily the material becomes polarised (and in analogy for magnetization M). The conductivity σ is the proportionality constant between the electric current density J and the electric field E.

For the following analysis, an interaction with a nonlinear dielectric ($\mu = \mu_0$) media is assumed. The dielectric is isotropic (full rotational symmetry), homogeneous (full translational symmetry), source free (charge density zero) and non-conducting (free current density J is zero). These assumptions are valid for propagation and Raman scattering in gases and some liquids. For anisotropic crystals, ϵ or χ_e are generalized to tensors.

Due to the nonlinear response of the media, the polarisation density vector P is a function of the electric field and can be expressed as a power series

$$P = \epsilon_0 \left[\chi_\mathrm{e}^{(1)}E + \chi_\mathrm{e}^{(2)}E^2 + \chi_\mathrm{e}^{(3)}E^3 + ...\right] \equiv P_\mathrm{L} + P_\mathrm{NL}, \tag{2.25}$$

where $\chi_\mathrm{e}^{(1)}$ describes linear interactions P_L (e.g., refraction). The quantities $\chi^{(2)_\mathrm{e}}, \chi^{(3)_\mathrm{e}}$ are second and third-order nonlinear susceptibilities giving rise to additional frequencies in the light spectrum. The second order optical interactions occur only in non-centrosymmetric media, i.e., crystals without inversion symmetry. Third-order effects on the other hand do not have symmetry restrictions and are present in all substances.

One approach to describe nonlinear interactions is to derive a wave equation with nonlinear polarisation as a driving term. Applying a $\nabla\times$ operator on Eq. (2.17) and using standard vector identities the wave equation acquires the form

$$\nabla^2 E - \frac{n^2}{\mathrm{c}_0^2}\frac{\partial^2 E}{\partial t^2} = \frac{1}{\epsilon_0 \mathrm{c}_0^2}\frac{\partial^2 P_\mathrm{NL}}{\partial t^2}, \tag{2.26}$$

where the index of refraction is defined as $n = \mathrm{c}_0/\mathrm{c} = \sqrt{\epsilon_\mathrm{r}}$.

Stimulated Raman scattering can be described classically by the nonlinear polarisation [82]. The following treatment is restricted to a scalar approximation for clarity.

An optical field applied across a dielectric induces a polarisation in the material proportional to the molecule dipole moment $\vec{p}$ and number of molecules N. The induced dipole moment, described by a damped harmonic oscillator is

$$\vec{p}\,(z,t) = \alpha \vec{E}\,(z,t)\,, \tag{2.27}$$

$$\vec{P} = N\alpha \vec{E}\,(z,t)\,, \tag{2.28}$$

where α is the polarisability of the molecule. The fundamental assumption is that the polarisability is not constant but depends on the internuclear separation $q(t)$ (the Placzek approximation [79])

$$\alpha(t) = \alpha_0 + \left(\frac{\partial \alpha}{\partial q}\right)_0 q(t). \tag{2.29}$$

When the molecule is periodically oscillating due to an applied harmonic field the polarisability will also periodically change. Therefore the refractive index of coherently oscillating molecules will be modulated in time and impress frequency sidebands upon the transmitted electromagnetic wave, separated by the resonant frequency of the oscillator $\pm\omega_\mathrm{r}$.

The molecule is forced to oscillate under the influence of the electric field according to the equation of motion

$$\frac{\mathrm{d}^2 q}{\mathrm{d}t^2} + 2\gamma \frac{\mathrm{d}q}{\mathrm{d}t} + \omega_\mathrm{r}^2 q = \frac{F(t)}{m}, \tag{2.30}$$

where γ is the damping constant, ω_r denotes the resonance frequency of the oscillator, $F(t)$ is the force inducing the vibration and m is the reduced nuclear mass. The force is exerted by the applied optical field in the form of energy W required to establish an oscillating dipole moment

$$W = \frac{1}{2}\alpha \left\langle E^2\,(z,t)\right\rangle, \tag{2.31}$$

$$F(z,t) = \frac{\mathrm{d}W}{\mathrm{d}q} = \frac{1}{2}\left(\frac{\mathrm{d}\alpha}{\mathrm{d}q}\right)_0 \left\langle E^2\,(z,t)\right\rangle, \tag{2.32}$$

where angle brackets represent a time average over an optical period. When it is assumed that the pump laser frequency ω_P and the Stokes frequency $\omega_\mathrm{S} \approx \omega_\mathrm{P} - \omega_\mathrm{r}$ are present in the optical field, the total electric field can be written as

$$E(z,t) = A_\mathrm{P} \exp\left[i\left(k_\mathrm{P} z - \omega_\mathrm{P} t\right)\right] + A_\mathrm{S} \exp\left[i\left(k_\mathrm{S} z - \omega_\mathrm{S} t\right)\right] + c.c., \tag{2.33}$$

and the time varying part of the applied force is

$$F(z,t) = \left(\frac{\partial \alpha}{\partial q}\right)_0 \left\{A_\mathrm{P} A_\mathrm{S}^* \exp\left[i\left(Kz - \Omega t\right)\right] + c.c.\right\}, \tag{2.34}$$

where $K = k_\mathrm{P} - k_\mathrm{S}$ and $\Omega = \omega_\mathrm{P} - \omega_\mathrm{S}$.

After substituting Eq. (2.34) into Eq. (2.30) the amplitude of the molecular vibration is

$$q(\Omega) = \frac{\left(\frac{\partial\alpha}{\partial q}\right)_0 A_\mathrm{P} A_\mathrm{S}^*}{m\left(\omega_\mathrm{r}^2 - \Omega^2 - 2i\Omega\gamma\right)}. \tag{2.35}$$

This solution can be used in (2.28) to find the nonlinear part of the polarisation

$$\vec{P}_\mathrm{NL}(z,t) = N\left(\frac{\partial\alpha}{\partial q}\right)_0 \left[q(\Omega)\mathrm{e}^{i(Kz-\Omega t)} + c.c.\right] \times \left[A_\mathrm{P}\mathrm{e}^{i(k_\mathrm{P}z-\omega_\mathrm{P}t)} + A_\mathrm{S}\mathrm{e}^{i(k_\mathrm{S}z-\omega_\mathrm{S}t)} + c.c\right]. \tag{2.36}$$

Several frequency components are present in the solution. The part oscillating at frequency ω_S is called the Stokes polarisation and its complex amplitude can be expressed as

$$\vec{P}_\mathrm{NL}(\omega_\mathrm{S}) = N\left(\frac{\partial\alpha}{\partial q}\right)_0 q^*(\Omega)A_\mathrm{P}\mathrm{e}^{ik_\mathrm{S}z} = 6\epsilon_0\chi_\mathrm{R}^{(3)}(-\omega_\mathrm{S};\omega_\mathrm{P},-\omega_\mathrm{P},\omega_\mathrm{S})\left|A_\mathrm{P}\right|^2 A_\mathrm{S}\mathrm{e}^{ik_\mathrm{S}z}, \tag{2.37}$$

where the Raman part of the third order susceptibility $\chi_\mathrm{R}^{(3)}$, written so that the real and imaginary part are clearly identified, is defined as [85]

$$\chi_\mathrm{R}^{(3)}(-\omega_\mathrm{S};\omega_\mathrm{P},-\omega_\mathrm{P},\omega_\mathrm{S}) = \frac{N\left(\frac{\partial\alpha}{\partial q}\right)_0^2(\omega_\mathrm{r}^2-\Omega^2) - iN\left(\frac{\partial\alpha}{\partial q}\right)_0^2 2\Omega\gamma}{6\epsilon_0 m\left[\left(\omega_\mathrm{r}^2-\Omega^2\right)^2 + 4\Omega^2\gamma^2\right]}. \tag{2.38}$$

The spatial evolution of the Stokes, anti-Stokes and pump waves can be derived by using the appropriate nonlinear polarisations as a driving term of the wave equation (2.26). The sign of the imaginary part of the susceptibility determines whether the wave will be amplified or attenuated. The development of the wave amplitudes and intensities $I = |E|^2 \mathrm{c}_0 n\epsilon_0/2$ in the slowly varying amplitude approximation is given as

$$\frac{\mathrm{d}A_\mathrm{S}}{\mathrm{d}z} = i\frac{3\omega_\mathrm{S}}{n_\mathrm{S}\mathrm{c}_0}\chi_\mathrm{R}^{(3)}(\omega_\mathrm{S})\left|A_\mathrm{P}^2\right|A_\mathrm{S}, \tag{2.39}$$

$$\frac{\mathrm{d}A_\mathrm{P}}{\mathrm{d}z} = i\frac{3\omega_\mathrm{P}}{n_\mathrm{P}\mathrm{c}_0}\chi_\mathrm{R}^{(3)}(\omega_\mathrm{P})\left|A_\mathrm{S}^2\right|A_\mathrm{P}, \tag{2.40}$$

$$\frac{\mathrm{d}I_\mathrm{S}}{\mathrm{d}z} = -\frac{6\omega_\mathrm{S}}{n_\mathrm{S}n_\mathrm{P}\mathrm{c}_0^2\epsilon_0}\mathrm{Im}\chi_\mathrm{R}^{(3)}(\omega_\mathrm{S})I_\mathrm{P}I_\mathrm{S}, \tag{2.41}$$

$$\frac{\mathrm{d}I_\mathrm{P}}{\mathrm{d}z} = -\frac{6\omega_\mathrm{P}}{n_\mathrm{S}n_\mathrm{P}\mathrm{c}_0^2\epsilon_0}\mathrm{Im}\chi_\mathrm{R}^{(3)}(\omega_\mathrm{P})I_\mathrm{P}I_\mathrm{S}. \tag{2.42}$$

Since $\Omega = \omega_\mathrm{P} - \omega_\mathrm{S}$ is positive, the imaginary part of the Stokes susceptibility (2.38) is negative and therefore the Stokes component is amplified according to Eq. (2.41). Since a scalar approximation is used, the growth depends only on the laser fields intensities. The process is automatically phase-matched and pump phase distortions

are not directly transferred to the Stokes field. Using susceptibility identities it can be shown that the imaginary part of the susceptibility at pump laser frequency is positive and therefore the growth of the Stokes field occurs at the expense of the pump laser field.

A similar argument can be used for the anti-Stokes component. Since $\chi_{\mathrm{R}}^{(3)}(\omega_{\mathrm{a}}) = \chi_{\mathrm{R}}^{(3)}(\omega_{\mathrm{S}})^*$, the photons spontaneously scattered in the anti-Stokes wave will be attenuated. As can be seen from Fig. 2.2, the real and imaginary part of the Stokes and anti-Stokes susceptibilities are mirrored over the pump laser frequency. Efficient generation of anti-Stokes laser radiation is possible only by fulfilling a phase-matching condition of a four-wave mixing component of the third order susceptibility.

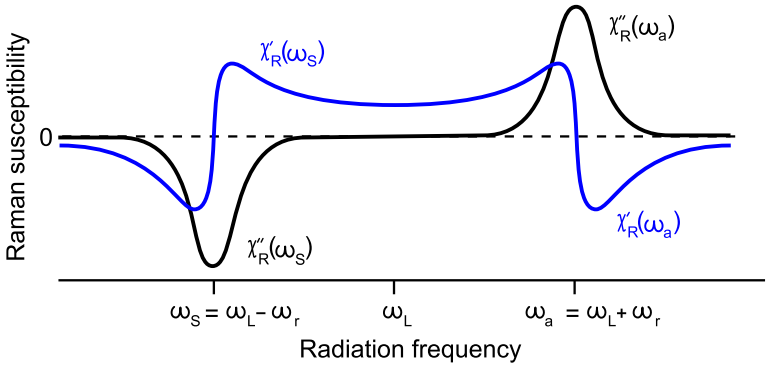

Figure 2.2: Real and imaginary parts of the Stokes ω_{S} and anti-Stokes ω_{a} susceptibilities.

This classical description can explain amplification of the Stokes radiation by the interaction of the pump and Stokes laser fields in a nonlinear medium. The beating between the co-propagating pump (initially strong) and Stokes (initially weak) waves induce molecular vibrations (mutually coherent with the laser fields) at their resonance frequency. The induced oscillating polarisability leads to amplification of the Stokes wave at the expense of the pump. The amplified Stokes wave beats more strongly with the pump, producing stronger molecular oscillations and thus further increasing the conversion of the pump to the Stokes and so on.

2.3 Raman laser equations

For a quantitative description of SRS two sets of differential equations are required; one for the electromagnetic fields and one for the description of the molecular system. The equations can be derived from the wave equation (2.26) and the equation of motion of molecular oscillations (2.30).

It is beneficial to first simplify the general wave equation. Assuming that all interacting waves are harmonic in time and, neglecting the second derivatives, the derived Helmholtz's equation of interacting waves propagating in z direction is given as [86]

$$\frac{n}{c_0}\frac{\partial E}{\partial t} + \frac{\partial E}{\partial z} + \frac{1}{2\epsilon_0 c_0 n}E = \frac{i\omega}{2\epsilon_0 c_0 n}P_{\mathrm{NL}}. \tag{2.43}$$

The equation of the material vibrations (2.30), with the electric field composed of two frequencies ω_{P} and ω_{S} (2.33) as a driving force, is a source of material waves (i.e., phonons). The induced nonlinear polarisation P_{NL} in a material (2.37) is the source of new electromagnetic waves described by the Eq. (2.43). The electromagnetic fields together with the material vibrations can be written as

$$\frac{n_{\mathrm{P}}}{c_0}\frac{\partial A_{\mathrm{P}}}{\partial t}+\frac{\partial A_{\mathrm{P}}}{\partial z}=i\frac{3\omega_{\mathrm{P}}}{n_{\mathrm{P}}c_0}\chi_{\mathrm{R}}^{(3)}(\omega_{\mathrm{P}})qA_{\mathrm{S}}-\frac{1}{2\epsilon_0 c_0 n_{\mathrm{P}}}A_{\mathrm{P}}, \tag{2.44}$$

$$\frac{n_{\mathrm{S}}}{c_0}\frac{\partial A_{\mathrm{S}}}{\partial t}+\frac{\partial A_{\mathrm{S}}}{\partial z}=i\frac{3\omega_{\mathrm{S}}}{n_{\mathrm{S}}c_0}\chi_{\mathrm{R}}^{(3)}(\omega_{\mathrm{S}})qA_{\mathrm{P}}-\frac{1}{2\epsilon_0 c_0 n_{\mathrm{S}}}A_{\mathrm{S}}, \tag{2.45}$$

$$\frac{\partial q}{\partial t}+\Gamma q=\frac{i}{2m\omega_{\mathrm{r}}}\left(\frac{\partial\alpha}{\partial q}\right)_0 A_{\mathrm{P}}A_{\mathrm{S}}^{*}, \tag{2.46}$$

where the pump and Stokes are resonant with the Raman transition $\omega_{\mathrm{P}}-\omega_{\mathrm{S}}=\omega_{\mathrm{r}}$. In most cases the molecular vibrations are heavily damped.

When the excitation pulse has much longer duration than the dephasing time of the optical phonons (typically picoseconds for most crystals) the transient behaviour of the SRS can be neglected. Therefore the solution to the equation of molecular vibrations can be substituted into Eq. (2.44) and (2.45). Introducing intensity in the same way as in Eqs. (2.39–2.42) ($I=|E|^2\,\mathrm{c}_0 n\epsilon_0/2$), the rate equations for pump and Stokes intensities are obtained as

$$\frac{n_{\mathrm{P}}}{c_0}\frac{\partial I_{\mathrm{P}}}{\partial t}+\frac{\partial I_{\mathrm{P}}}{\partial z}=-g_{\mathrm{P}}I_{\mathrm{P}}I_{\mathrm{S}}-\alpha_{\mathrm{P}}I_{\mathrm{P}}, \tag{2.47}$$

$$\frac{n_{\mathrm{S}}}{c_0}\frac{\partial I_{\mathrm{S}}}{\partial t}+\frac{\partial I_{\mathrm{S}}}{\partial z}=g_{\mathrm{S}}I_{\mathrm{P}}I_{\mathrm{S}}-\alpha_{\mathrm{S}}I_{\mathrm{S}}, \tag{2.48}$$

where $\alpha_{\mathrm{S,P}}$ are absorption loss coefficients for the Stokes and pump fields, respectively and the small-signal Raman gain $g_{\mathrm{S}}=g_{\mathrm{P}}\omega_{\mathrm{S}}/\omega_{\mathrm{P}}$ is defined by Eq. (2.16) and the susceptibility is given by Eq. (2.38). Equations for additional Stokes components can be added in a similar manner.

If the pump and Stokes fields are time-independent (CW lasers), the time derivatives can be set to zero and the equations further simplify to

$$\frac{\partial I_{\mathrm{P}}}{\partial z}=-g_{\mathrm{P}}I_{\mathrm{P}}I_{\mathrm{S}}-\alpha_{\mathrm{P}}I_{\mathrm{P}}, \tag{2.49}$$

$$\frac{\partial I_{\mathrm{S}}}{\partial z}=g_{\mathrm{S}}I_{\mathrm{P}}I_{\mathrm{S}}-\alpha_{\mathrm{S}}I_{\mathrm{S}}. \tag{2.50}$$

Neglecting the depletion of the pump wave, the integration of Eq. (2.50) from 0 to the length of the interaction L gives an exponential solution

$$I_{\mathrm{S}}(L)=I_{\mathrm{S}}(0)\exp\left(g_{\mathrm{S}}I_{\mathrm{P}}L-\alpha_{\mathrm{S}}L\right). \tag{2.51}$$

The Stokes beam is exponentially amplified as it propagates down the Raman medium.

At threshold the premise of an un-depleted pump field is fulfilled. Therefore, the threshold condition can be derived by equating the round-trip gain and the loss within

the resonator.

$$I_{\mathrm{P}}^{\mathrm{th}} = \frac{2\alpha_{\mathrm{S}}L - \ln(R)}{2g_{\mathrm{S}}L}, \tag{2.52}$$

where R is the the total reflectivity of resonator mirrors.

To correctly predict the Stokes output power as a function of the incident pump, the depletion of the pump beam must be taken into account. The coupled Eq. (2.49), (2.50) are generally solved numerically, or under certain conditions can be treated analytically (as in Chap. 4).

2.4 Diamond as a Raman medium

The Raman crystal chosen for the external cavity Raman laser in this thesis is a synthetic single-crystal (SC) diamond. In this section the basic principles of SC diamond growth and its properties are presented and the general Raman scattering theory is applied to diamond.

2.4.1 Optical-quality diamond growth

The use of diamond as a Raman gain medium places stringent requirements on the crystal quality. Stress-induced birefringence and residual absorption due to impurities elevate the laser threshold and compromise its performance (see Chaps. 3 and 5). Therefore, only samples made by chemical-vapor-deposition (CVD) where the growth conditions can be tightly monitored and controlled have been used to demonstrate efficient DRL operation.

CVD synthesis of high quality diamond has been described and reviewed by Friel et al. [41, 50]. The method utilizes a hydrocarbon source gas introduced into a chamber under low pressure (tens to hundreds of Torr). The substrate is heated to around 700 to 1200 °C. In order to provide the reactive components the gas mixture has to be activated. Several methods can be used including hot filament, microwave plasma, arc-jet and others [41].

The microwave plasma deposition (MPCVD) activation technique currently provides the highest-quality diamond for optical applications. In a growth chamber, the microwave plasma provides energy to drive the chemical reactions. Single or polycrystalline diamond can be grown depending on the substrate [50].

Single-crystal diamond must be grown on single-crystal diamond substrates, usually on a 100-oriented surface [50]. Dopants can be introduced during the process in a controlled manner; however, even without deliberate doping, some level of impurities and defects is unavoidable [50]. The level of defect formation is linear with crystal growth-rate, but inversely proportional to the square of the atomic hydrogen flux. Therefore there is a trade off in growth-rate when synthesizing high quality material.

2.4.2 Diamond lattice structure

Diamond's lattice is composed of highly-symmetrical covalently-bonded carbon atoms. To understand the crystallographic geometry, the terminology and structure are explained in this section.

Diamond's atomic structure belongs to the O^7_h-Fd$\bar{3}$m space group and consists of two interpenetrating face centered cubic (FCC) Bravais lattices (red and blue in Fig. 2.3) displaced along the body diagonal of the cubic cell by one quarter the length of the diagonal. However, the full diamond lattice is not Bravais, since the environment of each point differs in orientation from the environment of its nearest neighbours [84, 87].

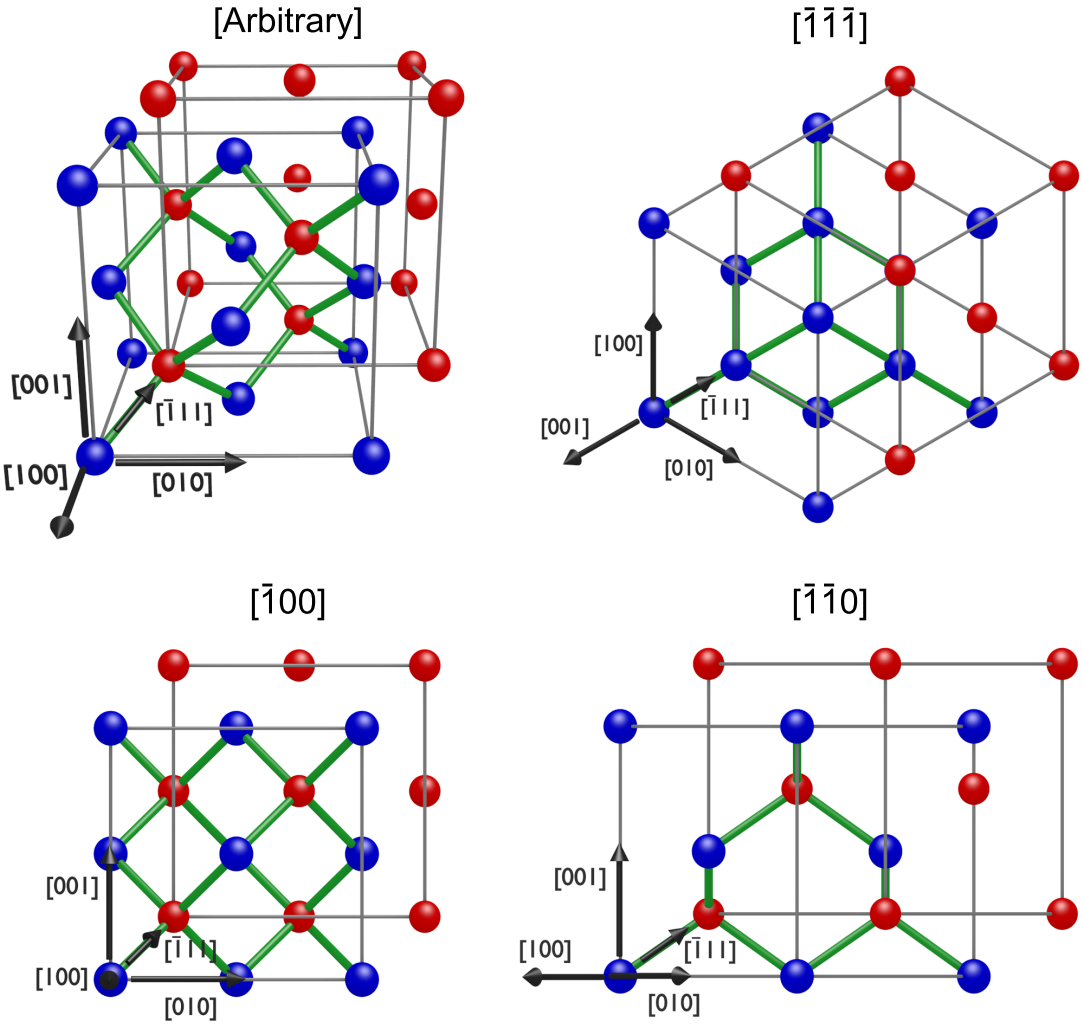

FIGURE 2.3: Two interpenetrating FCC lattices (in red and blue) form diamond's crystallographic structure. Top left – seen in perspective for an arbitrary angle, top right – orthographic view along [$\bar{1}\bar{1}\bar{1}$] direction, bottom left– orthographic view along [$\bar{1}$00] and bottom right – orthographic view along [$\bar{1}\bar{1}$0] direction.

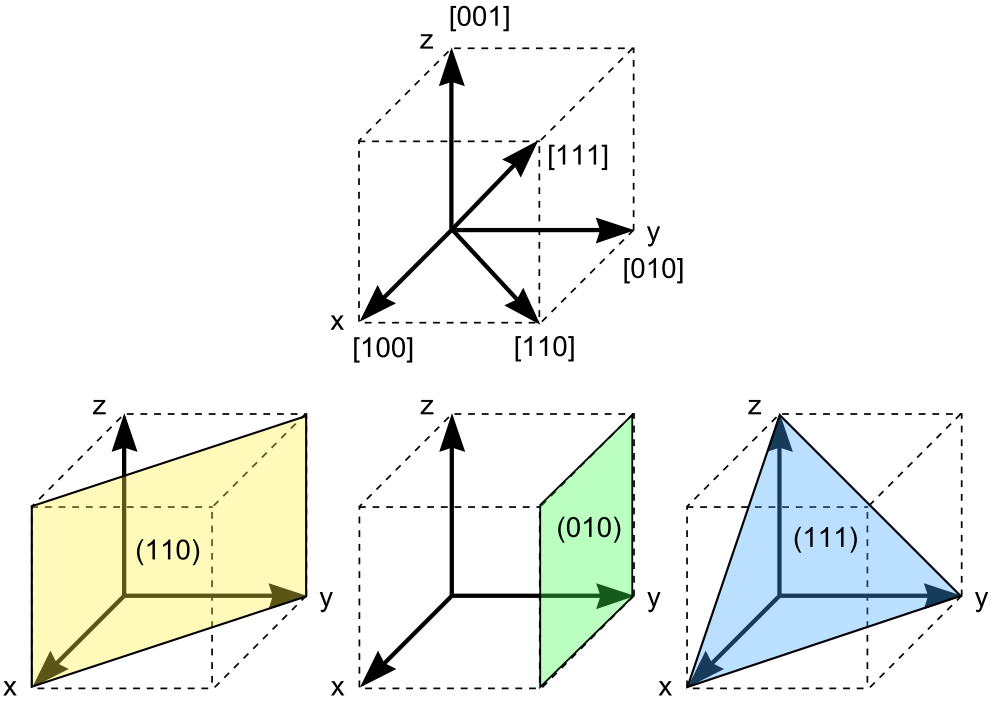

Figure 2.4: Crystallographic directions and orientation of planes defined by Miller indices.

The crystallographic planes and directions are labeled using Miller indices [88]. After associating unit vectors with a right handed x,y,z Cartesian coordinate system in a crystal, designation of the specific planes (hkl) is enclosed in parentheses, and directions perpendicular to the planes in brackets $[hkl]$, as shown in Fig. 2.4. It is often useful to refer to all equivalent planes or directions. The family of such planes and directions is written in braces $\{hkl\}$ and chevrons $\langle hkl \rangle$, respectively. The bar above a number denotes opposite direction.

Distinguished directions with respect to the crystallographic structure are shown in Fig. 2.3. In the following chapters the vertical direction is defined as the [001] direction, and the horizontal as the $[\bar{1}10]$ direction. The beams, in all cases in this thesis, propagate through the crystal parallel to the $[\bar{1}\bar{1}0]$ direction (or generalized to $\langle 100 \rangle$ and $\langle 110 \rangle$ respectively). The beam polarisation direction is usually aligned with either the $[\bar{1}11]$ or $[1\bar{1}1]$ direction, but is refereed to simply as $\langle 111 \rangle$.

During CVD deposition, the diamond grows in the $\langle 100 \rangle$ direction and with $\{111\}$ faces on its sides [41]. For use in Raman lasers, the samples' sides are cut to form $\{110\}$ planes (see Fig. 2.5), as propagation of the pump along the $\langle 110 \rangle$ direction and having the orientation of its polarisation parallel to the $\langle 111 \rangle$ axis maximizes the Raman gain (see later Sec. 2.4.4).

2.4.3 Diamond properties

Natural and synthetic diamonds can be classified according to their level of impurities into two categories. Type I samples contain more than 5 ppm of mainly nitrogen in

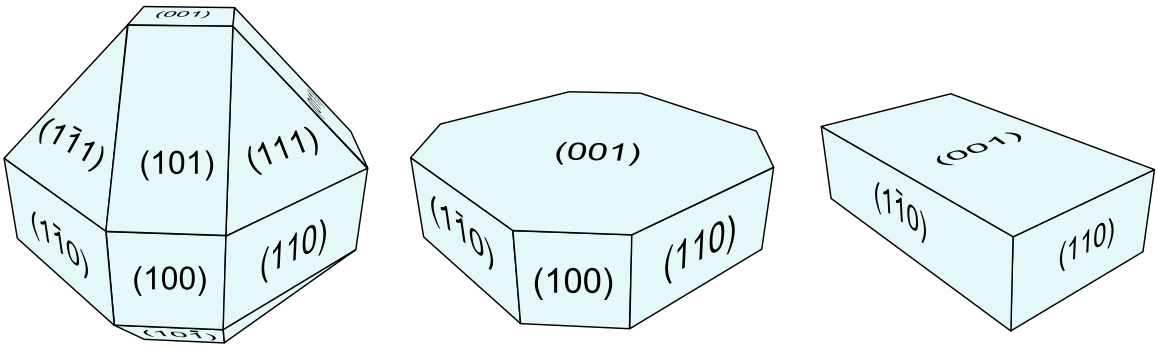

FIGURE 2.5: Illustration of a diamond sample (right), cut from the general diamond shape. The sample sides are formed by {110}, and top and bottom by {100} planes.

either aggregated form (Ia) or as a single substitution (Ib). More than 98% of all natural diamonds are type I. Specimens with less than 5 ppm of impurities are called type II. In type IIa, nitrogen is the main impurity and the diamond is electrically insulating. If the major impurity is boron, the diamond is a p-type semiconductor and of type IIb. In this work, SC CVD diamonds with nitrogen content between 0.02 and 0.1 ppm and reduced stress-induced birefringence are used. This very unique material is sometimes labeled as type IIIa by the manufacturer, Element Six [51].

Type IIa CVD-grown samples exhibit all the extreme properties for which diamond is known. Of many outstanding properties (extreme hardness, dielectric strength, and high speed of sound) there are several that are of particular interest for developing lasers. Thermal conductivity, which is crucial for high power operation, is highest in diamond amongst any bulk material at room temperature and is more than several hundred times higher in diamond than glasses and most crystalline materials. For SC CVD diamond, the thermal conductivity is about $2000\,\mathrm{Wm^{-1}K^{-1}}$ [50, 51] and second only to graphite in the form of mono-layer – graphene. That makes it ideal for thermal management and high power applications such as heat sinks and kilowatt-class CO_2 laser windows. However, bonding of diamond with other materials is not trivial due to its very low thermal expansion of $1.1 \times 10^{-6}\,\mathrm{K^{-1}}$. The thermo-optic coefficient dn/dT is positive and moderate compared to other crystals. As a result, heat deposited in the crystal due to optical pumping or inelastic (i.e., Raman) scattering generates (positive) thermal lenses of strength several orders of magnitude weaker than in other materials under an identical thermal load (see Sec. 3.5.1 for details).

The diamond transparency range is also exceptional, spreading from the deep UV to far the IR. The absorption spectrum shown in Fig. 2.6 highlights the absorption edge at 225 nm, associated with diamonds indirect band gap, and 2 and 3-phonon excitation peaks between 2.5 and 6.5 µm.

Diamond, like all crystals, is subject to optical imperfections and extrinsic losses due to impurities and structural defects. The dominant cause of absorption loss in high-quality SC diamond, however, is nitrogen. In the gas phase, during CVD diamond synthesis, nitrogen increases the speed of growth; however, it also influences the optical properties. Nitrogen atoms incorporated in the diamond lattice form several neutral

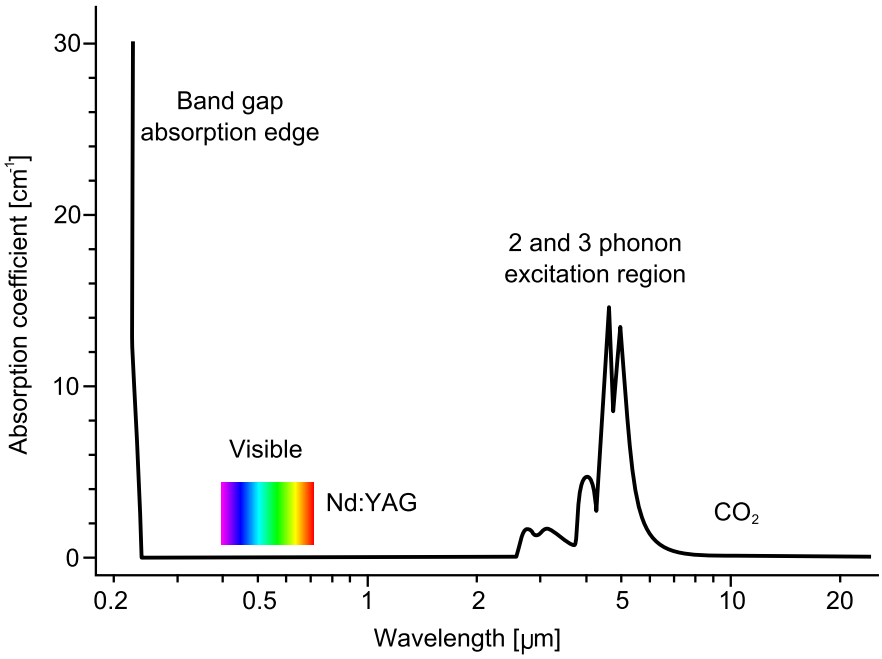

Figure 2.6: Room temperature intrinsic absorption of diamond, taken from [50]

or charged defects with absorption mainly in the UV and visible spectral regions. However, even in the IR around 1064 nm some absorption prevails. The mechanism is not yet fully understood, but seems to correlate with the nitrogen concentration in the gas mixture [41]. Samples with nitrogen concentration of 20 ppb have absorption coefficients of approximately $10^{-3}\,\mathrm{cm}^{-1}$ (see Fig. 2.7 taken from [50]). The isotopic purity of the CVD diamond is almost 99% when grown using un-enriched feed stock.

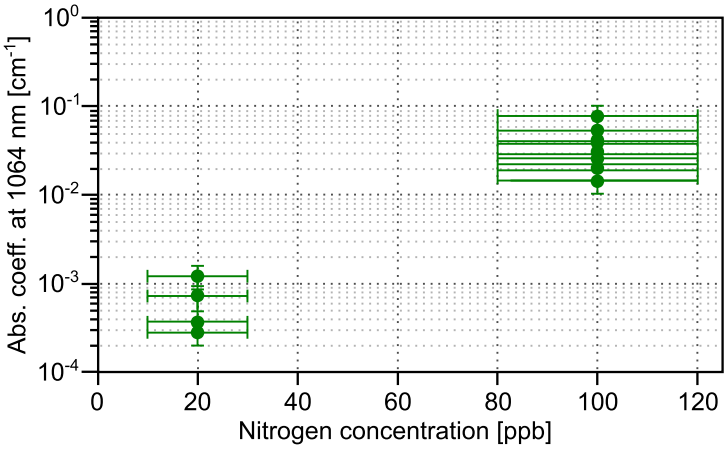

Figure 2.7: SC diamond residual absorption of samples containing approximately 20 and 100 ppb of nitrogen, taken from [50].

Another material parameter that is of importance for Raman lasers is birefringence. Diamond should be an isotropic material because of its symmetrical cubic lattice.

However, the strain from in-grown defects and the stress accumulated in the lattice during the growth process leads to birefringence. The dislocations in (100)-grown SC CVD diamond tend to propagate forming a line in the same direction or at 45°. The birefringence of these samples, measured by polarisation microscopy (Metripol [89, 90]), shows chaotic patterns with clusters of defects as well as regions of very low birefringence values. An example of birefringence in optical-grade SC CVD diamond shown in Fig. 2.8, reveals that the difference between the refractive index in the fast and slow axes can range from 10^{-8} to up to 10^{-4}.

Influence of absorption loss and residual birefringence on DRL performance has been studied theoretically and experimental in detail, and is elucidated in Chaps. 3 and 5.

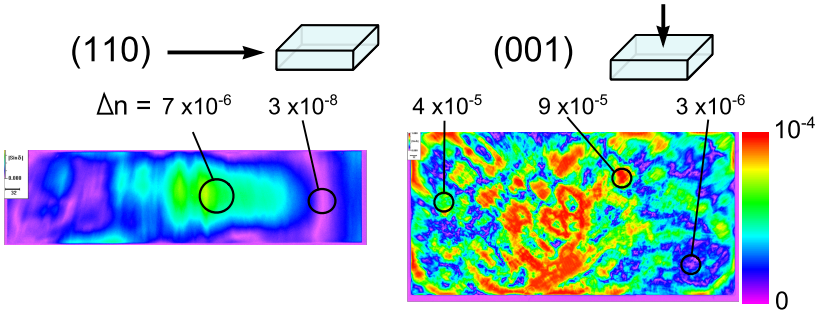

FIGURE 2.8: Stress-induced birefringence in the diamond along the [110] direction (left) and the [001] (right) [51].

2.4.4 Raman scattering in diamond

In this section the general theory of Raman scattering is applied to diamond. Measured Raman properties are listed and the polarisation behaviour explained.

In diamond, the optical phonon is associated with a vibrational mode involving the relative displacement of the two interpenetrating FCC lattices in the ⟨111⟩ direction as illustrated in Fig. 2.9. When the pump laser propagates along the ⟨110⟩ direction, which is perpendicular to the ⟨111⟩ direction, the beam polarisation can be aligned with ⟨100⟩, ⟨111⟩ or ⟨110⟩, or any angle in between.

Diamond, as a material with $Fd\bar{3}m$ symmetry and consisting of two interpenetrating face-centred cubic lattices, has a triply degenerate Raman tensor which can be written in the ⟨100⟩ orientation as [84]

$$\underset{R_1}{\begin{pmatrix} 0 & 0 & 0 \\ 0 & 0 & d \\ 0 & d & 0 \end{pmatrix}} \quad \underset{R_2}{\begin{pmatrix} 0 & 0 & d \\ 0 & 0 & 0 \\ d & 0 & 0 \end{pmatrix}} \quad \underset{R_3}{\begin{pmatrix} 0 & d & 0 \\ d & 0 & 0 \\ 0 & 0 & 0 \end{pmatrix}}, \tag{2.53}$$

where d is the spatial derivative of the crystal polarisability along the direction of carbon-carbon bonds.

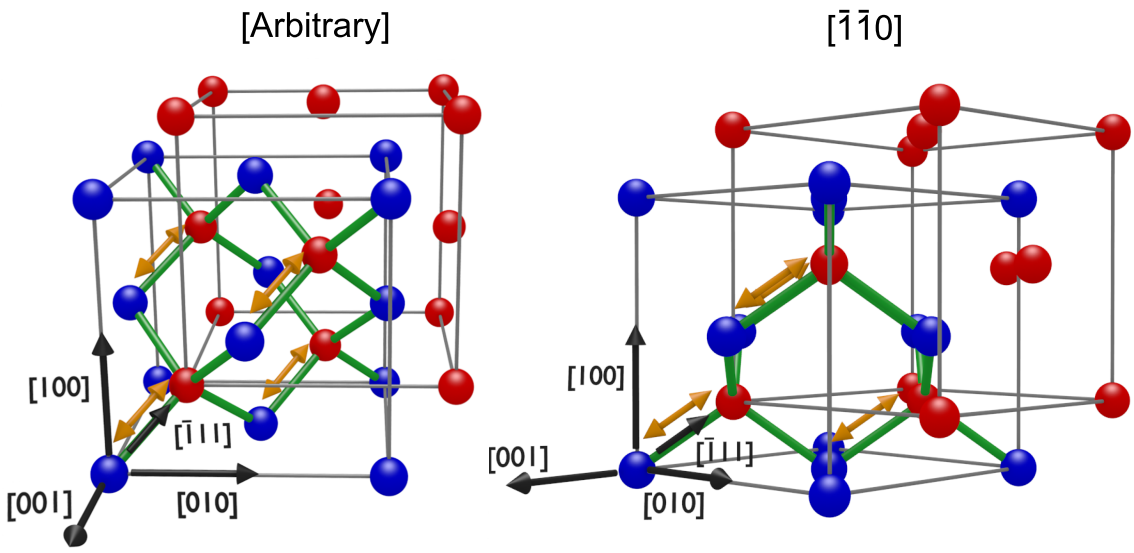

Figure 2.9: Crystallographic structure of diamond, showing the direction of the Raman vibrational mode (orange arrow) along the [$\bar{1}$11] axis.

When rotated counterclockwise around [100] by 45° (see Fig. 2.9) the tensor, now in the ⟨110⟩ orientation (corresponding to the propagation direction), takes the form

$$\underset{R_1}{\begin{pmatrix} 0 & 0 & \frac{d}{\sqrt{2}} \\ 0 & 0 & \frac{d}{\sqrt{2}} \\ \frac{d}{\sqrt{2}} & \frac{d}{\sqrt{2}} & 0 \end{pmatrix}} \quad \underset{R_2}{\begin{pmatrix} 0 & 0 & \frac{d}{\sqrt{2}} \\ 0 & 0 & -\frac{d}{\sqrt{2}} \\ \frac{d}{\sqrt{2}} & -\frac{d}{\sqrt{2}} & 0 \end{pmatrix}} \quad \underset{R_3}{\begin{pmatrix} d & 0 & 0 \\ 0 & -d & 0 \\ 0 & 0 & 0 \end{pmatrix}}. \tag{2.54}$$

The calculation of spontaneous scattering efficiency, according to Eq. (2.11), shows that the maximum is reached when the pump and Stokes polarisations are aligned with the ⟨111⟩ direction, which is the direction of the Raman mode vibrations [63]. In that case, the beating between the pump and Stokes wave causes the strongest change in polarisability of the diamond. A detailed calculation and comparison with measurements is provided in Chap. 5.

The Raman frequency determining the wavelength shift is 1332.3 cm^{-1}. The small-signal Raman gain coefficient of diamond has been measured by several groups at different wavelengths [91–93]. Figure 2.10 shows the various measurements summarized in [41]. The Raman gain coefficient for 1064 nm pumping is approximately 10 cm/GW.

The naturally broadened Raman linewidth arises from anharmonic forces on the phonon oscillator and the resulting damping. The full-width at half-maximum (FWHM) Raman linewidth has been measured spectroscopically by several groups to be between 1 and 4 cm^{-1} at room temperature [41]. Alternatively measurement of the phonon dephasing time, which is inversely proportional to the homogeneous linewidth, yields the value of 1.56 cm^{-1} [94]. The influence of Raman linewidth on Raman gain and DRL performance is treated in detail in Chap. 6.

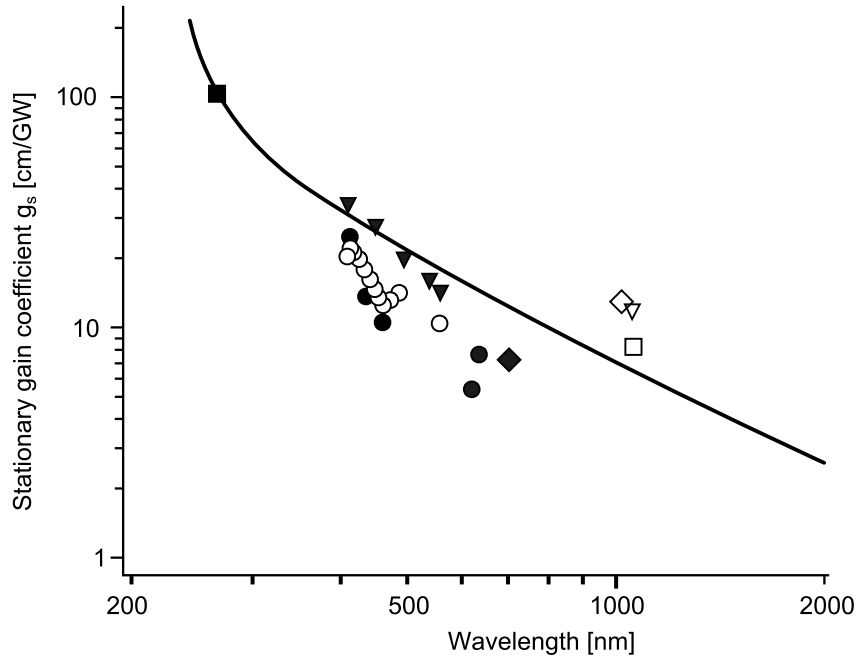

FIGURE 2.10: Raman gain coefficient of diamond as a function of pump wavelength, taken from [41].

2.5 Summary

This chapter has summarized the important background from the quantum and classical treatment of the Raman scattering. Using the classical treatment, and the gain coefficient provided by the quantum mechanical treatment, macroscopic stimulated Raman scattering is described by rate equations for depletion of the pump field and exponential growth of the Stokes wave. These equations form a foundation for derivation of an analytical model, describing amplification of the Stokes radiation as a function of pump power in the Chap. 4

Diamond's optical and thermal properties were briefly described. In order for diamond to be a practical Raman gain material in a laser, (particularly in a CW laser discussed in this thesis), it is critical optical losses are minimal. Absorption loss, due to the incorporation of nitrogen in the diamond during the growth process, has been highlighted as a dominant loss mechanism in the CVD diamond. The impact of loss on efficiency of the DRL is studied and discussed in Chap. 3.

Birefringence due to residual stress from the growth process has also been identified as important for efficient Raman laser operation. A theoretical and experimental study of DRL performance as a function of birefringence is discussed in detail in Chap. 5.

3

Continuous wave external cavity diamond Raman laser

This chapter presents the experimental development of a CW external cavity diamond Raman laser. First, the Raman resonator parameters are estimated to provide moderate generation threshold using theory from Chap. 2. Tolerances on pump beam parameters and output coupling transmission confirm that common optical components and laser pump sources can be used.

Aside from the Raman cavity, a substantial part of this chapter's investigation consisted of the development of suitable pump sources. A modular approach has been chosen for its simplicity and seemingly simple scalability. A pump laser with an output power (30 W) about three times the calculated Raman threshold was designed in order to demonstrate efficient and high-power CW external cavity Raman conversion. The second part of the chapter details the design and performance of a second pump laser that operated at reduced duty-cycle to provide pump powers up to 50 W and of sufficiently long duration to enable investigation of the external cavity Raman laser under conditions representative of steady-state operation.

The DRL was characterized and its performance analysed using energy conservation and heat management calculations. The external cavity Raman laser provides convenient access to all laser fields contributing to the interaction (pump, Stokes and residual pump). This enabled a power budget of the Raman conversion to be evaluated and used to determine factors limiting conversion efficiency. Calculation of thermal lensing is used to estimate the power-scaling limits of the configuration and to determine strategies for further power scaling.

3.1 Estimation of Raman lasing threshold

To verify the possibility of CW external cavity Raman conversion in diamond, the design parameters to achieve a moderate threshold $P_{\mathrm{P}}^{\mathrm{thr}}$ of 10 W incident pump power are calculated. The laser threshold is defined as the point where the round-trip gain equals the resonator loss. Losses include the useful output due to output coupler (OC) transmission, and parasitic losses such as surface reflections, bulk scatter, absorption, and diffraction loss. Gain depends on the Raman gain coefficient (approximately 10 cm/GW in diamond at 1064 nm [41, 70, 92]), pump intensity (i.e., pump peak power and focusing), and the length of the interaction.

The absorption coefficient α of the diamond samples at 1064 nm is below $2 \cdot 10^{-3}\,\mathrm{cm}^{-1}$

for ultra low nitrogen concentration samples (typically tens of ppb) [50, 64, 75]. Measurements of the residual absorption of diamond samples used in experiments at are not available in literature at the Stokes wavelength. However, as nitrogen and its inclusions in the diamond lattice do not have any absorption peaks in the infrared [41], it is reasonable to use the absorption coefficient at 1064 nm as an approximation. A value of $3.5 \cdot 10^{-3}\,\mathrm{cm}^{-1}$ is used to accommodate other minor loss mechanisms such as crystal coating reflections and bulk scatter.

The Raman laser threshold condition for a double pass pumped linear cavity is (see Chap. 2)

$$P_{\mathrm{thr}}^{\mathrm{P}} = \frac{z_{\mathrm{P}} M^2 \lambda_{\mathrm{P}}}{n_{\mathrm{P}}} \frac{T + 2\alpha L}{4 g_{\mathrm{S}} L}, \tag{3.1}$$

where the pump Rayleigh range z_{P} is given as

$$z_{\mathrm{P}} = \frac{w_{\mathrm{P}}^2 \pi n_{\mathrm{P}}}{M^2 \lambda_{\mathrm{P}}}. \tag{3.2}$$

With all parameters defined the Raman generation threshold at 1064 nm is a function of pump M^2 and output coupling transmission T. A typical pump laser may have the M^2 in the region of 1 to 1.6. That equates to pump waist radii of 36–45 µm, when considering the size of optical components and the length of the Raman resonator. Lasing threshold as a function of the output coupler transmission is shown in Fig. 3.1 for a crystal length L =1 cm, a pump wavelength λ_{P} = 1064 nm and M^2 parameters of 1, 1.3, and 1.6. As can be seen a threshold of about 10 W can be reached with an output coupling of approximately 0.5%.

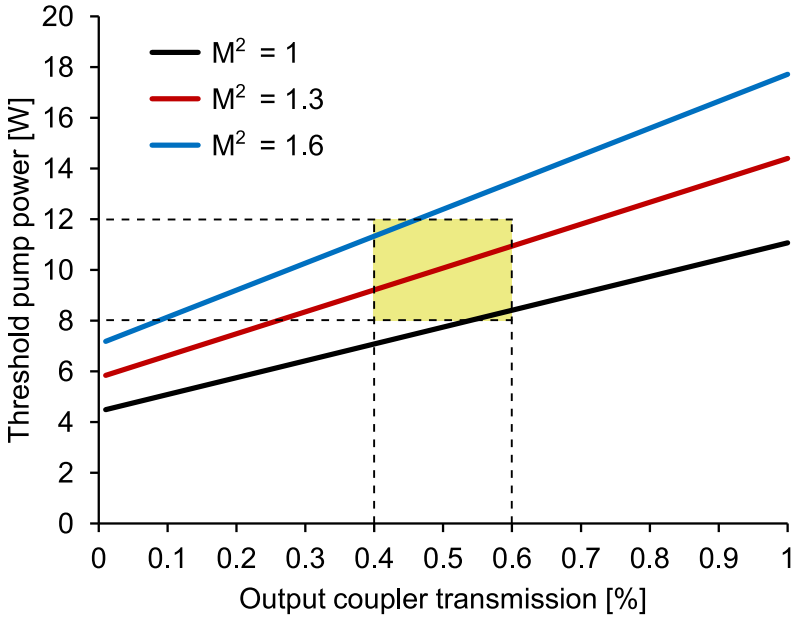

FIGURE 3.1: Threshold pump power as a function of OC transmission for three different beam quality parameters. A threshold of approximately 10 W is obtained for transmission of 0.5% with M^2 tolerance of 1–1.6.

3.2 30 W Nd:YVO continuous-wave pump laser

The predicted threshold of about 10 W for a 1 µm pump source allows the use of a large variety of laser systems. As Raman gain decreases markedly with pump spectral linewidth for $\Gamma_P > \Gamma_r$, a Nd laser ($\Delta\nu_P \approx$ GHz) is sufficiently narrow not to significantly compromise the minimum laser threshold achievable. The pump radiation should be linearly polarised, as explained in Sec. 2.4.4. Therefore a birefringent laser crystal such as Nd:YVO_4, ensuring polarised output without the need of intracavity polarising elements, is well suited to the application.

The Nd:YVO_4 gain crystal is often pumped by 808 nm diodes [1] in an end or side-pumped geometry [2]. In this work a side-pumped CW high-power vanadate module (RBA Nd:YVO_4, Northrop Grumman CEO) was chosen to allow larger flexibility in the resonator design and higher output powers [40].

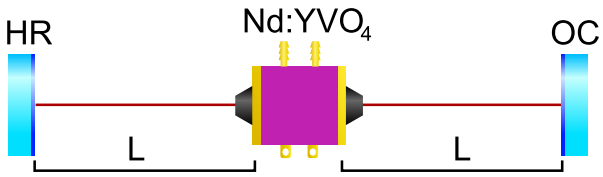

Figure 3.2: Schematic of the Nd:YVO_4 pump laser. The distance L can be adjusted for multi-mode or single-mode operation.

The need for low M^2 operation requires a high volume resonator, where the fundamental TEM_{00} mode fills the smallest aperture in the cavity [2]. In a symmetrical flat-flat cavity (see Fig. 3.2), the thermal lens in the gain medium stabilizes the resonator and the laser crystal diameter provides the smallest aperture in the cavity filtering out higher order modes. The resonator becomes unstable in this design if the thermal lens focal length is shorter than $\frac{1}{4}$ of the resonator length.

Taking the thermal lens of 180 mm at the maximum pump diode current of 23 A into account (using the manufacturer's specification data), the TEM_{00} cavity mode expands across the 2 mm wide vanadate laser rod for a mirror spacing of 790 mm, as shown in Fig. 3.3 (simulated using the Gaussian beam propagation protocol WinLase). The fundamental mode radius, shown in Fig. 3.4 as a function of thermal lens focal length, expands as the pump power and lens strength increases. The mode attains the rod radius for a 190 mm-long lens and diverges, thus destabilizing the cavity, for a 180 mm-long lens at the maximum available pump power.

Multi-mode operation of the laser using a 150 mm long resonator is compared to fundamental mode output in Fig. 3.5. At threshold the optimized laser generates in fundamental resonator mode (inset of Fig. 3.5); however, higher order modes appear as the pump power increases. Close to the maximal pump current the mode structure starts to collapse back to a fundamental Gaussian shape. The best M^2 achievable with

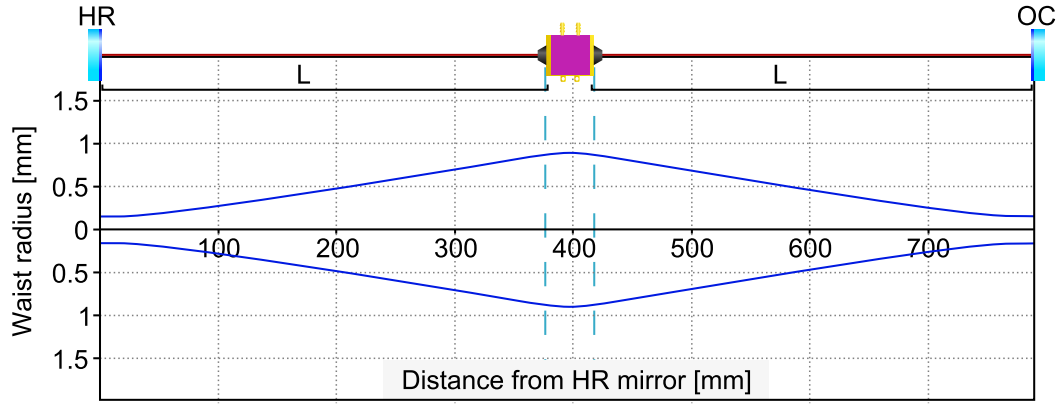

FIGURE 3.3: Intracavity laser field profile for a thermal lens of focal length 200 mm.

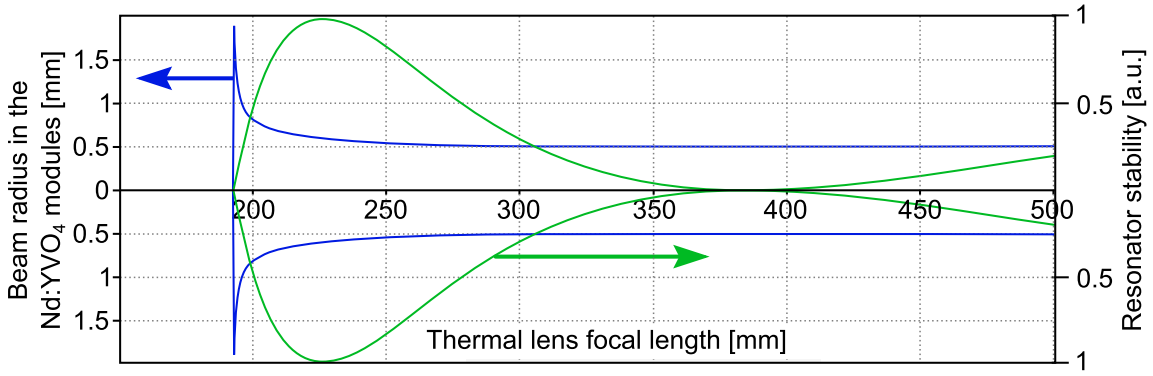

FIGURE 3.4: Resonator stability and waist radius in the laser rod as a function of thermal lens focal length for a mirror-to-module distance L = 375 mm.

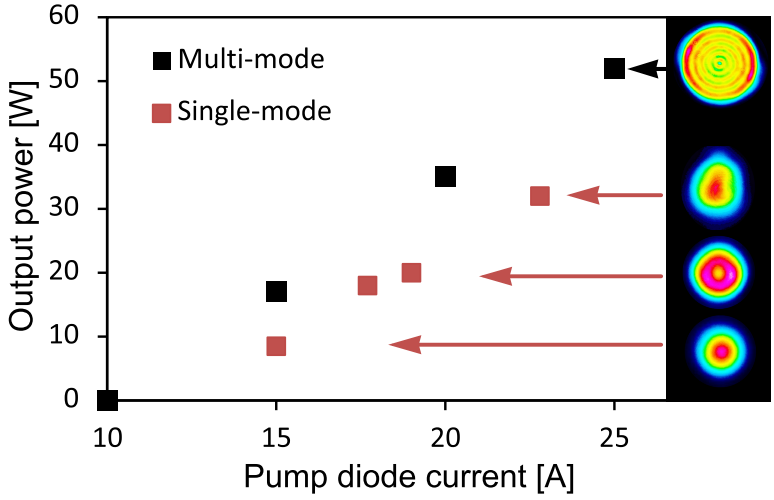

FIGURE 3.5: Laser output power in multi- and near single-mode regime.

output power higher than 30 W was 1.6, as measured using a beam profiler (BeamGage DataRay Inc.).

The vanadate laser linewidth of 53 GHz was measured using an optical spectrum analyzer (Anritsu MS9710B).

3.3 Raman cavity design considerations

In order to mode-match the Stokes intracavity field waist to the tightly-focused pump beam, the cavity must be close to concentric. That allows for a relatively simple and short resonator design with manageable mirror curvatures. The lens that focuses the pump beam into the diamond is chosen to produce a waist radius, and thus a Rayleigh range, predicted by the threshold calculation.

The Raman resonator was designed using the Gaussian beam propagation tool. A lens with a focal length of 50 mm focuses the pump through the concave input coupler (IC) with radius of curvature of 50 mm into a 9.5 mm-long diamond. Due to the IC curvature, the pump beam is slightly defocused and the waist is shifted towards the output coupler (OC). A collimated pump with a 1.2 mm radius (at $\frac{1}{e^2}$) incident upon the lens (f) forms a 33 µm waist radius in the diamond as depicted in Fig. 3.6.

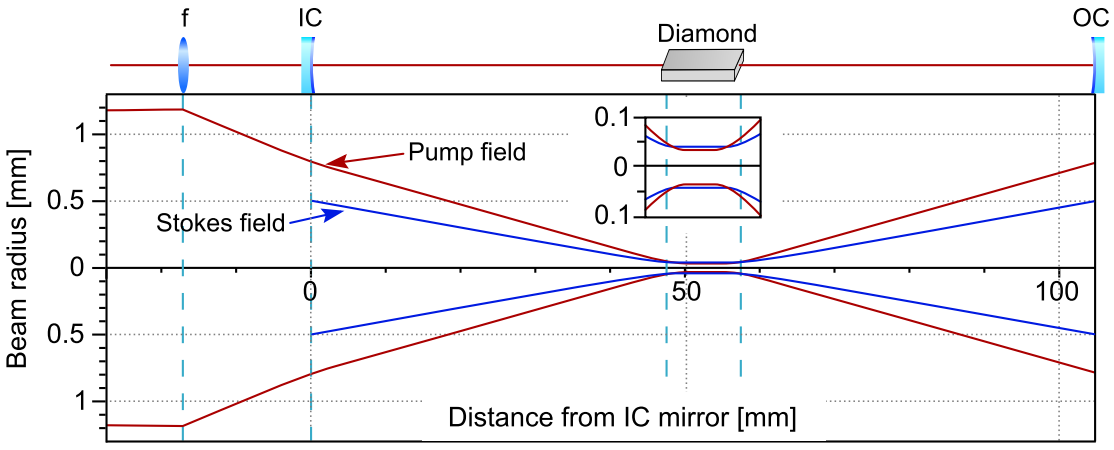

Figure 3.6: Intracavity Stokes and pump field waist radii. On top focusing into the Raman resonator, which is formed by input coupler (IC) and an output coupler (OC).

The resonator, which is symmetric about the diamond, is formed by convex IC and OC of 50 mm curvature. The intracavity-field waist radius and resonator stability diagram, shown in Fig 3.7, are functions of the mirror's displacement. For a 105 mm resonator or shorter the intracavity-field fundamental mode radius is equal to or greater than the pump focus radius. Therefore, after initial alignment, mode-matching optimization is achieved by small adjustments in cavity length.

The resonator stability, defined as [2]

$$0 \leq \left(1 - \frac{L}{r_{\mathrm{IC}}}\right)\left(1 - \frac{L}{r_{\mathrm{OC}}}\right) \leq 1, \tag{3.3}$$

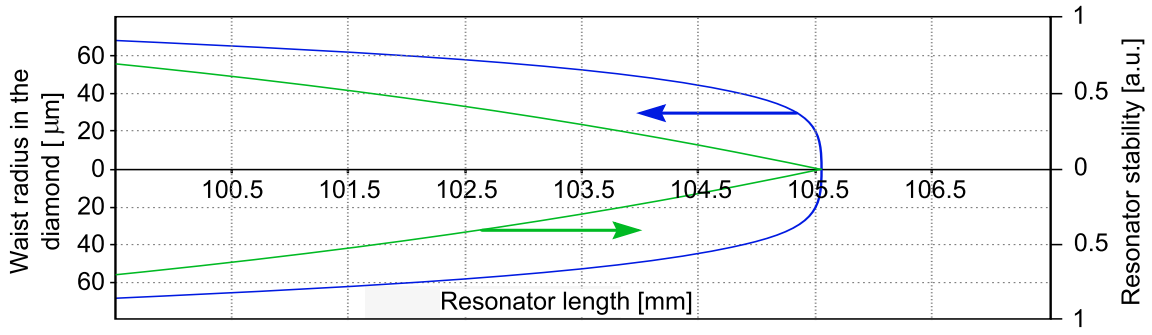

FIGURE 3.7: Waist radius in the center of the cavity and resonator stability as a function of resonator length.

where r_{IC}, r_{OC} are radii of curvature of the input and output coupler, respectively, is around 0.2 for a resonator length of 104.8 mm. A cavity that is so close to the instability point is extremely sensitive to small length changes and mirror alignment. On the other hand, once aligned, it is considerably robust towards thermal lensing in the Raman material. The resonator is destabilized when the thermal lens focal length reaches $\frac{1}{4}$ of the mirror spacing (i.e., ≈25 mm) as shown in Fig. 3.8, which encourages the use of a short resonator. Moreover the waist expands in the diamond for a positive thermal lens as the focal length approaches the stability limit, thus preventing coating damage of the approximately 1-cm-long Raman crystal.

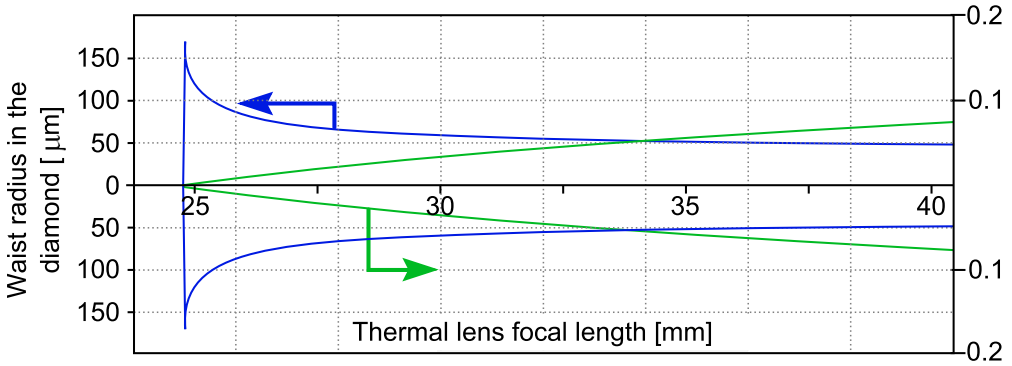

FIGURE 3.8: Waist radius and resonator stability as a function of thermal lens focal length.

Optical coatings for the Raman cavity mirrors were optimized for first Stokes generation and double pass pumping. The IC is transparent for the pump wavelength of 1064 nm ($T_{IC} \geq 96\%$) and highly reflective ($R_{IC} \geq 99.98\%$) at the first Stokes wavelength 1240 nm. The OC is highly reflective for the pump and has 0.43% transmission for the first Stokes. To prevent generation of the unwanted second Stokes component, reflectivity of IC and OC at 1480 nm was minimized. The diamond facets are anti-reflection (AR) coated with minimum reflectivity 1240 nm.

3.4 Continuous wave diamond Raman laser characterization

The experimental arrangement for the external cavity DRL is shown in Fig. 3.9. A half-wave plate and polarizer served as a pump power attenuator. After passing through an optical isolator, a second half-wave plate was used to align the polarisation vector of the pump with one of the diamond's ⟨111⟩ axes. In accordance with the above calculations, a focal length f = 50 mm was chosen for the pump focusing lens. The measured focal spot radius (at $\frac{1}{e^2}$) was ≈32 µm, resulting in an incident intensity of ≈0.8 MW/cm^2 at the threshold of 11.3 W. The pump, residual pump, and Stokes powers were measured by calibrated PIN photodiodes A, B, and C, and a power meter. The length of the resonator was adjusted to 105 mm to mode-match the pump waist sizes.

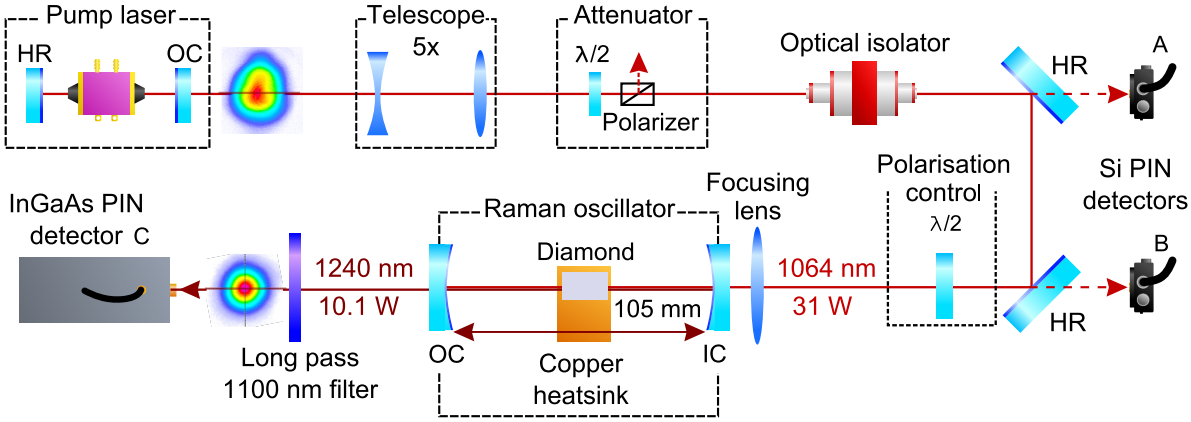

Figure 3.9: Experimental arrangement.

The diamond sample used was a low-nitrogen (≈20 ppb), ultra-low birefringence, type-IIIa, CVD-grown single-crystal (Element6 Ltd) of dimensions 5×9.5×1.2 mm^3. The stress-induced birefringence was between 7×10^{-7} and 3×10^{-6} (measured by the manufacturer using the Metripol method). Anti-reflective coatings were applied to both end-faces (R < 1% at 1064 nm, R < 0.25% at 1240 nm). The linearly-polarised pump beam was incident on the 5×1.2 mm^2 diamond face and propagated along the ⟨110⟩ axis.

Above the threshold of 11.3 W the Stokes output power increased with a slope efficiency of 49.7% (linear fit) as shown in Fig. 3.10. The maximum output power reached 10.1 W for 31 W of incident pump power. Over the operating range, the residual pump power remained approximately constant at around the 10 W level. The conversion efficiency at maximum power was 31.7%. The M^2 parameter improved from 1.6 for the pump to 1.16 (measured by BeamGage profiler) for the Stokes (refer to Fig. 3.9 for far-field images). No optical damage was observed.

The Stokes output exhibited substantial amplitude fluctuations when operated near the Raman laser threshold, but became more stable at higher pump powers when a

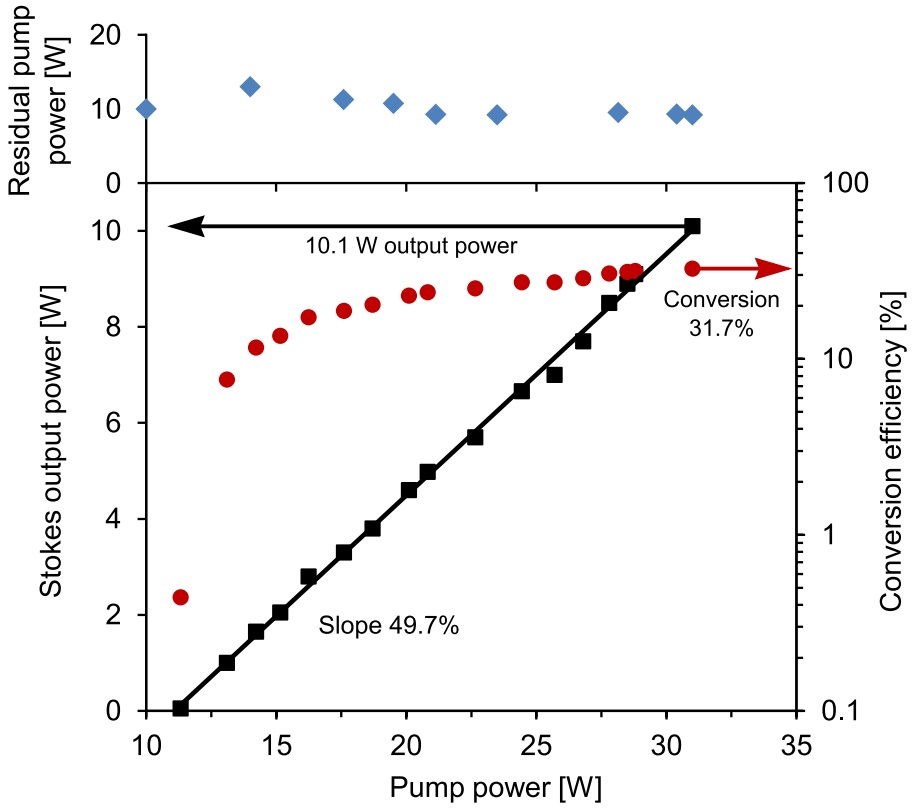

FIGURE 3.10: Stokes power, conversion efficiency and the residual power as a function of incident pump power.

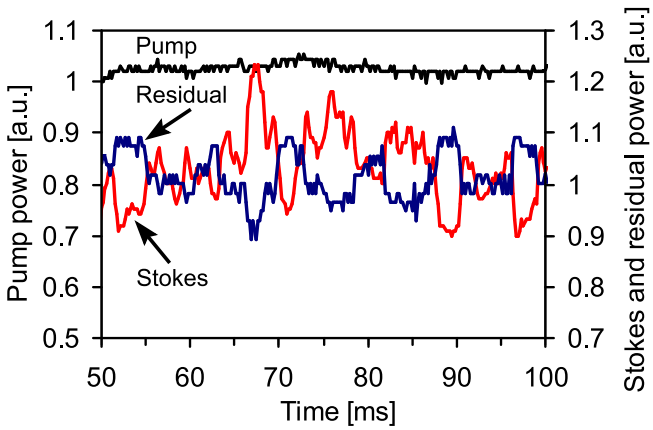

FIGURE 3.11: Stokes output power stability over 100 ms of operation at maximal pump power.

significant portion of the pump beam was depleted. The temporal behaviour near maximum power (Fig. 3.11) shows some fluctuations remaining (about 10% of the average power) correlated with changes in pump depletion. These changes may be caused by mode instabilities observed in the pump laser and mechanical vibrations on the non-isolated optical table.

The output power of 10 W represents a two fold increase in CW output demonstrated by any other crystalline Raman laser. The 50% slope and 32% conversion efficiency are comparable to external cavity pulsed Raman lasers based on conventional Raman crystals; however, almost quantum limited efficiency has been shown in pulsed-pumped diamond [63]. Therefore, factors influencing the efficiency of this CW Raman laser were investigated in detail, as discussed in the following section.

Note that there is significant intracavity Stokes power accumulated in the resonator and focused near the diamond faces, places significant optical stress on the AR coatings. The circulating Stokes power for 10 W output and 0.43% output coupling is 2.3 kW. As the beam profile is expected to be Gaussian, the peak Stokes intensity on the diamond facet (beam radius $\sqrt{2}$ bigger than at the waist) is approximately 80 MW/cm^2. That is above the damage limit of most optical coatings for most other substrates; however, as primary damage mechanism is thermal in this regime, with heat primarily dissipated through the substrate, the much higher thermal conductivity of diamond is expected to enable operation at these greatly elevated intensities.

3.5 Raman laser efficiency limitations

The conversion efficiency of the Raman laser is affected by how much of the pump is depleted during the interaction and by how much of the converted Stokes radiation is divided between output coupling and losses. In the case of Raman fibre lasers, the pump field is often almost completely depleted due to long interaction length. In crystalline Raman lasers, as the pump is only double-passing through the relatively short crystal, the depletion depends more on how far above threshold the laser is operated (refer also to Chap. 4, Eq. (4.14)). Therefore, high levels of depletion are observed in pulsed-pumped Raman lasers where the pump intensity grows rapidly to levels many times above threshold. The CW Raman laser operating three times above threshold, on the other hand, exhibits naturally lower depletion.

When parasitic losses on the pump beam are minimal, the depleted pump power is converted to the Stokes field by stimulated Raman scattering. During the process, power corresponding to the Raman shift is lost to material phonon vibrations. Since the CW Raman laser is in steady-state, the Stokes power converted from the pump exactly equals the power lost due to output coupling and parasitic losses (bundled in the absorption loss coefficient α), whose ratio $T/(T + 2\alpha L)$ defines the useful output. Therefore, the pulsed pumped DRL, using an order of magnitude higher output-coupling (50%) than the roundtrip parasitic loss ($\approx$0.5% for $\alpha = 2 \cdot 10^{-3}$ and 99.8% transmission of the AR coated diamond faces), reached near quantum-limited efficiency [63], whereas in the CW DRL, where output coupling is similar to the roundtrip loss, half of the generated power is lost to absorption and scatter.

Since the external cavity Raman laser setup allows simultaneous measurement of the pump power, back reflected residual pump power, and Stokes output power, it is relatively straightforward to evaluate a power budget for the DRL. Such calculation for the 10 W CW Raman laser is shown in Fig. 3.12. From the pump depletion, which is measured as the change in the residual pump power upon alignment of the Raman

laser cavity (from 31 W to 9.2 W at maximum pump power), the power coupled into the Stokes and phonon fields (21.8 W) is obtained. According to the Raman frequency of diamond (1332 cm^{-1}, or 14.2% of the pump frequency) the power lost to the excitation of optical phonons was deduced to be 3.1 W leaving an upper bound on the optical Stokes power generated to be 18.7 W. Since the measured Stokes output (10.1 W) was 54% of the total Stokes generated, we deduce that the difference (8.6 W) represents the combined parasitic absorption and scatter loss in the diamond.

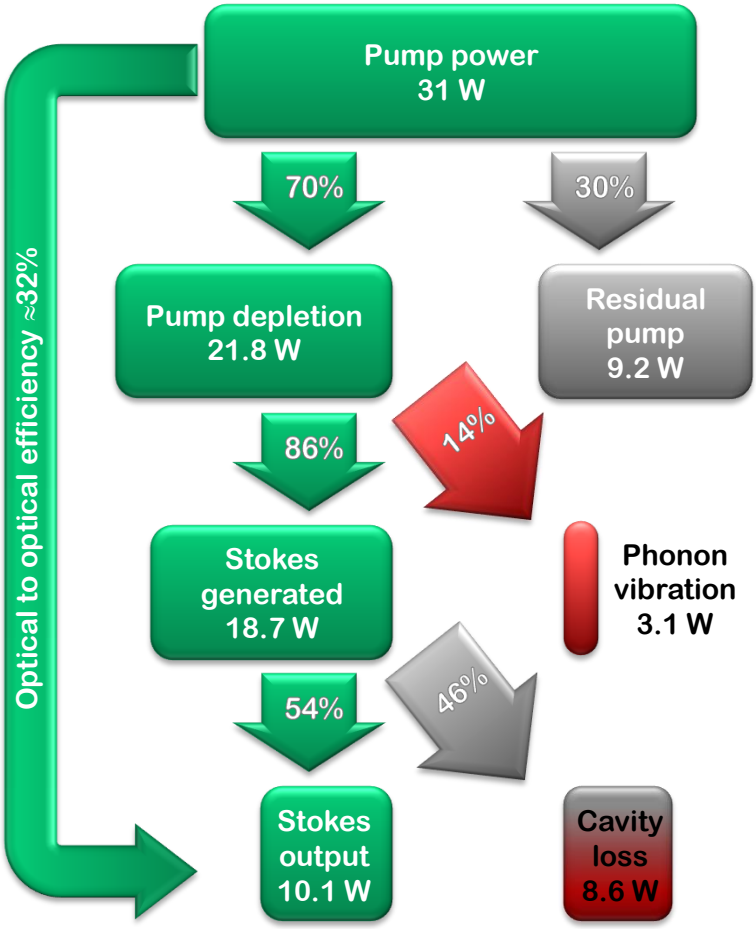

FIGURE 3.12: Power budget calculation of 10 W CW DRL. The intracavity generated Stokes power is divided between useful output and resonator loss due to parasitic bulk absorption and scatter.

Well above threshold, the 46% loss fraction of the generated Stokes power was constant as a function of pump power, suggesting linear absorption and scattering loss processes. Using the output-coupler transmission (T = 0.43%), the Stokes power circulating in the Raman cavity and the combined absorption–scatter coefficient in the diamond at 1240 nm was deduced. As shown in Fig. 3.13, the loss coefficient distributed over the crystal length was 0.17±0.05% cm^{-1} for the investigated range. This is an upper bound of the absorption coefficient as there may be some off-axis

reflections from the diamond facets (parallelism of the diamond samples end faces was about 18 mrad) and bulk scatter loss. Since the loss coefficient is close to the manufacturer's absorption coefficient value of approximately 0.1% cm^{-1} at 1064 nm for low nitrogen (20 ppb) material [50], the diamond bulk absorption is believed to be the main loss mechanism. Although higher efficiency may be obtained by stronger focusing and optimizing the output coupling, the results of this calculation show that the major limitation of this configuration is diamond loss. Improvements in diamond quality are thus expected to enable slope and conversion efficiencies much closer to the quantum limit (86% for pumping at 1064 nm).

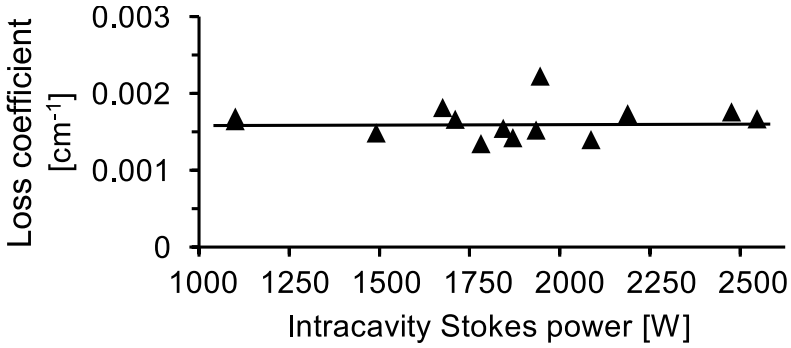

Figure 3.13: Parasitic loss coefficient deduced at different pump powers plotted as a function of intracavity circulating power.

Due to the heating in the crystal that arises from inelastic (Stokes) scattering and parasitic absorption (deduced to be a total of 11.7 W), the efficient operation of the device relies on the excellent thermal handling properties of the diamond. Nevertheless, for further power-scaling, the onset and impact of thermal lensing on Raman conversion must be considered.

3.5.1 Thermal lensing in Raman crystals at high powers

The thermal lens caused by by on-axis heating has been well studied in end-pumped inversion lasers [2]. Techniques developed to deal with thermal loading typically involve better heat management, such as undoped crystal end caps, use of diamond heat spreaders [95], and distribution of the gain media over long lengths, such as fibres, as well as resonator designs incorporating intracavity elements that counteract the lensing effects. However, only some of these techniques are applicable to crystalline Raman converters. The most often used approach has involved the use of compensating elements (see [10, 96–98] and App. A 5 for examples).

The heat deposited in the Raman media originates from inelasticity of the Raman scattering process, as well as residual absorption. A method for mitigating the absorption-induced heating at high powers is to limit the accumulated Stokes power in the resonator by increasing the output coupling. The impact on the laser performance will be two fold. The threshold increases according to Eq. (3.1), and the ratio of loss versus output-coupling changes in favour of the latter, thus increasing slope

efficiency. Modelling, including a detailed study of output power as a function of loss and output-coupling, is presented in Chap. 4.

During the conversion of the depleted pump photons, energy corresponding to the Raman shift of the material is expended on vibrations of optical phonons which couple into acoustic phonons and dissipate as heat. The vibrations are highly damped and their coupling occurs on picosecond time-scales at low acoustic velocities, and therefore is highly localized [99]. The conversion into heat however, may happen over a longer period, allowing the thermal gradient to spread over a larger area than the pump beam size. However, as these thermal dynamics are not yet well understood (and a study of this would be outside the scope of this work) it is assumed here that, to the first order, the Raman heat source is the size of the pump beam. If in reality the temperature gradient occupies a larger area, the thermal lens will be weaker and the calculations comprise an upper bound for the thermal lens. Because the lens is located in the pump beam focus, the lens area does not change significantly even for high pump intensities.

The thermal lens profile established as a result of optical pumping is often considered to be approximately parabolic for end-pumped lasers [100]. Assuming uniform heat deposition over a radius of a beam w, the inverse focal length $1/f$ (i.e., lens strength) of the thermal lens is calculated using a formula for end pumped lasers [2, 41, 56]

$$\frac{1}{f} = \frac{P_{\mathrm{dep}}}{2\pi K\ w^2}\left[\frac{\mathrm{d}n}{\mathrm{d}T} + (n-1)\,(\nu+1)\,\alpha_{\mathrm{T}} + n^3\alpha_{\mathrm{T}}C_{\mathrm{r},\phi}\right], \tag{3.4}$$

where P_{dep} is the heat power deposited in the material, ν is Poisson's ratio, n is the refractive index, K is the thermal conductivity, α_{T} is the thermal expansion coefficient, $C_{\mathrm{r},\phi}$ is the photo-elastic coefficient and $\frac{\mathrm{d}n}{\mathrm{d}T}$ is the dependance of refractive index on temperature change quantifying the thermo-optic effect. As the product of α_{T} and the photo-elastic coefficient is usually notably smaller than $\frac{\mathrm{d}n}{\mathrm{d}T}$ and α_{T} alone, the photo-elastic contribution can be neglected [41]. The increase of the lens strength due to deposited heat power is mitigated, in the work considered here, by mostly the high material thermal conductivity and the lens area defined by the beam size.

Table 3.1 displays the thermo-optical properties of selected Raman crystals, including diamond. The other Raman crystals differ from diamond most starkly in terms of thermal conductivity. From Eq. 3.4, it is apparent that the two to three orders-of-magnitude higher thermal conductivity makes diamond far more suitable for power scaling than alternative crystals.

The lens established in the Raman media due to the Raman quantum defect and the absorption of the Stokes field starts to influence the resonator stability for high pump powers. The stability limit of the near-concentric Raman resonator is compared for diamond and alternative Raman crystals as a function of deposited heat power and pump waist radius in Fig. 3.14 (the blue column indicates total heating deposited in diamond in current setup). In the calculation, the Stokes waist is matched to the pump by adjusting the resonator length (105.5 mm initially) and the stability limit occurs when the lens focal length is shorter than $\frac{1}{4}$ of the resonator length. If the thermal lens is negative, the lens strength is counteracted by focusing of the near-concentric

Table 3.1: Thermo-optical properties of selected Raman crystals [24, 75, 101, 102].

Crystal	Raman shift [cm^{-1}]	Thermal conductivity [$Wm^{-1}K^{-1}$]	dn/dT [$10^{-6}K^{-1}$]	Thermal expansion coeff. [$10^{-6}K^{-1}$]
diamond	1332.3	2000	15	1.1
KGW[i]	768.9	2.6 (a)	-1.5 (a)	2.4 (a)
		3.8 (b)	-1.0 (b)	11 (b)
		3.4 (c)	-1.6 (c)	17 (c)
$Ba(NO_3)_2$	1047.3	1.2 (b)	-20	18
$BaWO_4$	924	3	-9	4–6 (a)
				23 (b)
$GdVO_4$	885	5	3	1.5 (a)
				7.3 (c)

[i] The crystallographic axes of KGW do not coincide with neither the principle axes of the thermooptic tensor, nor the thermal expansion tensor.

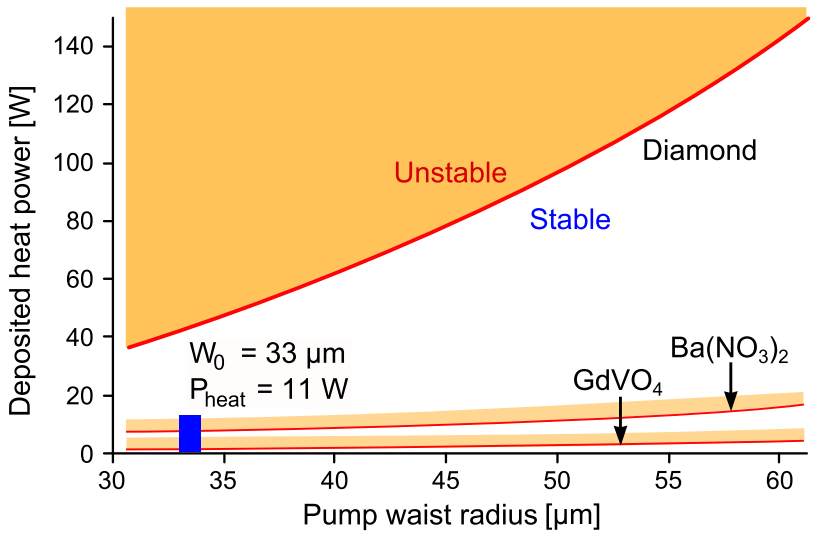

Figure 3.14: Stability limit of a of nearly-concentric Raman resonator as a function of heat deposited in a Raman crystal and pump waist radius.

resonator, thus the cavity remains stable for much stronger negative lensing. For a 33 μm pump waist radius, the allowed heat deposited in diamond is up to 40 W, but only around 5 W for other crystals. As the pump spot increases, the same amount of heat causes a weaker thermal lens, hence the stability region is extended with a slope determined by the thermal properties of the material.

Since the powers deposited in the crystal and the output beam are approximately equal in the present configuration, the cavity is expected to become unstable at approximately 40 W of output power. Linear extrapolation of output power to that level, according to the slope efficiency in Fig. 3.10, would require approximately 70 W of pump power.

3.6 Diamond Raman laser pumping using a 50 W laser

In order to investigate the Raman laser performance at higher pump powers, a second pump laser was designed and constructed. In this section, the pump laser and the resulting performance of a DRL are described.

3.6.1 50 W quasi-continuous Nd:YAG laser design

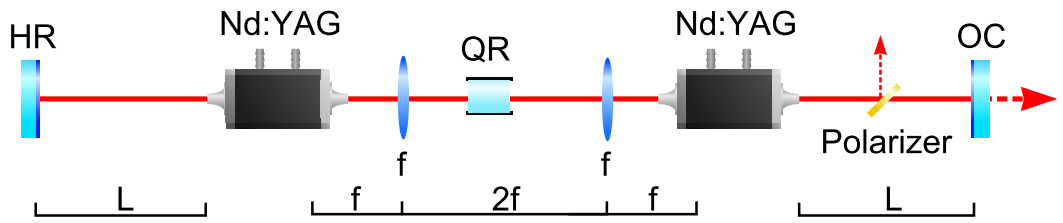

FIGURE 3.15: Design of a 50 W QCW pump laser. HR - high reflector, OC - output coupler, QR - 90° quartz rotator, L - module to mirror distance.

A double Nd:YAG module resonator utilizing standard birefringence compensation scheme was designed to generate a high quality output beam of output power greater than 50 W. The double gain-module Nd:YAG laser configuration is shown in Fig. 3.15. The depolarisation and bifocusing that results from thermally-induced birefringence in Nd:YAG crystals is compensated using a 90° polarisation rotator placed between the laser rods [2]. In order to minimize the aberrations, the principle planes of the thermal lenses induced in the rods are imaged onto each other using a 4f relay-imaging system [103, 104]. A plate polarizer is inserted to ensure linearly-polarised output. The transmission of the output coupler (OC) was 40%.

As mentioned in Sec. 3.2, the rod diameter (3 mm in this case) provides the cavity aperture to discriminate the higher-order spatial modes and enables the efficient generation of a low-M^2 beam. Therefore, the laser was designed to operate stably, in the strong thermal-lens regime, at maximum current. The cavity instability point as a function of pump diode current at, 50% duty-cycle (DC), for different module to mirror distances L is shown in Fig. 3.16. The deduced thermal-lens focal length as a function of pump diode current (see Fig. 3.17) was used to estimate the module-to-mirror distance for high beam-quality operation.

At the maximal diode current of 20 A, the thermal-lens focal length induced in the module is 280 mm (see Fig. 3.17). It was found that increases in length of the flat-flat resonator under maximal thermal loading, resulted in a power roll-off before low-M^2 operation is reached. A convex lens with a focal length of −100 mm was therefore inserted close to the OC (see top of Fig. 3.18). The intracavity waist radius is shown in Fig. 3.18 for a 280 mm thermal lens and L = 225 mm, the conditions for which the

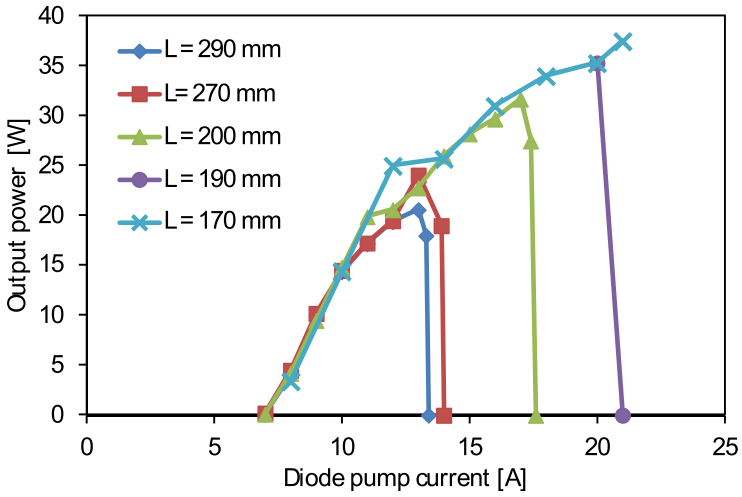

Figure 3.16: Output power rollover with diode current for several values of L.

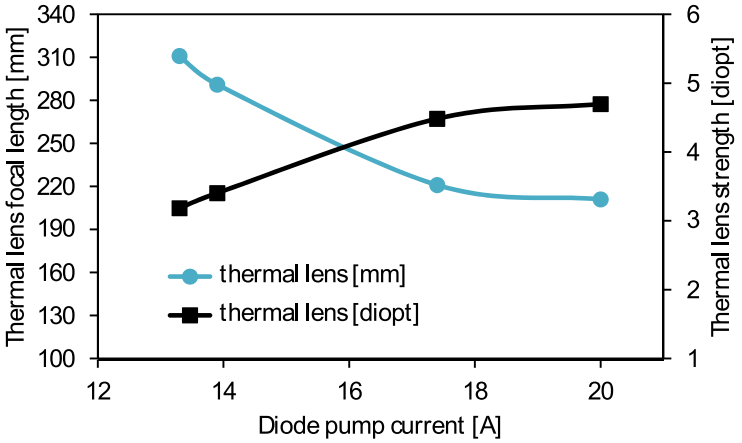

Figure 3.17: Calculated thermal lens strength as function of diode current.

TEM_{00} mode size matches the laser rod. However, the asymmetrical resonator stability as a function of mirror spacing and thermal lensing has two zones where the resonator is stable. Figure 3.19 shows the intracavity waist radius in the rods as a function of cavity length revealing that the waist radius increases to 1.5 mm for a 225 mm rod-mirror separation and a stability parameter of 0.2.

In order to estimate the sensitivity of the resonator to changes in thermal lensing, L was set to 225 mm and the waist radius in the modules is plotted as a function of focal lengths in the laser rods in Fig. 3.20. The calculation shows a narrow stability region (the second region lies outside the view) with waist radius changing from 0.77 to 1.5 mm. For distances between components set according to Fig. 3.18, and for maximum diode current, the intracavity waist and thus mode order can be optimized by small changes in laser repetition rate and duty-cycle (which affects the heat load and thus the lens strength). Upon careful optimization, the laser operates only in a narrow

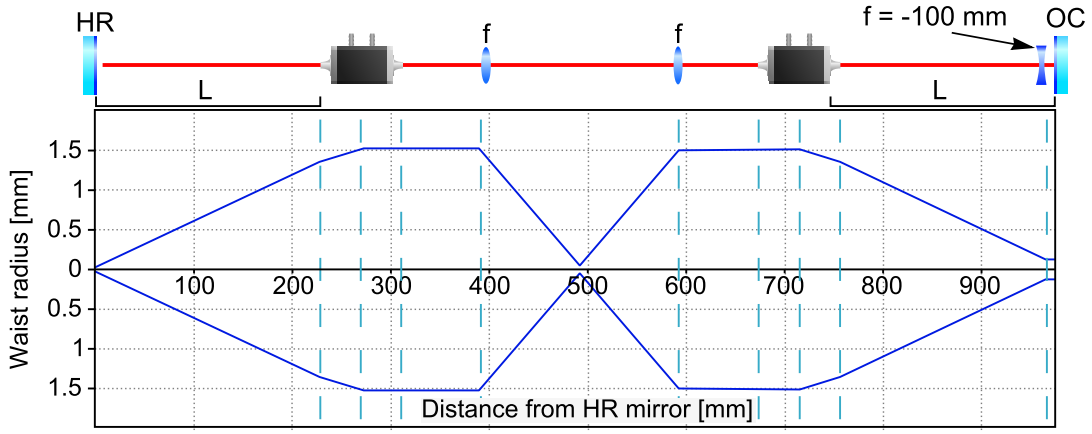

FIGURE 3.18: Calculated TEM_{00} waist radius inside the two module Nd:YAG laser containing a negative lens calculated for maximum pump current.

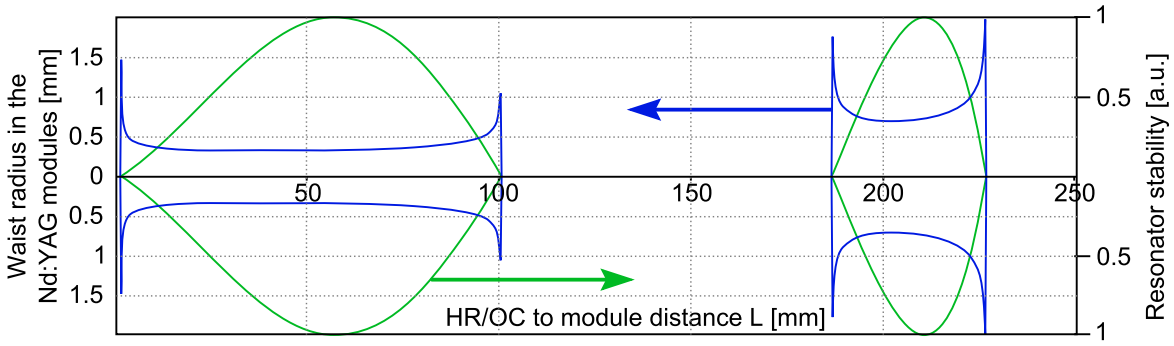

FIGURE 3.19: The resonator stability and waist radius in the Nd:YAG rods as a function of the distance L, calculated for maximum pump current.

window around maximum pump current. Average output power is 24 W at 46.2% duty-cycle generating an on-time QCW power of 52 W in quasi-rectangular pulses of duration 30 ms (Fig. 3.21). The spatial profile of the beam is shown inset to Fig. 3.21. As the laser cavity was set close to the stability limit, and due to the relatively strong thermal lensing in the Nd:YAG rods (double compared to similar CW systems, see for example [105, 106]), the M^2 of the laser beam was approximately 2.0 (determined by BeamGage beam profiler).

3.6.2 Diamond Raman performance characteristics

Raman scattering occurs on picosecond timescale (approximately equal the phonon dephasing time of 6.8 ps in diamond [94]). In KGW the temperature gradients establish within about 30 ms [98] (see App. A 5). Diamond having three orders of magnitude higher thermal conductivity is assumed to reach a steady-state on a microsecond timescale. Therefore, DRL characteristics under conditions of steady-state thermal gradients in the crystal can be studied by investigating behaviour with 30 ms duration

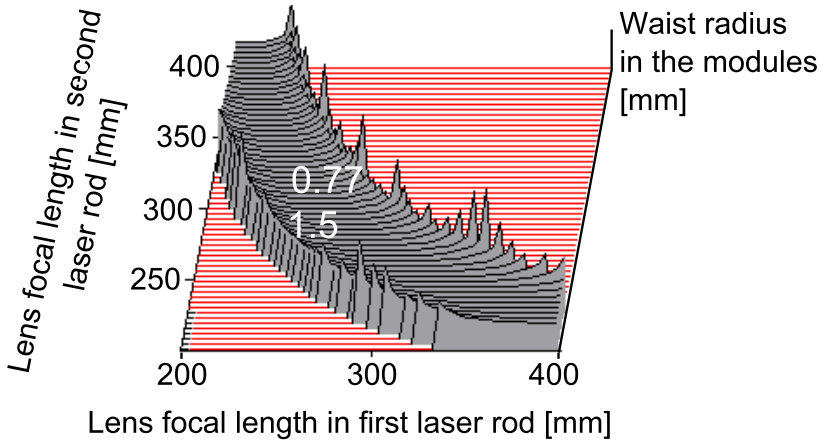

Figure 3.20: The resonator waist radius in the Nd:YAG rods as a function of the focal lengths of the thermal lenses in each module.

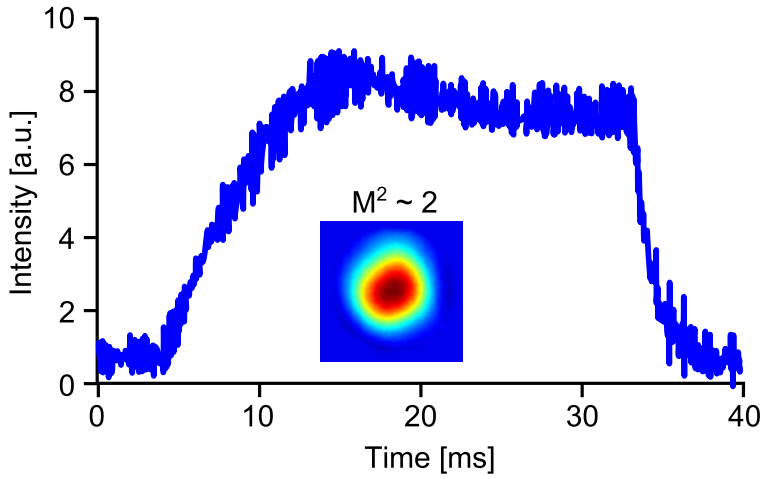

Figure 3.21: Temporal and spatial (inset) profile of the QCW pump laser output at the maximal QCW power of 52 W.

pump pulses. Throughout this Chapter, on-time powers are generally quoted (instead of average powers) as these values are representative of what is likely to be achieved using cw pumping.

For DRL characterization, a similar pumping scheme to that in Sec. 3.4 has been employed. After passing through an optical isolator and a half-plate (the pump polarisation is parallel to diamond's ⟨111⟩ direction), the 50 W QCW pump radiation is focused into the diamond by a 50 mm-focal-length lens resulting in 48 W incident pump power in a 49 µm pump spot radius in the diamond.

The DRL cavity shown in Fig. 3.22 is close to concentric, ensuring good mode-matching of the Stokes and pump fields. The IC has identical transmission and reflectivity to that in Sec. 3.3. The OC was highly reflective for the pump, to provide double pass pumping and had slightly higher (0.5%) transmission at the first Stokes wavelength than the one used previously. The IC and OC radius of curvature were

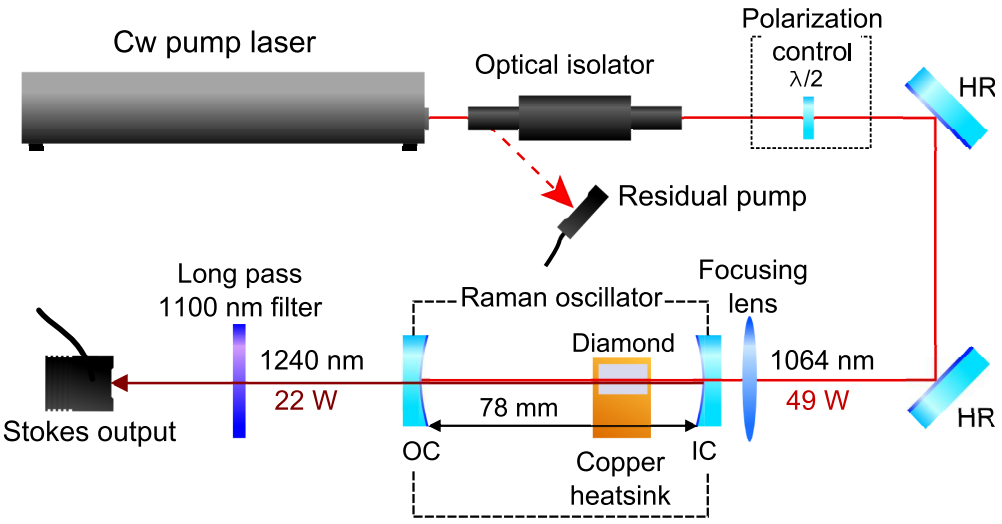

FIGURE 3.22: Experimental setup. Measurement of output Stokes and residual pump power.

25 and 50 mm, respectively, and the cavity length was 78 mm. The diamond used was an $8 \times 4 \times 1\,\text{mm}^3$ sized single-crystal-CVD diamond of identical grade to the one used previously with anti-reflection coatings minimizing reflection at 1240 nm, deposited on both facets.

Figure 3.23 shows the measured Stokes output and conversion efficiency as a function of incident pump power. The threshold is approximately doubled compared to previous measurements; however the linear slope efficiency increased to 77.8% and conversion efficiency to 45%. At the maximum incident pump power of 48 W the generated Stokes output was 21.8 W. The measured residual pump power decreased from 18 W at threshold to about 15 W at full pump power. No power roll-off (which would imply destabilization of the cavity due to thermal lensing) was observed, as expected from the analysis of Fig. 3.14.

The temporal profile of the Stokes output followed the pump pulse as shown in Fig. 3.24. At the maximum pump power, fluctuations in the Stokes amplitude can be correlated to instabilities in the pump laser.

The pump and Stokes spatial profiles were measured to investigate beam quality enhancement due to Raman beam clean up. The spatial distribution of all beams involved, depicted in Fig. 3.25 remained Gaussian. However, the $M^2 = 1.12$ beam parameter obtained for the Stokes beam is a substantial improvement from the pump beam quality.

The threshold of 20 W was higher than expected. Taking the lower beam quality of the pump, the larger pump spot and the slightly higher output-coupling into account predicted a threshold (Eq. (3.1)) of 15 W. The high slope efficiency is partially a result of higher output-coupling but also indicates that parasitic losses were lower than for the previous crystal (see next chapter). The increased threshold may be attributable

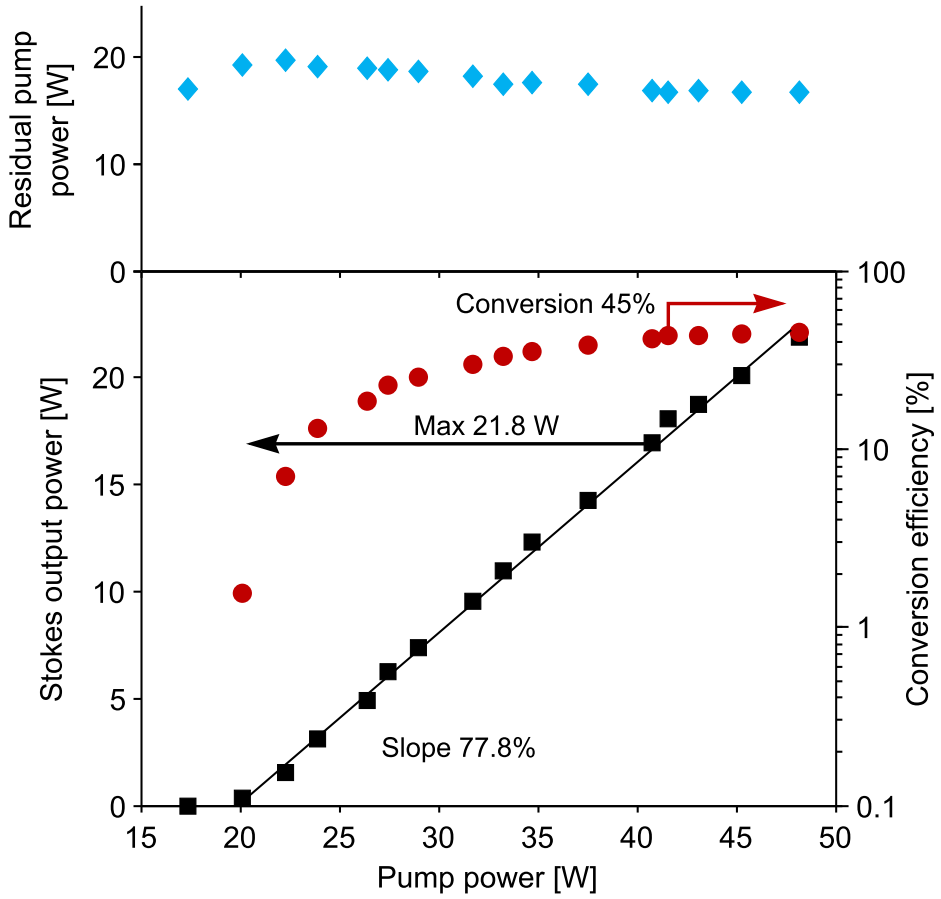

Figure 3.23: Stokes output power, residual pump, and conversion efficiency as a function of incident pump power.

to a higher residual birefringence in the diamond. In the experiment, a half-wave plate was used to ensure that the pump polarisation parallel with a diamond's ⟨111⟩ axis. Depending on the position in the crystal, the measured Stokes polarisation, however, was not always aligned with the pump. It was also observed that threshold and output polarisation properties varied significantly depending on the lateral position of the diamond with respect to the beam. A detailed analysis of Raman laser polarisation behaviour, with significant implications for these results and more generally for DRLs, is presented in Chap. 5.

The lack of output-power saturation indicates that further power-scaling may be possible by increasing the pump power beyond 50 W. At the maximum output power (22 W), the Stokes intracavity circulating power was approximately 4 kW ($I = 55\,MW/cm^2$ on the diamond faces, which is lower than in the previous case due to the bigger pump spot size). Theoretical optimization of the diamond Raman laser is presented in the next chapter.

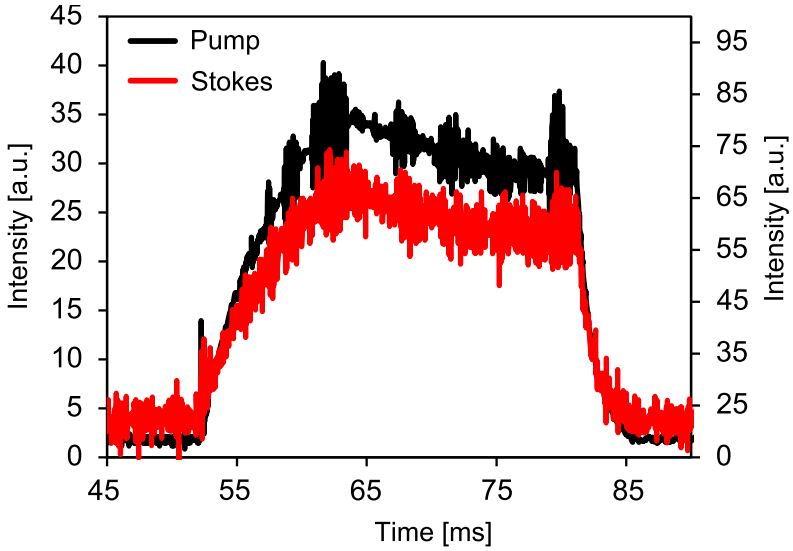

FIGURE 3.24: Stokes and pump temporal behaviour.

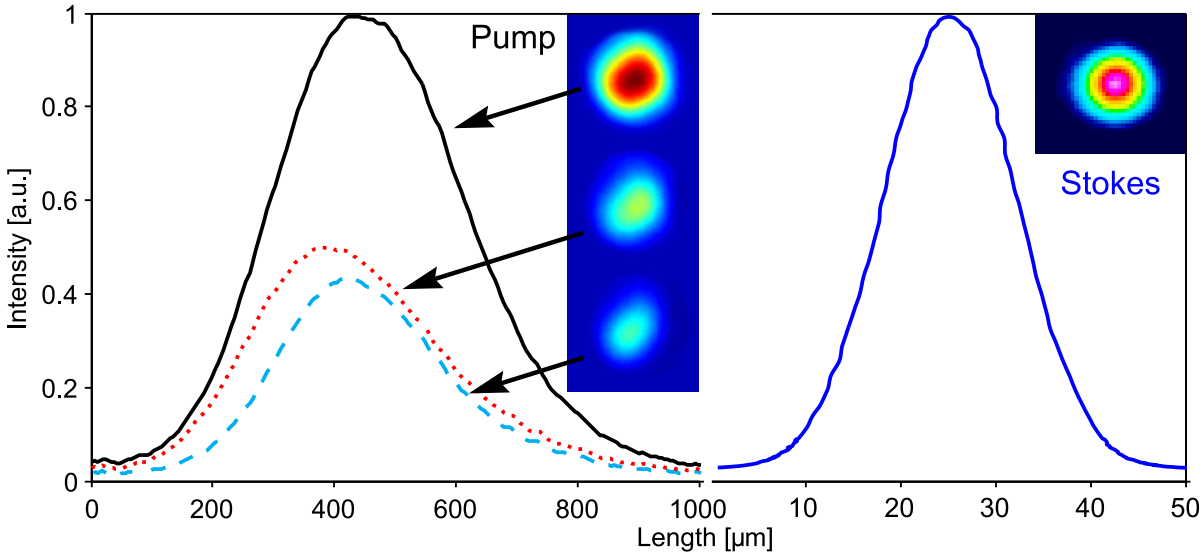

FIGURE 3.25: Intensity profiles of residual pump exiting the diamond (left) and Stokes far-field distribution (right – blue full line), as imaged by the CCD camera. For residual pump profiles: Black full line – at maximum, 48 W pump power, with cavity misaligned for zero Stokes output; blue dashed line – at threshold 18 W; red dotted line – at maximum pump 48 W and maximum Stokes 20 W.

3.7 Conclusion

Development of an extra-cavity quasi CW Raman laser has been presented from initial design, through to efficient and high power operation. A maximum on-time Raman output power of 22 W was demonstrated at a conversion efficiency of 45%. The beam quality improved to $M^2 = 1.08$ from $M^2 = 2$ for the pump.

Analysis of thermal management of Raman crystals revealed that diamond in the

current scheme is able to handle at least five-times higher deposited heat power compared to molecular-ion crystals. Since the Stokes power generated within the Raman resonator is almost equally distributed between output and parasitic loss, close to 70 W of output power, and therefore deposited heat, is theoretically possible before the predicted onset of a limiting thermal-lens. However, the external cavity concept is not limited to this level. Increases in the pump spot size weaken the thermal lens generated, and an increase of output coupling will reduce the heating caused by residual absorption. Both methods lead to an increase in laser threshold, hence a suitable pump laser is required to generate at least three times the threshold power. Higher power and efficiencies are also likely to be obtained as diamond with improved quality becomes available.

The presented high-power and high-efficiency operation of an external cavity CW DRL represents a novel approach for CW Raman laser technology. The key design advantages of a near-concentric resonator, combined with a high-gain Raman crystal with excellent thermal properties (diamond) comprise a power-scalable wavelength conversion approach with small footprint and intrinsically-low spectral broadening (cf., fibres or parametric oscillators). This concept provides a simple add-on device potentially applicable to a range of high power CW laser technologies (including line narrowed fibre lasers and amplifiers, see Chap. 6) and offers further potential for extending the wavelength range via Stokes cascading and subsequent harmonic conversion.

4

Diamond Raman laser optimization

The previous chapter investigated the performance characteristics of an extra-cavity DRL pumped by two lasers with 30 and 50 W of output power. In one case, the power budget calculation suggested that conversion efficiency was limited by loss caused mainly by residual absorption of diamond samples. However, no attempt has been made to improve performance by optimizing other resonator properties such as output coupling and focusing. Here, a mathematical model is used to predict performance as a function of various resonator parameters such as output-coupling, focusing, diamond loss, and diamond length.

In this chapter the steady-state Raman Eqs. (2.49, 2.50) derived in Chapt. 2 are used as a basis of an analytical model describing CW stimulated Raman conversion. The specifics of the CW extra-cavity design (namely, low output coupling and non-resonant pumping) simplify the solution into a single equation describing the Stokes generation. Furthermore, changes in cavity parameters due to thermal lensing can be neglected by virtue of using diamond as the Raman gain medium and athermal nature of the near-concentric resonator.

The model results are compared to the two presented DRLs of Chap. 3. The model is then used to predict the Stokes output power as a function of pump power levels and resonator properties.

4.1 Derivation of analytical model

Following the results of Chap. 2 the pump depletion and Stokes growth in a steady-state limit can be expressed as

$$\begin{aligned} \frac{\mathrm{d}I_{\mathrm{S}}^{\mathrm{int}}(r,z)}{\mathrm{d}z} &= g_{\mathrm{S}} I_{\mathrm{P}} I_{\mathrm{S}}^{\mathrm{int}} - \alpha I_{\mathrm{S}}^{\mathrm{int}}, \\ \frac{\mathrm{d}I_{\mathrm{P}}(r,z)}{\mathrm{d}z} &= -\frac{g_{\mathrm{S}}}{\eta} I_{\mathrm{P}} I_{\mathrm{S}}^{\mathrm{int}} - \beta I_{\mathrm{P}}, \end{aligned} \tag{4.1}$$

where I_{P}, $I_{\mathrm{S}}^{\mathrm{int}}$ are pump and Stokes intracavity intensity, respectively, $\eta = \lambda_{\mathrm{P}}/\lambda_{\mathrm{S}}$ is quantum defect of the inelastic Raman process (e.g, Raman shift), and α, β are parasitic losses at Stokes, pump wavelength, respectively.

When integrating the equations a method similar to [107] is used. It is first assumed that all beams the pump I_{P}, Stokes I_{S}, and residual pump, have the TEM_{00} intensity

distributions

$$I_{\mathrm{P,S}}(r,z) = P_{\mathrm{P,S}}(z)\,\frac{2}{\pi}\frac{1}{w_{\mathrm{P,S}}^2(z)}\exp\left[-2\left(\frac{r}{w_{\mathrm{P,S}}(z)}\right)^2\right]. \tag{4.2}$$

The validity of this assumption is discussed later in Sec. 4.3. The power in the beam with Gaussian profile is then

$$P_{\mathrm{P,S}}(z) = I_{\mathrm{P,S}}(0,z)\,\frac{\pi w_{\mathrm{P,S}}^2(0)}{2}, \tag{4.3}$$

where $I_{\mathrm{P,S}}(0,z)$ is intensity of the pump and Stokes field on the beam axis and it is allowed for the change of the beam radius $w_{\mathrm{P,S}}(z)$ from waist $w_{\mathrm{P,S}}(0)$ due to focusing

$$w_{\mathrm{P,S}}(z) = w_{\mathrm{P,S}}(0)\sqrt{1+\left(\frac{z}{z_{\mathrm{P,S}}}\right)^2}, \tag{4.4}$$

where $z_{\mathrm{P,S}}$ is respective Rayleigh range defined as

$$z_{\mathrm{P,S}} = \frac{\pi n_{\mathrm{P,S}} w_{\mathrm{P,S}}^2(0)}{M_{\mathrm{P,S}}^2 \lambda_{\mathrm{P,S}}}, \tag{4.5}$$

where M^2 is beam quality factor, $\lambda_{\mathrm{P,S}}$ vacuum wavelength and $n_{\mathrm{P,S}}$ index of refraction.

Performing the volume integration of the intensity distributions in polar coordinates (radius r from 0 to ∞, θ from 0 to 2π) is simplified by the assumption that the pump, residual pump after depletion, and Stokes beam transverse distributions are Gaussian. The Eq. (4.1) become (where losses were neglected)

$$\begin{aligned}\frac{\mathrm{d}P_{\mathrm{S}}^{\mathrm{int}}(z)}{\mathrm{d}z} &= \frac{2}{\pi}g_{\mathrm{S}}P_{\mathrm{P}}(z)\,P_{\mathrm{S}}^{\mathrm{int}}(z)\,\frac{1}{w_{\mathrm{P}}^2(z)+w_{\mathrm{S}}^2(z)},\\ \frac{\mathrm{d}P_{\mathrm{P}}(z)}{\mathrm{d}z} &= -\frac{2}{\pi}\frac{g_{\mathrm{S}}}{\eta}P_{\mathrm{P}}(z)\,P_{\mathrm{S}}^{\mathrm{int}}(z)\,\frac{1}{w_{\mathrm{P}}^2(z)+w_{\mathrm{S}}^2(z)}.\end{aligned} \tag{4.6}$$

In order to solve one of the Eqs. (4.6) one has to assume that either the Stokes intracavity power or pump does not change significantly across the resonator length. Once above threshold the strong depletion of the pump cannot be neglected. The intracavity Stokes power, on the other hand, can be assumed to be constant over the resonator due to the low round-trip gain and loss of this high-Q Raman resonator. For I_{S} independent of z the equation for pump depletion can be solved by separation of variables (integral from $-L/2$ to $L/2$, where L is interaction length) with exponential solution

$$P_{\mathrm{P}}\left(-\frac{L}{2}\right) = P_{\mathrm{P}}\left(\frac{L}{2}\right)\exp\left(-GP_{\mathrm{S}}^{\mathrm{int}}\right), \tag{4.7}$$

where

$$G = \frac{g_{\mathrm{S}}}{\eta}\frac{\arctan(C)}{D}, \tag{4.8}$$

and

$$C = \frac{L}{2}\sqrt{\frac{\left(\frac{w_{\mathrm{P}}(0)}{z_{\mathrm{P}}}\right)^2 + \left(\frac{w_{\mathrm{S}}(0)}{z_{\mathrm{S}}}\right)^2}{w_{\mathrm{S}}^2(0) + w_{\mathrm{P}}^2(0)}},$$
$$D = \frac{\pi}{4}\sqrt{\left(w_{\mathrm{S}}^2(0) + w_{\mathrm{P}}^2(0)\right)\left[\left(\frac{w_{\mathrm{P}}(0)}{z_{\mathrm{P}}}\right)^2 + \left(\frac{w_{\mathrm{S}}(0)}{z_{\mathrm{S}}}\right)^2\right]}. \tag{4.9}$$

The Raman gain in focused geometry G is identical to Boyd's analysis of threshold in extra-cavity gas Raman lasers [107]. The $P_{\mathrm{P}}(-L/2)$ is the pump power P_{P} and $P_{\mathrm{P}}(L/2)$ is the residual power after depletion P_{Res}.

The generated Stokes power $P_{\mathrm{S}}^{\mathrm{gen}}$ is the difference between pump and residual pump power scaled by the Raman shift and in steady-state must replenish all resonator losses $P_{\mathrm{S}}^{\mathrm{loss}}$ due to output coupling $P_{\mathrm{S}}^{\mathrm{oc}}$ and other mechanisms

$$\begin{aligned} P_{\mathrm{S}}^{\mathrm{gen}} &= \frac{\lambda_{\mathrm{P}}}{\lambda_{\mathrm{S}}}\left(P_{\mathrm{P}} - P_{\mathrm{Res}}\right), \\ &= \frac{\lambda_{\mathrm{P}}}{\lambda_{\mathrm{S}}} P_{\mathrm{P}}\left[1 - \exp\left(-G P_{\mathrm{S}}^{\mathrm{int}}\right)\right] = P_{\mathrm{S}}^{\mathrm{oc}} + P_{\mathrm{S}}^{\mathrm{loss}}. \end{aligned} \tag{4.10}$$

In a linear Raman resonator, half of the total intracavity Stokes power propagates in left and half in right direction. Therefore the out-coupled Stokes power is

$$P_{\mathrm{S}}^{\mathrm{oc}} = \frac{T}{2} P_{\mathrm{S}}^{\mathrm{int}} \Rightarrow P_{\mathrm{S}}^{\mathrm{int}} = \frac{2}{T} P_{\mathrm{S}}^{\mathrm{oc}}. \tag{4.11}$$

Introducing surface $\acute{\gamma}$ and bulk γ scatter loss and bulk absorption loss α

$$P_{\mathrm{S}}^{\mathrm{loss}} = \left[\acute{\gamma} + (\gamma + \alpha) L\right] P_{\mathrm{S}}^{\mathrm{int}} = \frac{2\left[\acute{\gamma} + (\gamma + \alpha) L\right]}{T} P_{\mathrm{S}}^{\mathrm{oc}}. \tag{4.12}$$

Assuming the major parasitic loss is bulk absorption, substitution of (4.11), (4.12) into (4.10) leads to a solution predicting the pump power needed for a certain Stokes output.

$$P_{\mathrm{P}} = \frac{T + 2\alpha L}{\eta T} P_{\mathrm{S}}^{\mathrm{oc}}\left[1 - \exp\left(-\frac{2G}{T} P_{\mathrm{S}}^{\mathrm{oc}}\right)\right]^{-1}. \tag{4.13}$$

It is possible to find inverse solution to (4.13) in terms of the Omega (also called the Lambert W) function, however it does not provide any further insight into the problem. Combining Eqs. (4.7), (4.11) and (4.12) provides expected residual pump power

$$P_{\mathrm{Res}} = P_{\mathrm{P}} \exp\left(-\frac{2G}{T} P_{\mathrm{S}}^{\mathrm{oc}}\right) = P_{\mathrm{P}} - \frac{T + 2\alpha L}{\eta T} P_{\mathrm{S}}^{\mathrm{oc}}. \tag{4.14}$$

The slope of the output characteristics in a limit of infinite pump equals the maximum conversion efficiency σ

$$\sigma = \frac{\eta T}{T + 2\alpha L}. \tag{4.15}$$

For the gain medium without parasitic loss the efficiency will be limited by the quantum defect of the Raman process η.

The generation threshold $P_{\mathrm{P}}^{\mathrm{thr}}$ is obtained by limiting the Stokes output in (4.13) to zero

$$P_{\mathrm{P}}^{\mathrm{thr}} = \frac{T + 2\alpha L}{2g_{\mathrm{S}} \cdot \arctan(C)} D. \tag{4.16}$$

This general expression accounts for different focusing of the pump and Stokes beams. The optimal ratio of the pump and Stokes confocal parameters $b_{\mathrm{P,S}} = 2z_{\mathrm{P,S}}$ minimizing the generation threshold is shown in Fig. 4.1. The optimal ratio of $b_{\mathrm{P}}/b_{\mathrm{S}} = 0.38$ agrees with Boyd's threshold optimizing calculation [107] and is a result of taking into account focusing of Gaussian beams.

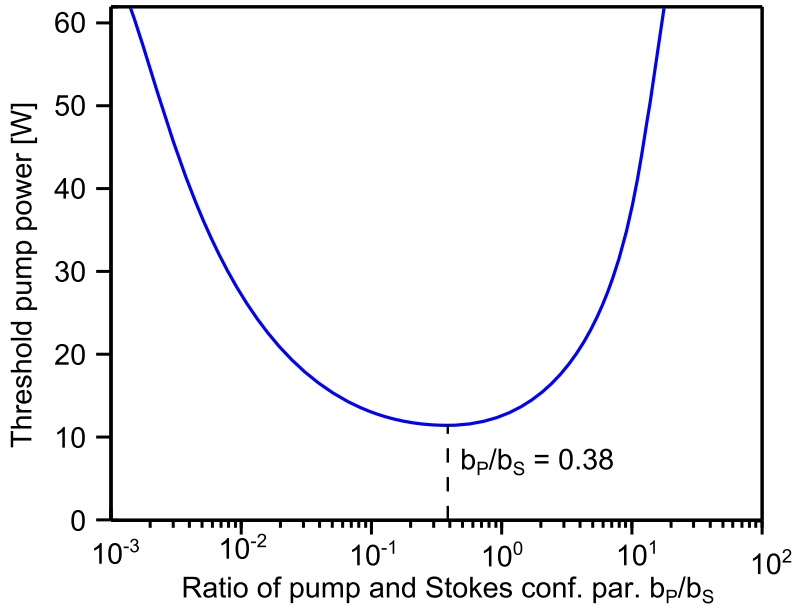

FIGURE 4.1: Stokes generation threshold as a function of pump and Stokes confocal parameters for arbitrary model parameters.

The generation threshold solution can be greatly simplified by assuming that the pump and Stokes fields confocal parameters are the same length b, $M_{\mathrm{P}}^2 \approx M_{\mathrm{S}}^2$, and $n_{\mathrm{P}} \approx n_{\mathrm{S}}$.

$$\begin{aligned} P_{\mathrm{P}}^{\mathrm{thr}} &= \frac{T + 2\alpha L}{2g_{\mathrm{S}} \cdot \arctan\left(\frac{L}{b}\right)} \frac{\pi}{b} \frac{w_{\mathrm{P}}^2 + w_{\mathrm{S}}^2}{2} \\ &= \frac{T + 2\alpha L}{2g_{\mathrm{S}} \cdot \arctan\left(\frac{L}{b}\right)} \frac{\pi w_{\mathrm{P}}^2 (\lambda_{\mathrm{P}} + \lambda_{\mathrm{S}})}{2b\lambda_{\mathrm{P}}}, \end{aligned} \tag{4.17}$$

which accounts for the difference in waist sizes of the pump and Stokes fields of the same confocal parameter. For the case, that the pump and Stokes fields are collimated (i.e., $z_{\mathrm{P,S}} >> L$) and their waists are the same size in (4.16), the threshold formula reduces to

$$P_{\mathrm{P}}^{\mathrm{thr}} = \frac{T + 2\alpha L}{2g_{\mathrm{S}} L} \pi w_{\mathrm{P}}^2(0). \tag{4.18}$$

This result is equivalent to a threshold analysis of collimated beam with top-hat transverse profile.

When a portion of the residual pump is reflected back to the Raman medium it experiences additional depletion. Assuming that the residual pump follows exactly the same path during the second pass, the double pass residual pump $P_{\mathrm{Res}}^{\mathrm{dp}}$ from (4.14) becomes

$$P_{\mathrm{Res}}^{\mathrm{dp}} = RP_{\mathrm{P}} \exp\left(-\frac{4G}{T} P_{\mathrm{S}}^{\mathrm{oc}}\right) \tag{4.19}$$

For OC reflectivity of $R = 1$ at the pump wavelength, and for the current design in which the cavity is concentric, the output characteristic and threshold will be

$$P_{\mathrm{P}} = \frac{T + 2\alpha L}{\eta T} P_{\mathrm{S}}^{\mathrm{oc}} \left[1 - \exp\left(-\frac{4G}{T} P_{\mathrm{S}}^{\mathrm{oc}}\right)\right]^{-1}, \tag{4.20}$$

$$P_{\mathrm{P}}^{\mathrm{thr}} = \frac{T + 2\alpha L}{4 g_{\mathrm{S}} L} \pi w_{\mathrm{P}}^2 (0)\,. \tag{4.21}$$

Therefore the generation threshold is half compared to single pass pumping but the slope efficiency does not change.

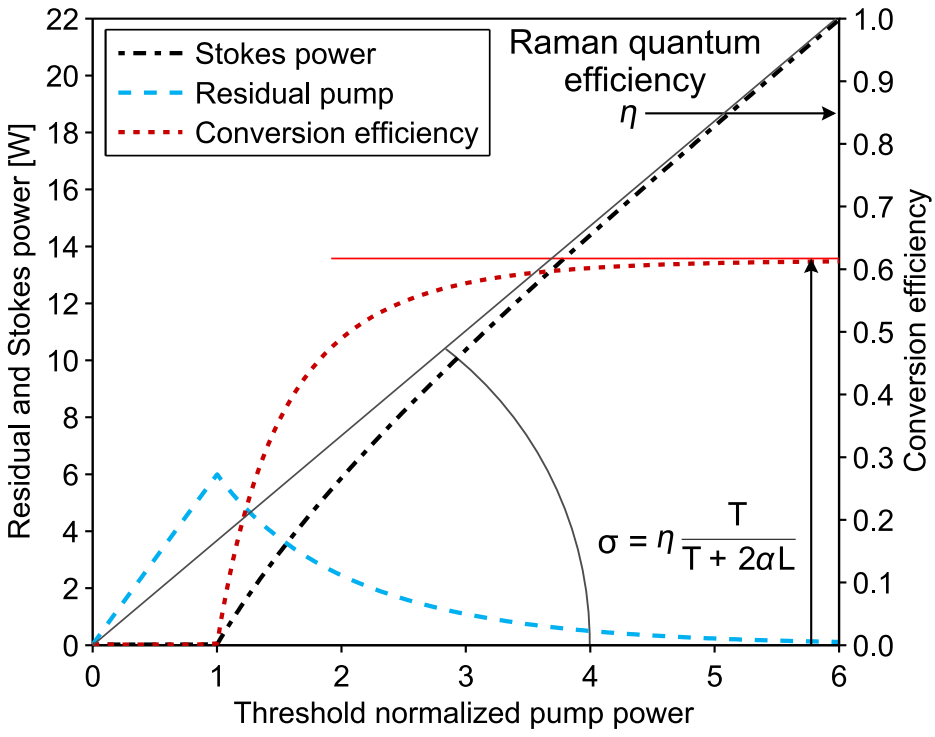

Figure 4.2: DRL output power, conversion efficiency and residual pump power as a function of pump power. The maximal conversion and slope efficiencies σ are limited by the intracavity loss.

The results of Eqs. (4.19) and (4.20), normalized to the laser threshold, together with conversion efficiency for arbitrary set of parameters are shown in Fig. 4.2. The

output power does not increase linearly but as an inverse function of (4.20). For operation far above threshold the Stokes output growth is linear according to

$$P_{\mathrm{P}} = \frac{T + 2\alpha L}{\eta T} P_{\mathrm{S}}^{\mathrm{oc}}. \tag{4.22}$$

4.2 Relationship with previous Raman laser models

Raman lasers has been extensively studied in the past and several different models have been introduced. When pulse pumping is involved most of these solve differential Raman laser rate equations numerically for several generated Stokes orders[108]. Due to the non-equilibrium nature of the equations, this approach is not easily comparable to the steady-state model derived here.

CW Raman laser models have also been developed for limited number of cases. A simplified plane-wave numerical model averaging the gain and loss over the cavity round-trip was derived for intracavity Raman lasers with power dependent harmonic conversion used as means of Stokes output coupling [109]. However, the conversion in CW intracavity Raman lasers is complex due to the interactive nature of inversion and Raman gain in the cavity. Therefore the model, although steady-state, is difficult to compare to the CW extra-cavity DRL model.

Closer to the approach used in this work is theoretical treatment of resonantly pumped gas Raman lasers. Steady-state analytical models have been developed concurrently by Repasky et al. [110] and Peterson et al. [111]. Here only the former approach is introduced as both lead to equivalent conclusions. The model was later modified to accommodate mirrors with asymmetric reflectivities [28] and used as a basis for derivation of time dependent rate equations [7]. The conversion to the Stokes field was calculated using the difference between pump and residual pump fields [28, 110]. The main difference compared to the single resonant extra-cavity Raman laser described here is that the pump field was assumed constant as a function of the longitudinal cavity coordinate due to its resonance within the cavity.

It has been shown that even at low output powers (below 100 mW) the heat generated in the gas due to the inelasticity of Raman scattering creates steep index gradient across the mode volume [100]. The resulting thermal lensing leads to expansion of the beams which decreases the gain and increases the circulating pump power. Steady-state solutions of the Raman laser rate equations including the power dependent lens duct formed in the Raman medium have been derived and solved numerically [100].

In the case that the pump wave is not resonated in the cavity (e.g., single or double pass pumping) its depletion on passage through the resonator must be taken into account. A basic model predicting and optimizing threshold has been introduced by Lisinetskii et al. [25]. The results agree with Boyd's [107] derivation and optimization of threshold of Raman lasers. The threshold increases proportionally to cavity loss and lowering of beam quality and decreases with crystal length but level off when the length is much longer than beams confocal parameter. As far as the author is aware a full analytical solution describing a non-resonantly pumped CW external cavity Raman

laser taking into account pump depletion and focusing of the Gaussian pump and Stokes fields as presented here has not yet been published.

4.3 Model comparison with experiment

The analytical model predictions are compared to output power characteristics of the two demonstrated DRLs of Chap. 3. All measurable parameters such as output coupling and pump spot size are substituted in the equation and diamond loss and gain coefficients are used as free variables to fit the threshold and slope efficiency. Limitations of the model are discussed.

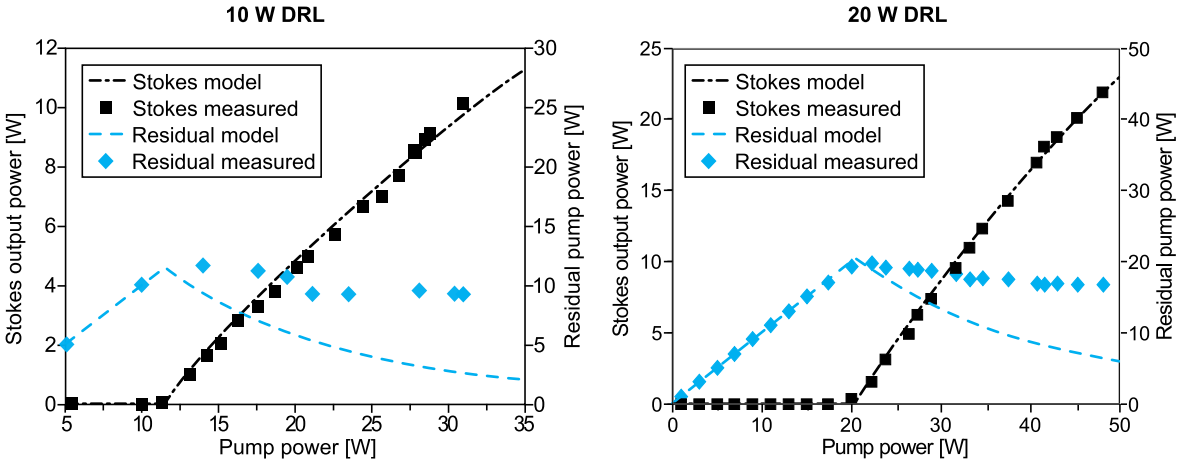

Figure 4.3: Comparison of the model with the experimental results of the 10 and 20 W DRLs. The fitting curves were calculated using Eq. (4.20) and parameters summarized in Tab. 4.1.

Figure 4.3 shows the measured Stokes output and residual pump power of the 10 and 20 W DRL compared with Eqs. (4.20) and (4.21) for parameters summarized in Table 4.1. As can be seen in both cases the modelled threshold and slope fit reasonably well. The slope efficiency, according to Eq. 4.15 depends only on resonator losses. As the output coupling and crystal length are well known, the parasitic absorption α is used as an adjustable parameter to fit the measured output power. The higher slope efficiency in the 20 W DRL compared to the 10 W system can be explained by lower absorption coefficient ($0.17\%\,\mathrm{cm}^{-1}$ compared to $0.28\%\,\mathrm{cm}^{-1}$) of the diamond sample and increased output coupling. Both values of α are within the range expected for diamond samples with 20 ppb nitrogen content as shown in Fig. 2.7.

The DRL threshold depends on resonator loss, Raman gain coefficient and pump and Stokes focusing properties (Eq. (4.16)). The cavity round-trip loss is defined by the slope efficiency and pump and Stokes beams characteristics are measured. Therefore, the Raman gain coefficient g_S is the only relevant free variable. In order to fit the measurement thresholds, gain coefficients of 9 cm/GW and 7.5 cm/GW were required

TABLE 4.1: Simulation variables used to model the 10 and 20 W extra-cavity DRLs.

Variable	10 W DRL	20 W DRL
α [10^{-2} cm^{-1}]	0.28	0.17
g_S [cm/GW]	9	7.5
T [%]	0.42	0.5
L [mm]	9.5	8
w_S [µm]	32	49
M_P^2	1.67	2
λ_P [nm]	1064	1064
λ_S [nm]	1240	1240
σ [%]	34.4	55.6

for the two DRLs having the 10 W and 20 W thresholds. The reported Raman gain coefficient of diamond ranges from 8 to 17 cm/GW [41, 92] for 1064 nm pumping, thus this work supports a gain coefficient at the lower end of this range.

The most notable discrepancy between model and observations appears in the residual pump. The calculated residual pump power above threshold approaches zero more rapidly with increased pump than the measured values. Performing the analytical integration preserves the Gaussian profiles of all the beams and the depletion is constant over the pump beam cross-section. However, the conversion rate is proportional to the intensity across the beam thus depletion of the pump beam centre is expected to be much stronger. The residual pump beam remains Gaussian as shown in Fig 3.25, despite strong depletion in the central part of the beam. This effect is attributed to the tight focusing of the pump beam and the resulting impact of diffraction on smoothening the beam profile. The net result is an axially-peaked pump beam that develops with progressively increased M^2. To include the dependance of the M^2 parameter of the residual pump on the depletion into current model is not trivial and would require to correctly model a diffraction of arbitrary interacting beams. In addition, stress-induced birefringence is shown to greatly affect the oscillating Stokes polarisation and the Raman gain in Chap. 5. Due to neglected diffraction and polarisation effects the residual beam is not depleted as strongly as predicted above threshold. To compensate for the excessive depletion, the model slightly underestimates the gain and loss coefficients.

4.4 Diamond Raman laser optimization

The analytical model describes well the threshold and slope efficiency with reasonable g_S and α parameters. Therefore, it was used to study the principal factors that govern DRL behaviour, as well as to find optimal zones of operation, tolerances on cavity and diamond material parameters, and how to modify design for optimal operation when higher pump powers are available.

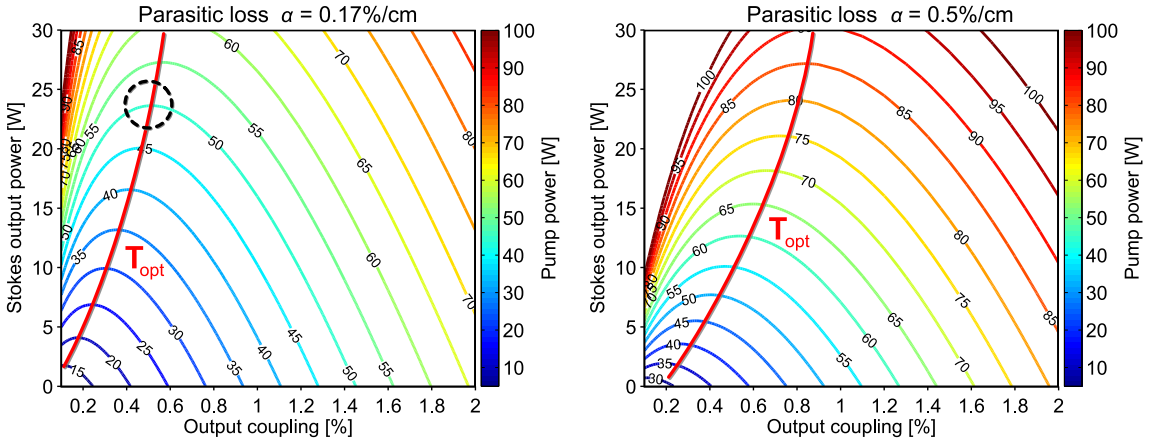

Figure 4.4: Stokes output power as a function of output coupling calculated at different pump powers for two different parasitic absorption coefficients. The red line indicates optimal value of output coupler transmission T_{opt} maximizing Stokes output power. The dashed circle indicates the point of operation of the 20 W DRL.

Figure 4.4 shows the output power dependence on output coupling for the operating conditions of 20 W DRL described in Chap. 3 (second column Tab. 4.1).

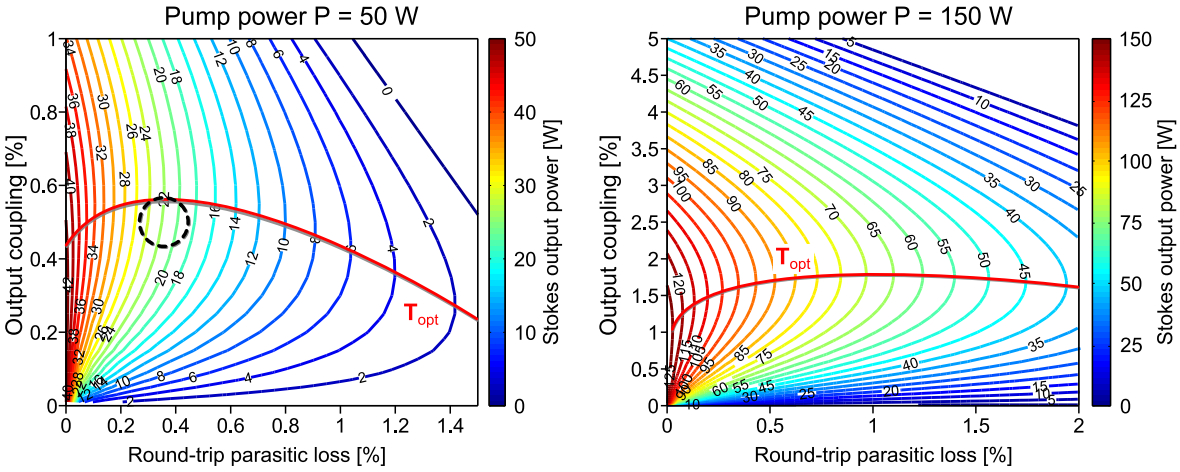

Figure 4.5: Stokes output power as a function of output coupling and round-trip loss calculated for 50 W and 150 W of pump power. The red line shows optimal output coupler transmission maximizing Stokes output power and the dashed circle indicates the point of operation of the 20 W DRL.

To evaluate the influence of parasitic loss on the Raman laser performance, Stokes output power is shown as a function of output coupling and round-trip losses in Fig. 4.5. For fixed pump power, the Stokes output power increases for lower loss as expected. The optimal output coupling increases for round-trip losses $< 0.3\%$. For higher loss, however, the output coupling has to be lowered to achieve the highest output possible at 50 W pump power. At three times higher pumping level, losses have less impact and beyond a certain point there is no large benefit in changing the output coupling.

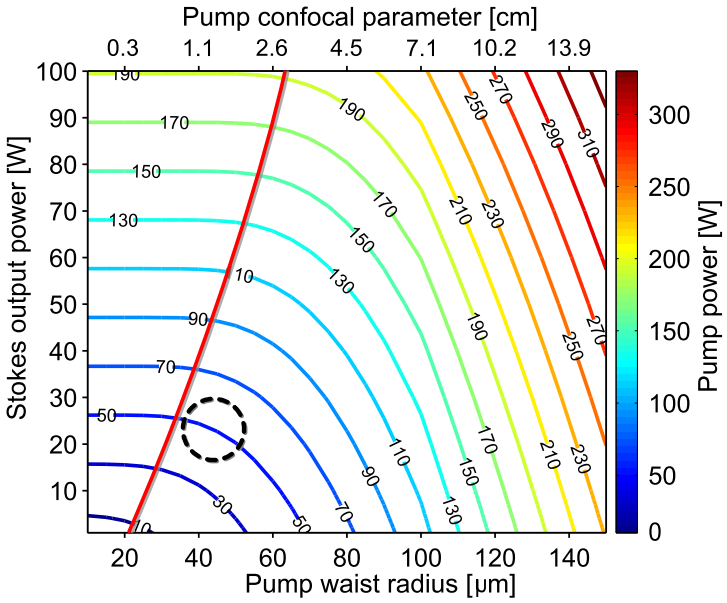

FIGURE 4.6: Stokes output power as a function of pump waist radius (bottom axis) for different pump power. Top axis shows corresponding pump beam confocal parameter. The red line shows maximal Stokes output power and pump waist radius at particular pump powers and the dashed circle indicates the point of operation of the 20 W DRL.

The focal spot-size of the pump beam (assuming mode-matched Stokes) is one of the most important design variables as the intensity scales quadratically with the beam radius. On one hand a small pump spot is desired to lower generation threshold, whereas higher laser intensity increases thermal-lens strength and may lead to damage of the optical coatings at higher pump powers. Fig. 4.6 shows that for a fixed Raman crystal length (8 mm) and output coupling (0.5%), and matched pump to Stokes waist ratio, the Stokes output power saturates and further decreases in spot size do not lead to any further significant increases in output. The red curve indicating operating conditions close to maximum output, and with large pump waist size, highlights conditions for which near maximum efficiency can be obtained while minimizing pump (and Stokes) intensity on the crystal facets thus easing the stress on diamond anti-reflection coating. The main effect of spot-size is to alter the gain and thus laser threshold. Therefore once operating well above threshold, the slope efficiency and power approach common values as shown in Fig. 4.7.

Assuming fixed focusing (in this case $w_0 = 49\,\mu m$) the crystal length can be optimized with respect to resonator loss. The crystal length that maximizes Stokes output is shown in Fig. 4.8 for two different output couplings. The curve of optimal length L_{opt} indicates that longer crystals can be used at higher output couplings. Increase of parasitic loss (due to diamond absorption and scatter loss for example) on the other hand (see Fig. 4.9) forces the use of shorter crystals.

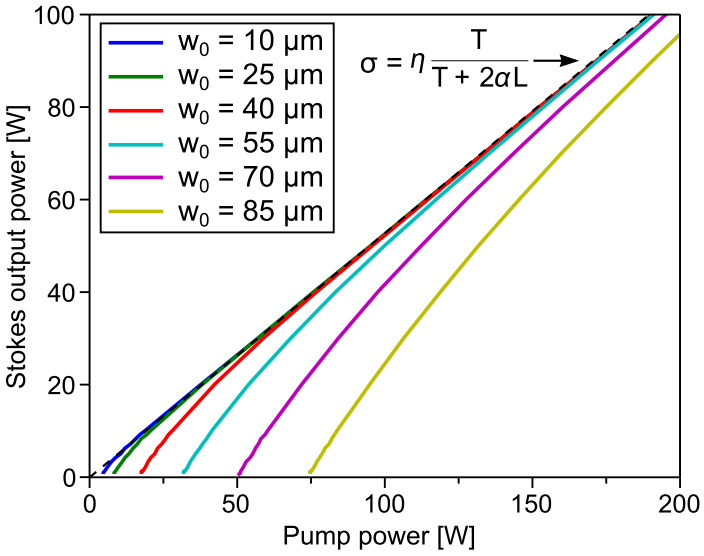

Figure 4.7: Stokes output power as a function of pump power for a range of pump spot sizes.

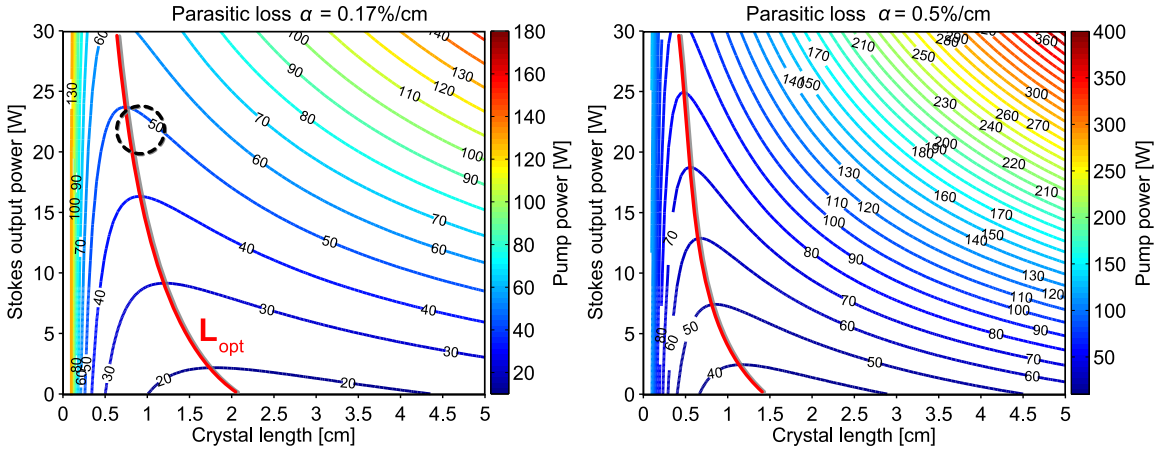

Figure 4.9: Stokes output power as a function of crystal length calculated at different pump powers for loss parameters $\alpha = 0.17\%\text{cm}^{-1}$ and $0.5\%\text{cm}^{-1}$. The red curve L_{opt} shows optimal length of the crystal. The dashed black circle indicates the operation point of the 20 W DRL.

The optimization analysis presented is valid provided that thermal lensing in the diamond does not significantly change the pump and Stokes waist sizes. As established in Chap. 3, the current resonator is expected to withstand at least 70 W deposited heat before thermal lensing significantly affects resonator stability. For the present experimental arrangement, approximately 45% of the output Stokes power is deposited as heat in the crystal, thus power-scaling to output powers beyond 100 W is likely to see the emergence of thermal effects. Note that much higher powers than 100 W are expected by using system designs with enlarged pump and Stokes spot sizes as well as higher output coupling. These measures will also mitigate the risk of diamond coating damage.

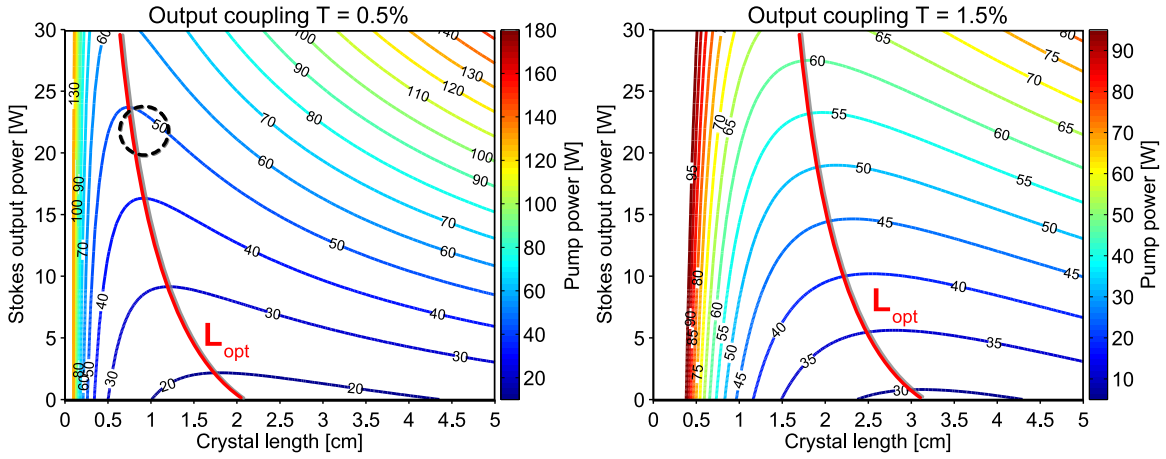

FIGURE 4.8: Stokes output power as a function of crystal length calculated at different pump powers for output coupling values of 0.5% and 1.5%. The red curve L_{opt} shows optimal length of the crystal and the dashed black circle the operation point of the 20 W DRL.

4.5 Conclusion

An analytical model describing non-resonantly pumped CW Raman lasers has been developed in this chapter. Equations defining the Raman laser threshold, slope and conversion efficiencies as functions of measurable resonator parameters were derived. Compared to other Raman laser models developed, the analytical approach was made possible by the non-resonant pump and high-Q Stokes resonator. The validity of the model is limited to systems with negligible thermal lensing.

Good agreement between measured and calculated threshold and slope efficiency was demonstrated for pump powers up to 50 W. A discrepancy in residual pump power was observed and attributed to deterioration of the residual pump beam quality and residual birefringence in the diamond (as discussed in detail in the following chapter).

The model was used to find optimal cavity parameters maximizing Stokes output power at different pump powers. The improved understanding of the laser behaviour on diamond crystal and cavity parameters on Stokes output power provides a convenient design tool for optimizing the design of efficient CW extra-cavity DRLs.

Pages 63-77 of this thesis have been removed as they may contain sensitive/confidential content.

6

Single-frequency pumped diamond Raman laser

Single-longitudinal-mode (SLM) laser operation is a unique regime where the resonator and gain properties are chosen to allow only one longitudinal mode to oscillate within the cavity. The advantage is a highly monochromatic beam that potentially has very low phase and intensity noise (caused by mode coupling) with excellent beam quality. Applications requiring or preferring SLM laser radiation include spectroscopy and atom cooling. While single SLM inversion lasers are common and well understood, there are only a few examples of SLM Raman lasers. SLM output has been demonstrated in resonantly pumped gas Raman lasers [7, 114] and recently in a silicon rib waveguide Raman laser [26]. The extra-cavity DRL provides the opportunity to study the structure of oscillating Stokes modes under SLM pumping in a controlled and few element system.

In this chapter, the DRL is investigated using a SLM fibre laser as a pump source. As well as enabling investigation of the output mode properties when pumping with a SLM laser, the study also demonstrates the applicability of DRLs to a broader family of pump lasers. The output power and efficiency are compared to the multi-longitudinal-mode (MLM) pumping experiments in Chap. 3. The longitudinal mode content of the Stokes beam is characterized as a function of cavity length and input power.

6.1 Raman gain under broad and narrow-band pumping

The effects of pump laser linewidth on the Raman gain have been of great theoretical and experimental interest. In the early development of Raman laser, several aspects captivated the research community including the observed asymmetry in forward and backward scattering, the independence of the forward gain on the pump laser linewidth (in gases) and other peculiarities in the spectral characteristics of the Raman scattering. For the purpose of this thesis, steady-state Raman scattering theory is considered for media with and without dispersion and in a low gain (where the round-trip gain $2gzL \ll 1$) and high gain ($2gzL \gg 1$) limit. The dispersion here refers to different group velocities of the pump and Stokes waves. The second order cross correlation of the pump and Stokes field amplitudes, $\langle E_{\mathrm{P}}^{*}(\tau_1) E_{\mathrm{S}}(0, \tau_2)\rangle$, where $\tau_{1,2}$ are integration times, is assumed to be either 0 (uncorrelated fields) or 1 (fully correlated fields) [115]. It is assumed that only a phase noise is present (no amplitude fluctuations) in the

fields.

The theory of Raman scattering with broad-band pump lasers (also includes narrow pump limit) in the medium without dispersion has been treated by Raymer et al. [116]. Without dispersion, the correlations between the pump and Stokes wave amplitude can freely develop, and hence, in the high-gain limit, the Stokes spectrum always replicates the pump spectrum. The gain is independent on the initial pump or Stokes linewidth and is maximized to the value of g_S (defined by Eq. (2.16)). This conclusion of the dispersionless theory is approximately valid in gases and liquids, where, in the high-gain regime, the Raman gain has been experimentally verified to be independent of the pump linewidth for over nearly five orders of magnitude when using liquid nitrogen as Raman medium [117] and from 0.5 to $0.003\,\mathrm{cm}^{-1}$ [118] when using H_2 gas.

In the low-gain limit and with initially correlated pump and Stokes fields, the fields remain fully correlated (i.e., identical spectra) and the gain is also maximized. However, in the low-gain limit and uncorrelated laser fields, the correlations don't evolve significantly over the cavity lifetime and the fields remain uncorrelated, even though the Stokes spectrum tends to replicate the pump [115]. The effective gain is reduced by the FWHMs of the pump Γ_P and Stokes Γ_S spectra according to

$$G_{\mathrm{eff}} \propto g_S \frac{\Gamma_r}{\Gamma_P + \Gamma_S + \Gamma_r}, \tag{6.1}$$

where Γ_r is the FWHM of the Raman transition.

Discrepancies between experiment and theory in non-gaseous materials, such as crystals, led to the development of statistical methods describing Stokes and pump field correlations in dispersive media. The theory has been developed by Trutna et al. [118], Georges et al. [115, 119] and others. Essentially, dispersion provides a mechanism preventing correlations between interacting fields. Therefore, even for initially correlated pump and Stokes fields, the effective gain is reduced. In the high-gain limit, the Stokes linewidth quickly tends towards zero due to the strong amplification at the centre of the spectrum and the effective gain is reduced by

$$G_{\mathrm{eff}} \propto g_S \frac{\Gamma_r}{\Gamma_P + \Gamma_r}, \tag{6.2}$$

In the low-gain limit the Stokes spectrum is unaffected, thus the gain is reduced by the same factor as for a medium without dispersion (Eq. (6.1)). Therefore the Stokes linewidth must be taken into account when evaluating the Raman gain.

In the opposite limit of narrow pump linewidth compared to the Raman linewidth, the pump linewidth is eliminated from equations in Tab. 6.1, thus the G_{eff} is either reduced by the Stokes linewidth only or the gain is unaffected. All the discussed cases are summarized in Tab. 6.1.

The DRL investigated here operates in the high dispersion regime (due to the diamond) and the low gain limit since the round-trip gain is only a few percent. The pump laser linewidth is $\Gamma_P \ll \Gamma_r$ for fibre laser pumping whereas $\Gamma_P > \Gamma_r$ when pumped with the Nd:YVO_4 laser in Chap. 3. Therefore, the effective Raman gain coefficient is expected to be higher for the SLM fibre laser pump according to Eq. (6.1). Using

Table 6.1: Summary of the Raman gain narrowing factors for an arbitrary pump field [116, 118, 119].

Dispersion	Gain limit	Input Stokes	Effective gain	Stokes output spectrum
No	Low	Uncor.	$G_{eff} \propto g_S \frac{\Gamma_r}{\Gamma_P+\Gamma_S+\Gamma_r}$	Uncor.
No	Low	Cor.	$G_{eff} \propto g_S$	Cor. Identical
No	High	Cor./Uncor.	$G_{eff} \propto g_S$	Cor. Identical
Yes	Low	Cor./Uncor.	$G_{eff} \propto g_S \frac{\Gamma_r}{\Gamma_P+\Gamma_S+\Gamma_r}$	Uncor.
Yes	High	Cor./Uncor.	$G_{eff} \propto g_S \frac{\Gamma_r}{\Gamma_P+\Gamma_r}$	Uncor.

the measured value of 53 GHz for the multi-mode pump laser linewidth and given diamond's 45 GHz linewidth, the gain is predicted to be 3.4 times higher for the SLM pump (here identical Stokes and pump spectra are assumed). Hence, for similar other experimental parameters, the predicted threshold is about 3.3 W compared to the 11 W lasing threshold of DRL pumped by a 30 W multi-mode laser in Chap. 3.

6.2 Raman linewidth broadening

In Raman crystals generally and indeed for diamond, the dispersion for pump and Stokes waves is significant for 1064 nm pumping ($\Delta n = 0.003$ for diamond) thus the Stokes and pump fields remain uncorrelated. Since the Raman transitions are homogeneously broadened [41, 94] and the pump is SLM, a single, or only a few longitudinal modes are expected to oscillate. The reduction in gain from the peak of the Lorentzian distribution for modes spaced by 1.6 GHz (7.5 cm long cavity containing 8 mm long diamond) is, using Eq. (2.15), 99.5%, 98% and 95.6% for the first three mode spacings. Therefore, resonator instabilities and second order effects may be significant in causing of multi-mode output.

Spatial hole-burning [2] is a major cause of multi-mode operation in standing wave homogeneously broadened inversion lasers. The Raman gain, however, is not spatially modulated as shown in Fig. 6.1, since no energy is stored in the Raman medium. The absence of the spatial hole-burning in SLM-pumped Raman lasers is expected to provide a mechanism for assisting in generating stable SLM output.

6.3 Single-frequency pumped diamond Raman laser

The DRL was pumped by a 1064 nm fibre laser system with up to 50 W of power in a diffraction limited beam. The output power and efficiency of the DRL are compared to pumping with the multi-mode laser. The spectral properties of the generated Stokes radiation are studied using a Fabry-Perot interferometer and RF analyzer. The findings are compared to the theory and the implications for future development of SLM DRLs discussed.

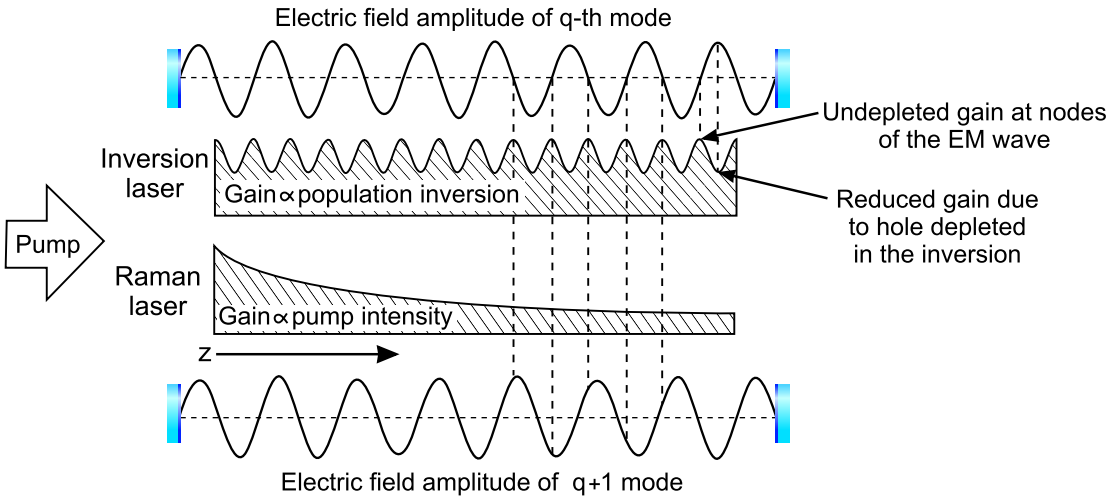

FIGURE 6.1: Comparison of spatial hole-burning in a standing wave inversion laser and gain profile in a Raman laser. The inversion gain is saturated by the standing wave intensity pattern only in the anti-nodes of the EM wave. Therefore a resonator mode with different frequency can be amplified by the unaffected periodic inversion regions.

6.3.1 Pump fibre laser characterization

The pump laser used in the experiment consists of a DFB diode seed laser and Yb fibre amplifier. The 5 mW seed laser (Toptica) had a linewidth of 5 MHz over 5 µs integration time and a mode-hopping free tuning range over 5 nm with wavelength centered at 1064 nm. The output beam was linearly polarised and with a TEM_{00} spatial mode. The seed signal was amplified in a 50 W Ytterbium fibre power amplifier (IPG Photonics). Since the operating wavelength range is 1030–1070 nm the amplifier was able to utilize the full tuning range of the seed laser. The fibre amplifier maintains linear polarisation and diffraction limited TEM_{00} output. The pump power incident upon diamond is shown in Fig. 6.2 as a function of the control unit setting.

The spectral characteristic of the pump laser was measured by a scanning Fabry-Perot (FP) interferometer (Thorlabs). Due to the confocal design of the FP the free-spectral-range is FSR = $c/4L$, which is 10 GHz for the 7.5 mm long cavity. The resonator finesse of 150 results in 67 MHz resolution. Fig. 6.3 shows a FP scan over twice the full FSR and an expanded view of resolvable width of a peak. The FWHM was 75 MHz as expected from the device resolution.

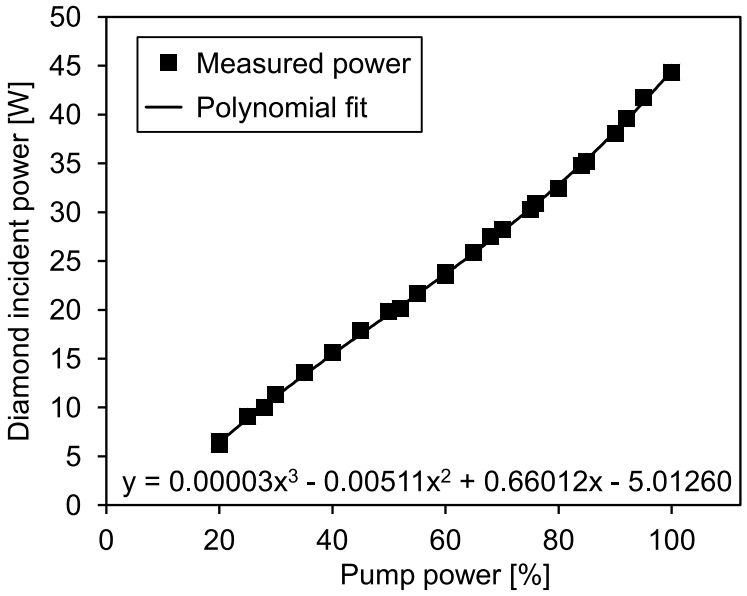

Figure 6.2: Pump power incident on the diamond as a function of relative amplifier amplification. The poly. fit was used to convert the relative setting to output power

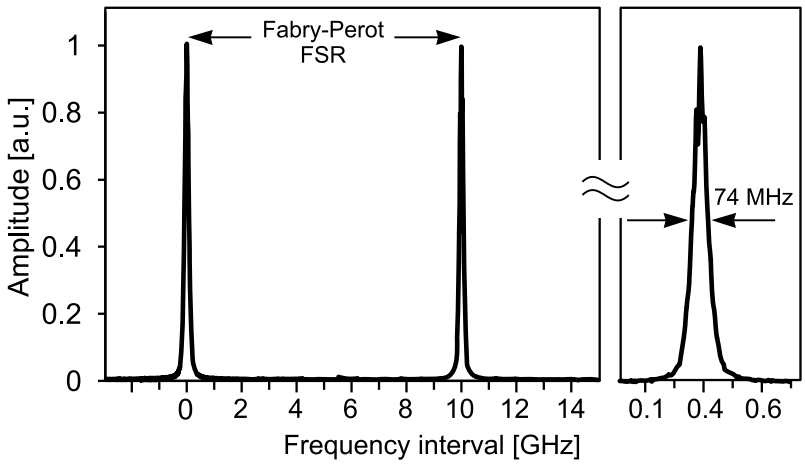

Figure 6.3: Pump laser mode characteristic measured by Fabry-Perot interferometer.

6.3.2 Diamond Raman laser design

The Raman cavity depicted in Fig. 6.4 is similar to the one used in Chap. 3. The input coupler (IC) with radius of curvature 25 mm was highly transmissive (T > 96%) for the pump and second Stokes wavelength and had reflectivity of 99.997% at the first Stokes component. Two 50 mm radius of curvature output couplers were used to investigate single–double-pass pumping. For the double-pass, the output coupler (OC1) was highly reflective for the pump and had a transmission of 0.5% for the Stokes. For the single pass experiments an output coupler (OC2) was used with an identical coating to the input coupler. Therefore the output coupling per round-trip was 0.0055% providing

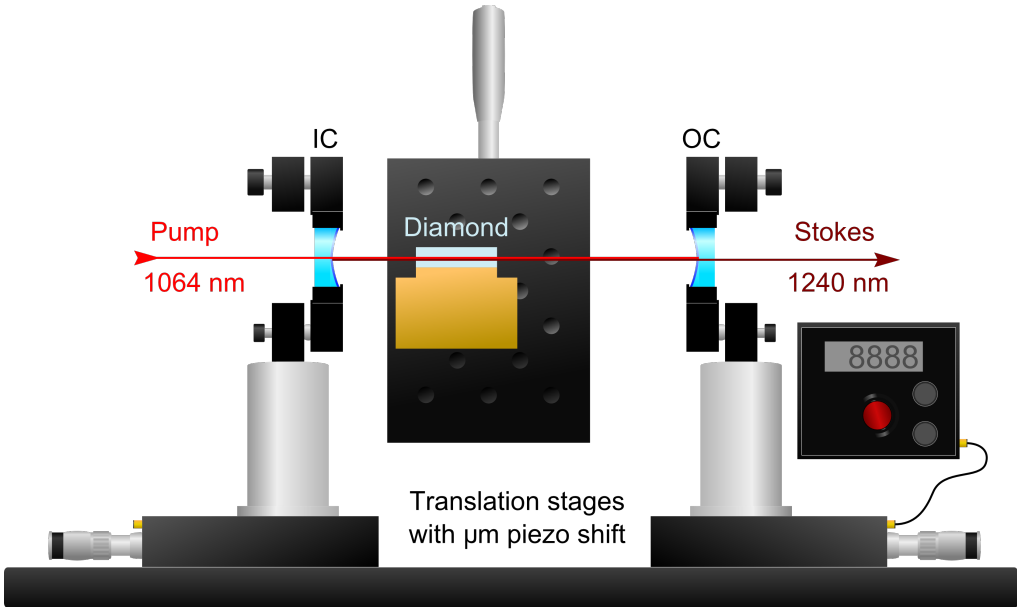

FIGURE 6.4: Stabilized DRL resonator with piezo cavity length tuning.

a finesse of an empty cavity exceeding 5000. The cavity length was 78 mm to ensure good overlap between the 50-mm-lens-focused pump and Stokes field. The diamond used was the 8-mm-long crystal used in experiments of Chaps. 3 and 5. In view of the findings of Chap. 5, the pump beam position in the diamond was optimized to provide low threshold and high slope efficiency output.

6.3.3 Diamond Raman laser power characteristics

The output power and conversion efficiency of the double-pass pumped DRL are shown in Fig. 6.5 as functions of incident pump power. Upon careful alignment the generation threshold is 10 W and the Stokes output power increases with a linear slope of 57.6% over the measured range (see Fig. 6.5). The conversion efficiency attains 44.9% and output power 18 W at maximum incident pump power of 43 W.

The threshold and slope efficiency are similar to that achieved when pumped by the 30 W Nd:YVO_4 laser (see Chap. 3). Hence, the effective gain coefficient is deduced to be similar to the multi-mode pump, despite the smaller pump linewidth Γ_P and improved beam quality. The smaller gain, in contrast to the three-fold increase predicted for the SLM pump, may be attributed to several factors including uncertainties in beam spot-sizes and the birefringence characteristics of the operating point in the crystal.

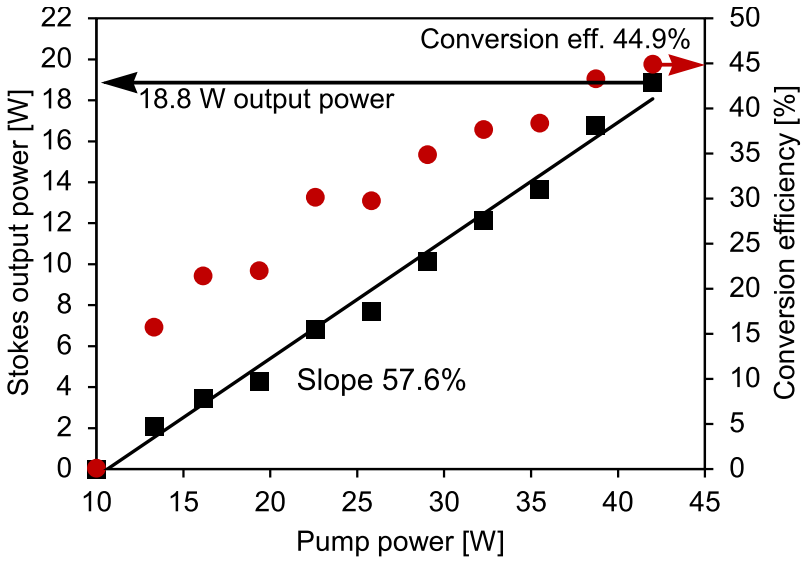

Figure 6.5: Stokes output power and conversion efficiency as a function of incident pump power.

During the measurement of slope efficiency, it was noted that the Stokes output power displayed substantially greater power fluctuations compare to the multi-mode case. To investigate the role of mechanical resonances on output power stability a voltage sine wave was applied to the piezo-driven OC. By changing the applied frequency between 1 Hz and 10 kHz several resonant frequencies shown in Fig. 6.6 were identified in the output for the DRL operating several times above threshold. No resonances were found above 1 kHz.

The measurement indicates that mechanical noise of certain frequencies resonates with opto-mechanical components of the Raman cavity and modulates the Stokes output amplitude. The susceptibility of the SLM-pumped DRL to resonator instabilities was found to be much greater than for multi-mode pumping. In order to make the

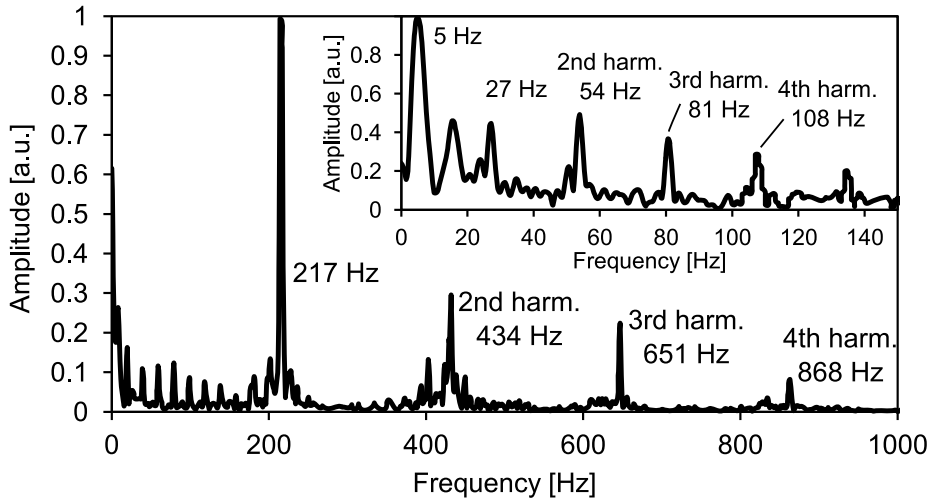

FIGURE 6.6: Identification of resonance frequencies (10-1000 Hz) of introduced mechanical noise.

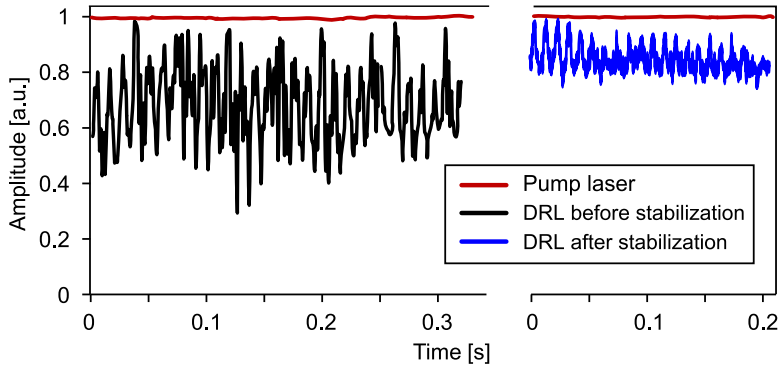

FIGURE 6.7: Comparison of pump (red) and Stokes power noise measured over 0.3 s before (black) and after (blue)mechanical stabilization of the DRL.

Raman cavity more rigid, the diameter of optical posts was increased from $\frac{1}{2}''$ to $1''$ and the setup was placed on a separate breadboard. Comparison of the DRLs amplitude stability in Fig. 6.7 shows significantly reduced noise amplitude in the Stokes output.

When optimizing the cavity parameters small variations in resonator length significantly impact the output power. As illustrated in Fig. 6.8 extension of the resonator length by about 1 µm causes the laser to switch on and off, even when pumped 2-3 times above threshold. Since this period is similar to the Stokes wavelength of 1.24 µm , it appears likely that the transitioning between on and off states is related to scanning of longitudinal modes through the peak of the gain curve. The magnified interval in the Fig. 6.8 shows an example of the abrupt transitions in power that occur within a half-wavelength range.

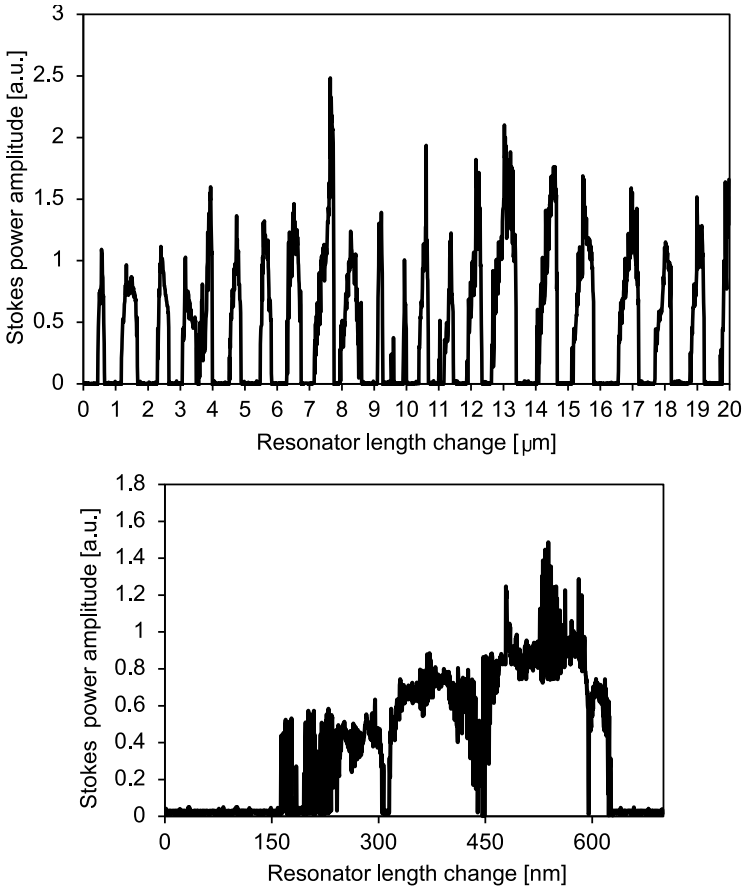

Figure 6.8: Stokes output power as a function of cavity length, for a pump power three times above threshold (30 W).

6.3.4 Diamond Raman laser spectral characteristics

During the course of laser optimization, the coarse spectrum of the Stokes output was measured using a temperature regulated spectrometer (NIR-512 Ocean Optics) with 5 nm resolution. When operating 2-3 times above threshold and for certain cavity length settings, two peaks adjacent to the first Stokes line appear in the spectrum (see Fig. 6.9). The two weak satellites are separated 66 cm^{-1} from the centre of the main Stokes line. Since the two satellites carried enough intensity to generate detectable second Stokes photons they are deduced to be coherently generated alongside the first Stokes. Similar spectral features, with somewhat different spacing (130 cm^{-1}), have been also since observed in an ultra-fast laser pumped DRL [120].

The fact that the appearance and amplitude of the extra frequency components depend on cavity length, and that the spacing varies between two DRL systems, suggests they may result from a phase-matched process such as four wave mixing. Stimulated Brillouin scattering was ruled out as a source since the speed of a sound wave ν_q

corresponding to the 66 cm^{-1} shift $\Delta\omega$, calculated as [41]

$$\nu_{\mathrm{q}} = \frac{\Delta\omega \mathrm{c}}{2\omega_{\mathrm{P}} n \sin(\theta/2)}, \tag{6.3}$$

where ω_{P} is the frequency of the pump laser and θ is the angle between the incident and scattered radiation from the acoustic wave, would be 40×10^4 m/s, an order of magnitude higher than the theoretical value of $\approx 2 \times 10^4$ m/s and thus unphysical. An expected magnitude of the SBS shift in diamond is approx. 6 cm^{-1} [121].

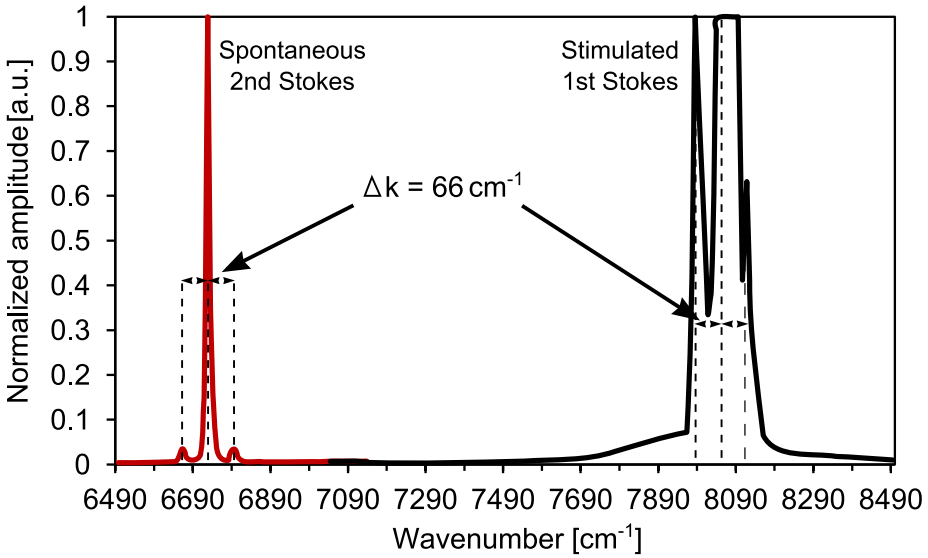

FIGURE 6.9: DRL output spectrum measured three times above threshold. Two satellite peaks, spaced by 66 cm^{-1} from the first Stokes, were observed under some cavity length settings.

Double-pass pumping

The longitudinal-mode content of the oscillating Stokes field was characterized by using of the 10 GHz FP interferometer. Note that since the FSR of the 78 mm DRL cavity, 1.68 GHz, is very close to six times the 10 GHz FSR of the FP interferometer, the modes spanning outside the FP FSR fold back on the same measured time interval with a small shift (see Fig. 6.10). Thus it was difficult to determine unambiguously the number of longitudinal-modes when more than six were present in the Stokes output spectrum.

When double pass pumping is used, and the Raman laser operates at maximum output power to eliminate threshold instabilities, several modes of operation were distinguishable. Under some conditions, SLM operation (as in Fig. 6.11 A), was induced by making small adjustments (within 1 μm) in the cavity length. However, the mode position is stable only for a few FP scans i.e., for a period of approximately 100 ms. The output power displayed random amplitude fluctuations, deduced from the absence of major peaks in the corresponding measured Fourier transform (FT) spectrum.

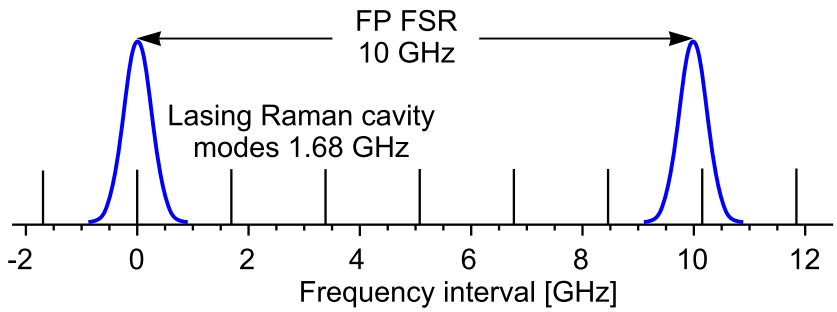

Figure 6.10: A schematic showing an FP interferometer scan with 10 GHz FSR. Since the transmission of the FP interferometer is a periodic function, modes may superimposed if the mode spacing is exactly or close to an integer fraction of the FP FSR.

Upon a change in the resonator length (within 1 µm) several weaker modes start to oscillate alongside the main mode (Fig. 6.11 B). The longitudinal mode spacing of 1.68 GHz corresponds to the FSR of the Raman resonator. The number of modes and their amplitudes were observed to fluctuate over the period of several FP scans.

Figure 6.11 C shows a further operation mode obtained by again adjusting the resonator length. The amplitude and quantity of the longitudinal modes increased. In the shown example at least six modes were oscillating within the FSR of the FP interferometer. The output power is more stable compared to the previous cases.

The last example Fig. 6.11 D shows highly multi-mode Stokes output. All modes oscillating contain similar power with some minor changes during consecutive measurements. The output power is stable with only some higher frequency noise and no major stable components in the Fourier domain.

Single-pass pumping

In order to understand the mechanism causing multi-mode Stokes oscillations under SLM pumping, the resonator setup was changed to enable single-pass pumping (OC2). The absence of the back reflected pump wave prevented possible interferences on the pump beam potentially influencing the Raman laser performance. The DRL threshold was 5 W of pump power. The output power, when operating three to five times above threshold, was tens of milliwatts. The longitudinal mode spacing of approx. 1.6 GHz did not change compared to the double-pass pumping as expected.

The Stokes power behaviour and mode content is shown in Fig. 6.12 A–D. For pump powers three (A–C) to five (D) times above threshold, the measured power was much more stable (over the measure time interval of 100 ms) compared to the double-pass pumping, and remained stable even for changes in cavity length. However, the mode structure was found to change markedly as a function of cavity length. In A, every second cavity mode is missing and the amplitude of the modes is uneven. Since a formation of intracavity etalons can cause a periodic modulation of resonator loss, the diamond was tilted in order to prevent multiple reflections of the diamond faces to resonate. After ensuring that no etalons could be formed in the cavity, similar alternating mode behaviour was observed for certain cavity length adjustments (see

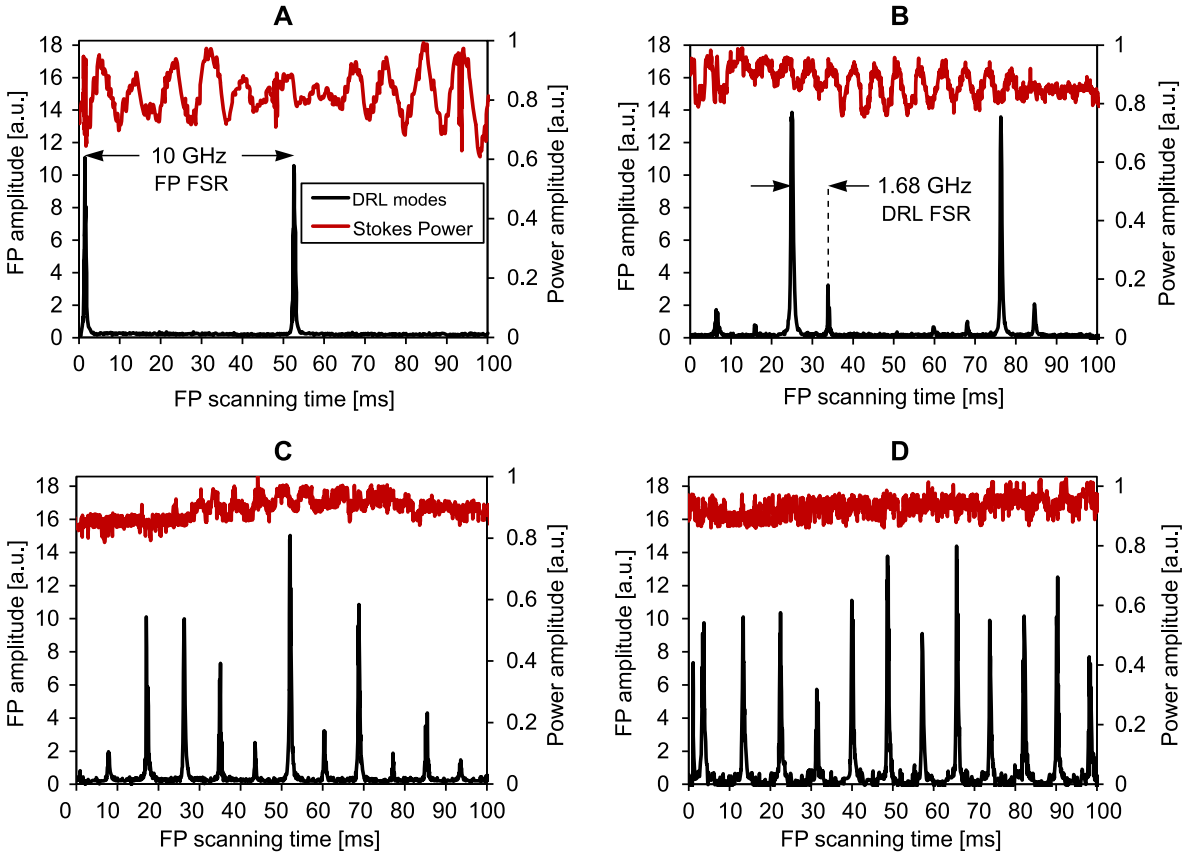

FIGURE 6.11: Output power and longitudinal mode content of the DRL under double-pass pumping. The operating conditions corresponding to each panel (A, B, C, D) are described in the text.

Fig. 6.12 B).

Further alterations of the resonator length caused the power to evenly distribute in the oscillating modes, as shown in C. All modes contained similar power and their amplitudes remained stable for over several hundreds of milliseconds. Without changing the cavity length the pump power was increased to five times above threshold. The modes amplitudes remained stable over a similar time interval as in previous case (Fig. 6.12 D). However, the broadening of mode peaks shown in the Fig. 6.12 D indicate that the number of modes increased well outside the FSR of the FP interferometer. When the pump power was than gradually decreased, the number of oscillating modes decreased; however, at least six modes are present even at the lasing threshold.

The individual modes are more "fuzzy" compared to the double pass pumping results indicating larger mode jitter within the FP integration period or rapid "on-off switching" of the modes. The reason may be the greatly increased photon cavity lifetime of 198 ns which corresponds to 380 round-trips. To determine whether the modes are oscillating simultaneously (as opposed to mode-hopping) a RF analyzer (Agilent N9030A 3 Hz to 50 GHz) was used to measure the beat frequency of the oscillating modes. The measured spectrum in Fig. 6.13 shows a strong beating signal

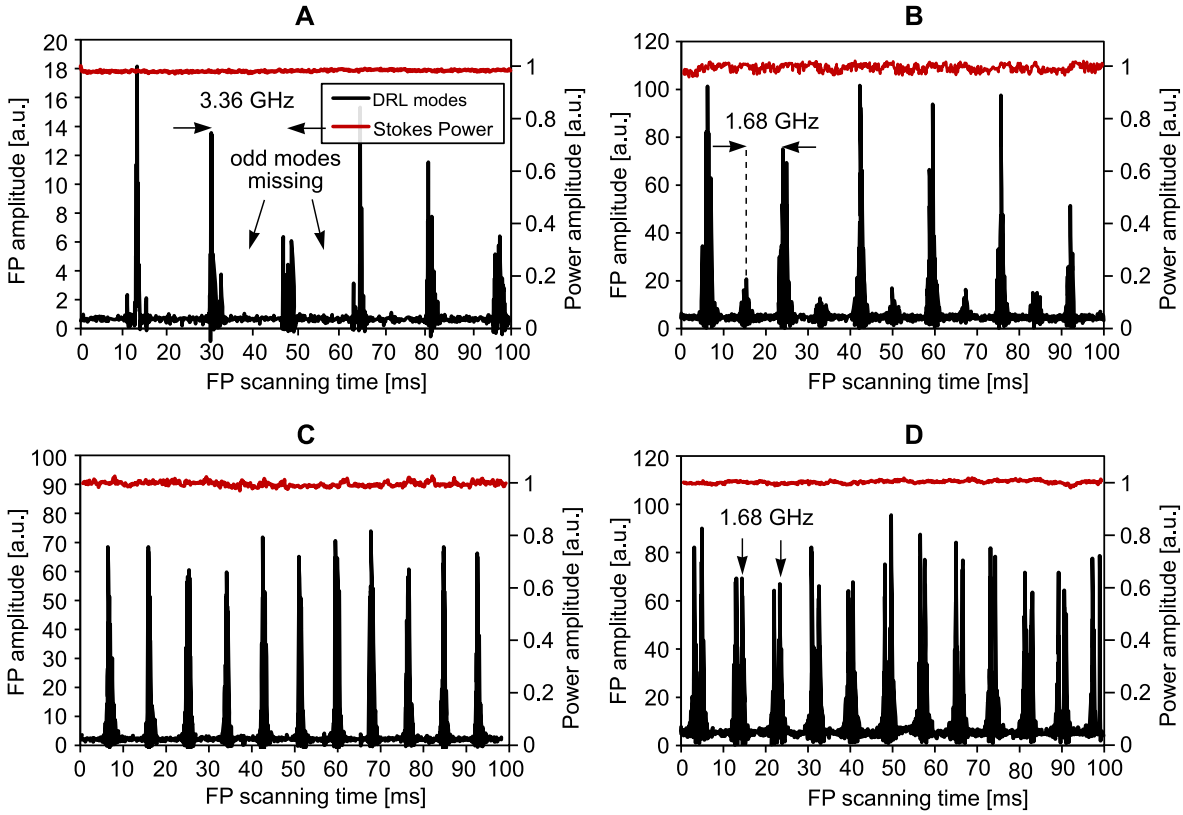

Figure 6.12: Output power and longitudinal mode content under single-pass pumping. In B–D, the diamond was tilted to reduce the possibility of etalon effects. In A–C the DRL operates three times, in D five times, above threshold.

at 1.684 GHz corresponding to the FSR of 77.8 mm long resonator containing a 8 mm long diamond. The presence of the resonance suggests that some of the longitudinal modes are oscillating simultaneously within the Raman cavity. The other smaller resonances, which are separated too far from the cavity resonance, are attributed to cavity instabilities changing the exact frequency of oscillating modes.

6.4 Discussion

Although the SLM-pumped DRL performed well in terms of slope efficiency and output power, there were several aspects of its performance that were unexpected in the light of the theory summarized earlier in the Chapter. The predicted reduction in threshold for the narrower linewidth pump was not observed. Due to the inherent uncertainties in operating parameters this result may not be significant, however. Perhaps the most significant departure in performance from theory is the highly multi-moded output, which in the case of double-pass pumping is accompanied by poor output power stability. This unstable frequency behaviour appeared to be a characteristic feature of the SLM-pumped DRL. SLM output was observed, but this could only be temporarily

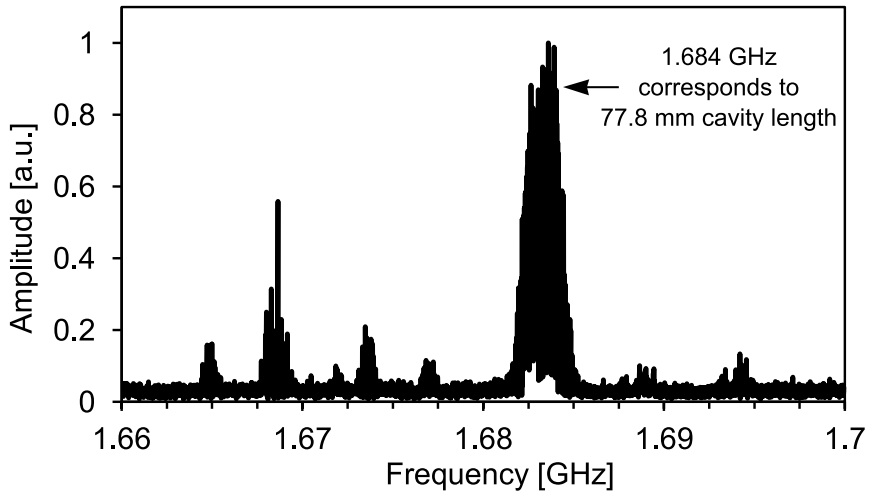

FIGURE 6.13: RF spectrum of laser output showing a beating frequency of the multi-mode Stokes output.

achieved (for periods less than 100 ms) using double-pass pumping and it was accompanied by large fluctuations (>10%) in output power on a millisecond time-scale.

The results are compared with the few other instances of SLM-pumped Raman lasers in the literature. The resonantly pumped gas systems of refs. [27, 27] utilized SLM pumping and the relatively narrow Raman linewidth of gases to achieve SLM output. In the case of H_2, the FWHM gain linewidth of 510 MHz is much smaller than the cavity mode spacing of the 7.28 cm cavity [27]. As a result, cavity locking required at least one cavity mode to coincide with the centre of the gain distribution. Under these conditions only one longitudinal mode can oscillate in the resonator. SLM Stokes output has also been reported in a Si Raman laser. Using a rib waveguide, both single-mode [26] and multi-mode [39] Raman outputs have been observed. Here the longitudinal mode spacing of the waveguide (0.9 GHz) was much smaller than silicon Raman linewidth of 37.2 GHz [41] allowing several modes to oscillate within the waveguide resonator. However, the techniques and conditions for which SLM output was obtained were not discussed in detail. Comparison of these systems with the DRL is shown schematically in Fig. 6.14. In contrast to the H_2 Raman laser the SLM-pumped DRL is not frequency locked to the pump and the diamond Raman linewidth (45 GHz [41]) is broader than the cavity FSR. In that respect the DRL is similar to the Si Raman laser. However, the lack of details regarding the Si laser stability and operating conditions prevents more detailed comparison.

As discussed above, the Raman gain is homogeneous, thus strong mode competition is expected. Even if there was significant inhomogeneous broadening (due to defects, isotopic and extrinsic impurities, etc) the fact that multiple modes are observed within the homogeneous width, even near threshold, is unexpected. The observed multi-mode behaviour suggests there is a mechanism, not yet understood, which causes inherent instability in SLM operation.

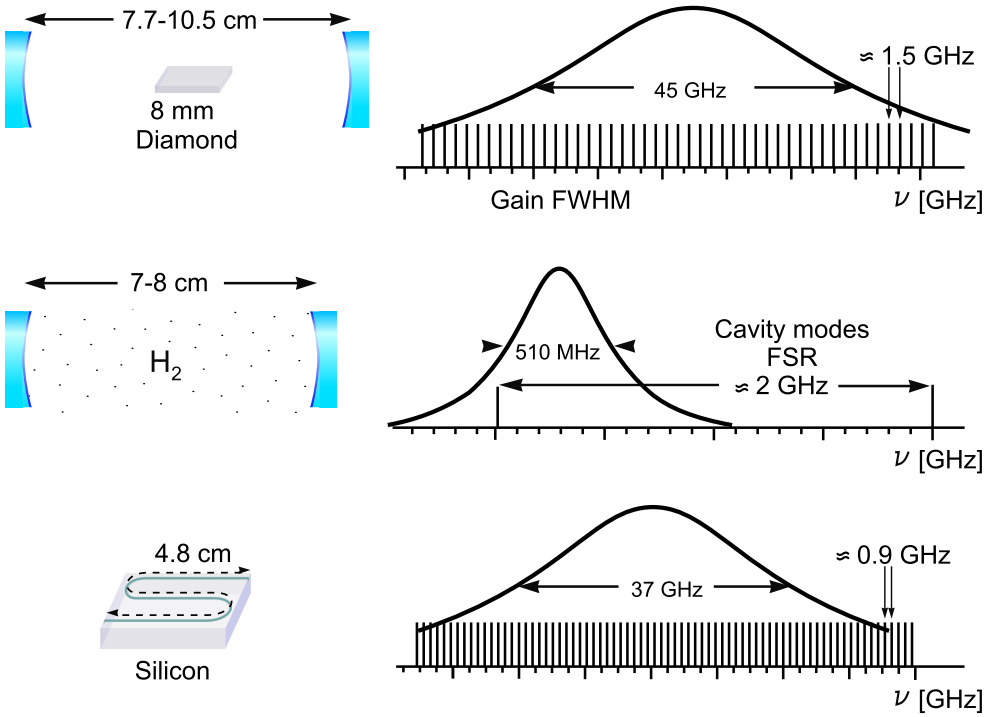

Figure 6.14: Comparison of resonantly pumped H_2 Raman laser, DRL and Silicon waveguide laser cavity and FWHM of the gain distribution.

It is widely known that when more than one frequency is present in the pump spectrum, four-wave mixing processes may give rise to additional components in the Raman polarisation leading to additional frequencies and broadening of Stokes output [122]. In the presented DRL the pump is strictly single mode; however, more than a single Stokes mode may be generated due to cavity length instabilities, stress birefringence or other subtle effects, due to a small gain difference of neighbouring modes (0.5% for the first neighbouring mode) close to the peak of the Lorentzian distribution. Such perturbations combined with four-wave mixing of multi-mode Stokes field may thus provide a mechanism for broadening the Stokes spectrum across a large fraction of the diamond Raman linewidth.

The DRL was observed to generate more stable multi-mode output for the case of a single-passed pump through the diamond. It is not yet clear, however, whether this is a result of greatly increased resonator finesse (and thus Stokes photon cavity lifetime) or due to the absence of the interferences on the pump wave.

6.5 Conclusion

In this chapter high power external cavity DRL pumped by a SLM fibre laser has been investigated. The 10 W threshold and 19 W of output power are comparable to multi-mode pumped DRL suggesting no significant change in the Raman gain. The shift from solid-state pumping to a Yb fibre system without loss in efficiency demonstrates the adaptability of extra-cavity DRL to pump sources other than bulk crystal lasers.

Indeed, as far as the author is aware, this work represents the first efficient and first CW conversion of a fibre laser in a Raman crystal.

The SLM pumping does not generally result in a stable SLM Stokes output. The number of oscillating longitudinal modes and their amplitudes stability varies for small changes in the cavity length. The mechanism leading to the multi-mode Stokes spectrum is more pronounced when using a high-Q cavity and single- rather then double-pass pumping, where several modes start to oscillate even slightly above threshold.

The origin of the multi-mode Raman generation in the case of the homogeneously broadened Raman gain in diamond under SLM pumping has been discussed. The understanding of the physics describing multi-mode Stokes generation from SLM pumping is immature, thus future work is needed to understand the mechanisms for spectrum broadening and to determine conditions enabling SLM operation. A number of approaches are envisioned. Shortening of the resonator so that its FSR is greater than half of the Raman linewidth FWHM assures single mode output. The resonator formed by diamond would have to be less than about 3 mm long in this case. Introducing mode-selecting intracavity elements (etalons, birefringent filters) may also provide an effective method for restricting the number of oscillating modes. At the same time, however, it increases cavity loss and thus reduces the lasers efficiency as established in previous chapters. Injection seeding of the cavity may also assist in a single-mode Stokes generation at the cost of additional system complexity.

7 Conclusion

Synthesis of single-crystal diamond has reached the point where samples with high optical quality are readily available. Diamond has progressed from cutting tools and heat-spreaders to applications in optics and lasers. As a Raman gain material, diamond exploits its excellent opto-mechanical and thermal properties and large scattering cross section and this has resulted in the rapid progress in crystal Raman laser technology, in the last few years. The main directions of development have been as extra-cavity pulsed and intra-cavity CW DRLs.

This thesis demonstrates a novel approach to achieving highly-efficient, high-power Raman conversion: extra-cavity CW diamond Raman lasers. The results show that the combination of an external oscillator and diamond as a Raman medium, enables efficient CW Stokes generation and is suitable for power-scaling to the hundreds of watts level.

7.1 Summary

The foundation work of this project was a demonstration of a 10 W CW DRL using a 30 W pump laser. This first encouraging result already exceeded the output power of most CW Raman lasers, and was two orders of magnitude more powerful than the previous best extra-cavity CW Raman laser. Due to the promise for further increases in output power, a second QCW pump laser with on-time power of 50 W was constructed to investigate the DRLs performance. The higher pump power enabled DRL output power, in steady-state, to be increased to 22 W. No power roll-off was observed confirming that diamonds power handling capability is vastly superior to other materials. A power budget of the Raman process was evaluated in Chap. 3.5. It revealed that the diamond bulk loss significantly limited the efficiency of the laser.

A calculation of thermal lensing and resonator stability showed that efficient operation is predicted when using higher pump powers. Output powers of up to approximately 100 W are anticipated before thermo-optic effects become significant in the resonator designed in Chap. 3.5.1. Scaling to much higher powers is predicted by increasing output coupling and beam waist sizes in the diamond.

In Chap. 4 an analytical model for the DRL was derived to identify which parameters are crucial to optimization. The modelling showed that the initially estimated parameters of the Raman resonator were close to optimal at current pumping levels, and only minor increase in efficiency could be gained by further optimizing the output-coupling. The model was used to predict acceptable tolerances on crystal length,

parasitic loss and output coupling, and their dependencies on pump power. In the presented DRLs, stronger focusing of the pump would decrease the threshold but not the maximal output power for fixed pump power and output-coupling of 0.5%. The length of 8 mm of the diamond was optimal for the current level of parasitic losses.

Throughout the experiments performed in this project it became obvious that DRL performance significantly varied as a function of beam location in the diamond. Even within one crystal a change of pump spot position led to unpredictable variations in output power and orientation of the Stokes polarisation. It was suspected that residual birefringence may have such an impact, as it is well known that during the CVD growth of single crystal diamond significant stress-induced birefringence can develop. Therefore, in Chap. 5 the polarisation properties of the Stokes beam were characterized as functions of pump beam polarisation and beam position in the diamond. A thorough comparison of the measured threshold and polarisation orientations with the calculated tensor nature of the Raman scattering efficiency showed that threshold was inversely proportional to the scattering efficiency for Stokes polarisations parallel to the birefringence axes. The pump polarisation orientation determined whether the Stokes polarisation was parallel to the fast or slow birefringence axis.

In order to study longitudinal-mode dynamics in these systems, a DRL was investigated that employed a single-frequency pump laser (Chap. 6). As far as the author is aware, this is the first time that mode dynamics for single frequency pumping have been investigated in detail for any crystalline Raman laser. Contrary to expectations, stable SLM output was not obtained. Laser output was found to exhibit many modes of behaviour involving large changes in amplitude stability and mode content. Under some conditions, sideband frequencies were observed adjacent to the Stokes peak in the spectrum that, although not yet explained fully, may be attributable to a non-Raman four-wave mixing process.

The extra-cavity conversion approach enabled by diamond has the potential to be applied to many different CW pump laser technologies with high spectral density and high brightness. To demonstrate this flexibility a CW 50 W Yb fibre laser was used to pump the DRL cavity. The measured output power characteristics were similar to the bulk solid-state laser pumping with almost 20 W of output power and 50% conversion efficiency. The external cavity diamond laser concept thus enables efficient frequency conversion to be applied to a greater range of pump lasers than for other Raman crystals materials, where the latter are generally restricted to lower powers and laser media compatible with intracavity designs.

7.2 Implications and future work

The results of this thesis directly impact on the design and operation of future DRL technology. Many of the outcomes indicate interesting directions for further study.

7.2.1 High-Q diamond Raman lasers

Since the output-coupling used throughout the thesis was only 0.5%, the findings apply directly to low-threshold high-Q diamond lasers. Although the DRL efficiency can be optimized by changing resonator properties according to the modelling in Chap. 4, diamond impurities and lattice defects were found to strongly influence performance of the DRL.

The residual absorption, caused by nitrogen and lattice defects in the synthetic diamond, is presently the major cause limiting the conversion efficiency. Future synthesis of lower loss material will enable slope and conversion efficiencies to increase accordingly towards the quantum limit, which in the case of 1064 nm pumping is 86%.

Lower birefringence material will enable efficient lasers to be designed more simply. These problems should also be considered for devices that simultaneously oscillate on the Stokes and pump fields within the diamond resonator. Many intracavity DRLs to date that have been investigated with 1-2% output-coupling (Parrotta et al. [73, 123], Lubeigt et al. [57, 64], Savitski et al. [74, 91], and Kemp et al. [95]) will similarly benefit from improved diamond. In the case of birefringence, depolarization loss of the fundamental field as well as the Stokes is a further consideration for the intracavity design. Future development of resonantly-pumped DRLs, which rely on resonant enhancement of the pump field within a DRL cavity, will likewise benefit from improved diamond quality.

When birefringence is significant, the results of Chap. 5 provide guidance on DRL optimization. Once the magnitude of the birefringence and its orientation in the diamond sample has been characterized, a path through the diamond with a birefringence axis parallel to one of the $\langle 111 \rangle$ directions is found to be preferred. Orienting the pump parallel to this axis results in lasing without a gain reduction. In the case of no other depolarization effects (such as circular dichroism), the birefringence will have no impact and the Stokes polarisation direction will be parallel to the pump in accordance with the Raman tensor. If such a spot does not exist in the sample, a place with the lowest birefringence is recommended. In designs that require the pump and Stokes fields polarisations to be parallel (e.g., cavities involving other polarizing elements), diamond orientated so that the local birefringence axis coincides with the pump polarization direction is expected to minimize losses on pump and Stokes fields.

7.2.2 Low-Q high power diamond Raman laser

Modelling presented in this thesis has shown that residual absorption and birefringence in diamond are less critical as pump focusing and power are increased. The optimal output-coupling increases, which reduces the relative impact of parasitic losses. Other parameters, such as crystal length, become important factors for optimization.

As the availability of narrow-linewidth, high-brightness, kilowatt class CW lasers is limited, quasi CW (QCW) pumping provides a convenient method for studying Raman conversion at elevated power levels. Since the thermal gradients in a diamond establish within 50 µs, pulses with more than 100 µs duration are sufficient for investigation of the steady-state DRL performance. For example, a QCW laser with 1% duty-cycle and 10 W average power will enable experimental investigation into the power limitations of DRLs under kilowatt pumping.

7.2.3 New wavelengths generation

In all of the experiments presented in this thesis, the DRL was pumped by 1064-nm emitting lasers. Although the 1240 nm Stokes output wavelength is of some interest in applications, the extra-cavity concept can be readily adapted to other parts of the spectrum.

The high power CW Raman output can be extended further into the infrared and into the applications-rich "eye-safe" region by cascading the scattering into higher Stokes orders. The second and third Stokes components when pumped at 1064 nm are 1485 nm and 1851 nm. Pumping with the secondary-line of Nd lasers at 1.3 µm, will enable generation of 1.6 µm and 2 µm. However, the Raman gain coefficient is reduced at longer wavelengths and the generation between 2.5 and 6.5 µm becomes more difficult due to multi-phonon excitation. Pump lasers based on different active laser ions (Yb, Tm, Er, etc.) further extend the potential wavelength coverage of DRLs.

Tunable high power CW lasers are a technology of great interest for DRL pumping. Specifically, the advances in Yb fibre lasers are highly encouraging. If a fibre laser, tunable from 976 to 1120 nm [124], were combined with the extra-cavity DRL presented, the wavelength coverage of the whole system would span from 976 to 1316 nm. By changing the output coupler to resonate the second or third Stokes component the laser would reach up to 2 µm. Similar advantages are also offered by VECSEL laser technology with even broader potential wavelength choice.

The DRL output can be extended into the visible by pumping with the harmonics of the pump sources. For example, the first three Stokes components of a green pump are situated in the yellow, orange and red spectral regions. Pumping DRLs at shorter wavelengths have the benefit that the gain is much higher, although it may be important to consider increased scatter and absorption coefficients. The wide band gap of diamond may be utilized to extend CW conversion in the ultraviolet. The Raman gain is approximately 100 cm/GW, thus thresholds are potentially an order of magnitude lower. It should be noted, however, that deep-UV operation is currently problematic, due to a characteristic UV-induced surface damage mechanism observed in the UV-C [68, 125].

A more efficient option for generating DRL output at shorter wavelengths is by intracavity harmonic conversion, a scheme that has been widely used in intracavity Raman lasers [12, 123, 126]. In this case, the Stokes field is strongly resonated and the second order-nonlinear conversion provides a means of output-coupling. Cavity designs for intracavity doubled DRLs may include folded and ring resonator schemes and are

a subject of further investigation.

7.2.4 Single-frequency sources

There are many applications in spectroscopy, atmospheric ranging and detection, and atom cooling that require CW high power and narrow linewidth laser radiation at specific wavelengths. The results presented in Chap. 6 show that the path to single frequency Stokes generation is not as straightforward as previously thought. A future theoretical study supported by experiments is required to further describe the single-frequency pump and multi-mode Stokes interaction.

Demonstration of single-frequency output may require incorporation of line-selective cavity elements such as etalons to provide the necessary additional mode discrimination. However, the increased loss would likely elevate the lasing threshold. Seeding of the DRL with a single-mode Stokes signal may also provide a viable strategy for inducing SLM operation.

7.2.5 Closing words

The extra-cavity DRLs studied throughout this thesis have proved to be an excellent test-bed for investigating the performance and limitations of CW beam conversion in diamond. The work presented in this thesis opens up new intriguing research areas and highlights the promise for diamond laser technologies in the future.

A
Related Publications

This appendix includes the following published journal articles that I have authored/co-authored and are relevant to this thesis:

1. O. Kitzler, A. McKay, and R. P. Mildren, "Continuous-wave wavelength conversion for high-power applications using an external cavity diamond Raman laser," Optics Letters **37**, 2790–2792 (2012).

2. A. McKay, O. Kitzler, and R. P. Mildren, "Simultaneous-brightness enhancement and wavelength conversion to the eye-safe region in a high-power diamond Raman laser," Laser & Photonics Reviews, early posting, DOI: 10.1002/lpor.20140012, (2014).

3. A. McKay, H. Liu, O. Kitzler, and R. P. Mildren, "An efficient 14.5 W diamond Raman laser at high pulse repetition rate with first (1240 nm) and second (1485 nm) Stokes output," Laser Physics Letters **10**, 105801 (2013).

4. A. McKay, O. Kitzler, and R. P. Mildren, "High power tungstate-crystal Raman laser operating in the strong thermal lensing regime," Optics Express **22**, 707–715 (2014).

5. A. McKay, O. Kitzler, and R. P. Mildren, "Thermal lens evolution and compensation in a high power KGW Raman laser," Optics Express **22**, 6707–6718 (2014).

Pages 102-136 of this thesis have been removed as they contain published material. Please refer to the previous page for citation details of the articles contained in these pages.

B
List of Publications

This appendix includes the following list of all publications and conference presentations that I have authored/co-authored during this PhD project:

Book chapter

1. R. P. Mildren and J. R. Rabeau, *Optical Engineering of Diamond* (Wiley-VCH Verlag GmbH & Co. KGaA, 2013), Chap. 8, R.P. Mildren, A. Sabella, O. Kitzler, D. Spence, and A. McKay, "Diamond Raman laser design and performance."

Patent

1. R. P. Mildren and O. Kitzler, "A device and a method for converting a light and a laser system," patent No. WO2013155568 A1 (2013).

Peer-reviewed journal articles

1. O. Kitzler, A. McKay, R. J. Williams, and R. P. Mildren, "Modeling and optimization of extra-cavity diamond Raman lasers," in preparation.

2. O. Kitzler, V. M. Hadiya, A. McKay, R. J. Williams, and R. P. Mildren, "Polarization control in high-Q diamond lasers," in preparation.

3. R. J. Williams, O. Kitzler, A. McKay, and R. P. Mildren, "Investigating diamond Raman lasers at 100 W-level quasi-cw pumping," in preparation.

4. A. McKay, O. Kitzler, and R. P. Mildren, "High power tungstate-crystal Raman laser operating in the strong thermal lensing regime," Optics Express **22**, 707–715 (2014).

5. A. McKay, O. Kitzler, and R. P. Mildren, "Simultaneous brightness enhancement and wavelength conversion to the eye-safe region in a high-power diamond Raman laser," Photon. Rev., L1–L5 (2014).

6. A. McKay, O. Kitzler, and R. P. Mildren, "Thermal lens evolution and compensation in a high power KGW Raman laser," Optics Express **22**, 6707–6718 (2014).

7. O. Kitzler, A. McKay, and R. P. Mildren, "Continuous-wave wavelength conversion for high-power applications using an external cavity diamond Raman laser," Optics Letters **37**, 2790–2792 (2012).

8. M. Jelinek, O. Kitzler, H. Jelinkova, J. Sulc, and M. Nemec, "CVD-diamond external cavity nanosecond Raman laser operating at 1.63 μm pumped by 1.34 μm Nd:YAP laser," Laser Phys. Lett. **9**, 35–38 (2012).

Conference presentations

1. A. McKay, O. Kitzler, and R. P. Mildren, "An analysis of thermal effects in high power (8 W) KGW Raman lasers," at SPIE LASE, San Francisco, United States, paper No. **8964-36** (2014). *Oral presentation.*

2. R. J. Williams, O. Kitzler, A. McKay, and R. P. Mildren, "Power scaling of diamond Raman lasers beyond 100 W using quasi-cw pumping," at SPIE LASE, San Francisco, United States, paper No. **8964-17** (2014). *Oral presentation.*

3. O. Kitzler, A. McKay, R. J. Williams, V. M. Hadiya, and R. P. Mildren, "Fiber laser pumped continuous-wave external cavity diamond Raman laser," at ANZCOP, Fremantle, Western Australia (2013). *Oral presentation.*

4. O. Kitzler, A. McKay, V. M. Hadiya, and R. P. Mildren, "Characterisation and optimization of external cavity continuous-wave diamond Raman laser," at FiO, Orlando, Florida, United States, No. **LTh2H.1** (2013). *Oral presentation.*

5. O. Kitzler, A. McKay, and R. P. Mildren, "Characterization of a single-frequency-pumped continuous-wave extracavity diamond Raman laser," at CLEO Europe, Munich, Germany, No. **CD-P37** (2013). *Poster presentation.*

6. O. Kitzler, H. Jelinkova, J. Sulc and L. Koubikova, M. Nemec, K. Nejezchleb, and V. Skoda, "High energy intracavity pumped eye-safe $BaWO_4$ Raman laser," at SPIE Photonics West, San Francisco, California, United States, No. **85991W** (2013). *Poster presentation.*

7. A. McKay, O. Kitzler, A. J. Lee, and R. P. Mildren, "Strong astigmatic lensing in high-power (>7 W) tungstate external-cavity Raman lasers," at ANZCOP, Fremantle, Western Australia (2013). *Poster presentation.*

8. R. J. Williams, O. Kitzler, A. McKay, and R. P. Mildren, "Quasi-CW-pumping of diamond Raman lasers," at ANZCOP, Fremantle, Western Australia (2013). *Poster presentation.*

9. R. J. Williams, O. Kitzler, A. McKay, and R. P. Mildren, "Planar diamond waveguide Raman laser operating at 573 nm and 620 nm," at ANZCOP, Fremantle, Western Australia (2013). *Post deadline oral presentation.*

10. A. McKay, O. Kitzler, and R. P. Mildren, "Power scaling of efficient diamond Raman lasers with 1240 nm and 1485 nm output," at CLEO Europe, Munich, Germany, No. **CA-1.4** (2013). *Poster presentation.*

11. O. Kitzler, A. McKay, and R. P. Mildren, "High power cw diamond Raman laser: Analysis of efficiency and parasitic loss," at CLEO: Science and Innovations, San Jose, California, United States, No. **CTh1B** (2012). *Oral presentation.*

12. A. McKay, O. Kitzler, H. Liu, D. Fell, and R. P. Mildren, "High average power (11 W) eye-safe diamond Raman laser," at SPIE Photonics West, San Francisco, California, United States, No. **85510U** (2012). *Poster presentation.*

13. O. Kitzler, A. McKay, and R. P. Mildren, "CW diamond laser architecture for high average power Raman beam conversion," at CLEO PacRim, Sydney, NSW, Australia (2011). *Post deadline oral presentation.*

14. O. Kitzler, A. Sabella, B. Johnston, A. McKay, and R. P. Mildren, "Design and characterisation of optical quality single crystal diamond for Raman laser applications," at CLEO PacRim, Sydney, NSW, Australia (2011). *Poster presentation.*

15. O. Kitzler, A. Sabella, A. McKay, and R. P. Mildren, "Characterization of optical quality single crystal diamond for Raman laser applications," at IMRC XX, Cancun, Mexico, No. **S17-P05** (2011). *Poster presentation.*

Symposia

1. O. Kitzler, A. McKay, and R. P. Mildren, "High average power diamond Raman beam conversion," at MMI-Harvard Diamond Photonics Symposium (2012). *Poster presentation.*

References

[1] A. A. Kaminskii, *Laser Crystals: their physics and properties* (Springer, 1990). 1, 31

[2] W. Koechner, *Solid-State Laser Engineering* (Springer, 2006). 1, 31, 33, 39, 40, 42, 72, 81

[3] I. T. Sorokina and K. L. Vodopyanov, *Solid-State Mid-Infrared Laser Sources* (Springer, 2003). 2, 4

[4] I. Breunig, D. Haertle, and K. Buse, "Continuous-wave optical parametric oscillators: recent developments and prospects," Applied Physics B **105**, 99–111 (2011).

[5] Lockheed Martin, http://www.lockheedmartin.com/us/products/aculight/argos.html. Accessed: 2014-03-31. 2

[6] A. Penzkofer, A. Laubereau, and W. Kaiser, "High intensity raman interactions," Progress in Quantum Electronics **6**, 55–140 (1979). 2, 11, 14

[7] J. K. Brasseur, P. A. Roos, K. S. Repasky, and J. L. Carlsten, "Characterization of a continuous-wave Raman laser in H_2," JOSA B **16**, 1305–1312 (1999). 2, 4, 5, 56, 79

[8] Y. Feng, L. R. Taylor, and D. B. Calia, "150 W highly-efficient Raman fiber laser," Optics Express **17**, 23678–23683 (2009). 2, 4

[9] H. M. Pask, "Continuous-wave, all-solid-state, intracavity Raman laser," Optics Letters **30**, 2454–2456 (2005). 2, 3

[10] J. A. Piper and H. M. Pask, "Crystalline Raman Lasers," Journal of Selected Topics in Quantum Electronics **13**, 692–704 (2007). 2, 3, 5, 39

[11] A. A. Demidovich, A. S. Grabtchikov, V. A. Lisinetskii, V. N. Burakevich, V. A. Orlovich, and W. Kiefer, "Continuous-wave Raman generation in a diode-pumped Nd^{3+}:$KGd(WO_4)_2$ laser," Optics Letters **30**, 1701–1703 (2005). 2

[12] A. J. Lee, D. J. Spence, J. A. Piper, and H. M. Pask, "A wavelength-versatile, continuous-wave, self-Raman solid-state laser operating in the visible," Optics Express **18**, 20013–20018 (2010). 2, 98

[13] P. Dekker, H. M. Pask, D. J. Spence, and J. A. Piper, "Continuous-wave, intracavity doubled, self-Raman laser operation in Nd:$GdVO_4$ at 586.5 nm," Optics Express **15**, 7038–7046 (2007).

[14] R. P. Mildren, H. M. Pask, H. Ogilvy, and J. A. Piper, "Discretely tunable, all-solid-state laser in the green, yellow, and red," Optics Letters **30**, 1500–1502 (2005). 2

[15] Y. Lu, X. Zhang, S. Li, J. Xia, W. Cheng, and Z. Xiong, "All-solid-state cw sodium D_2 resonance radiation based on intracavity frequency-doubled self-raman laser operation in double-end diffusion-bonded Nd^{3+}:$LuVO_4$ crystal," Optics Letters **35**, 2964–2966 (2010). 3

[16] L. Fan, Y. X. Fan, Y. Q. Li, H. Zhang, Q. Wang, J. Wang, , and H. T. Wang, "High-efficiency continuous-wave Raman conversion with a $BaWO_4$ Raman crystal," Optics Letters **34**, 1687–1689 (2009). 3

[17] L. Fan, Y. X. Fan, Y. H. Duan, Q. Wang, H. T. Wang, G. H. Jia, and C. Y. Tu, "Continuous-wave intracavity Raman laser at 1179.5 nm with $SrWO_4$ Raman crystal in diode-end-pumped Nd:YVO_4 laser," Applied Physics B **94**, 553–557 (2009).

[18] V. A. Orlovich, V. N. Burakevich, A. S. Grabtchikov, V. A. Lisinetskii, A. A. Demidovich, H. J. Eichler, and P. Y. Turpin, "Continuous-wave intracavity Raman generation in $PbWO_4$ crystal in the Nd:YVO_4 laser," Laser Physics Letters **3**, 71–74 (2005). 3

[19] P. Dekker, H. M. Pask, and J. A. Piper, "All-solid-state 704 mw continuous-wave yellow source based on an intracavity, frequency-doubled crystalline Raman laser," Optics Letters **32**, 1114–1116 (2007). 3

[20] A. J. Lee, H. M. P. J. A. Piper, H. Zhang, and J. Wang, "An intracavity, frequency-doubled $BaWO_4$ Raman laser generating multi-watt continuous-wave, yellow emission," Optics Express **18**, 5984–5992 (2010).

[21] F. G. Yang, Z. Y. You, Z. J. Zhu, Y. Wang, J. F. Li, and C. Y. Tu, "End-pumped continuous-wave intracavity yellow Raman laser at 590 nm with $SrWO_4$ Raman crystal," Laser Physics Letters **7**, 14–16 (2010). 3

[22] A. J. Lee, H. M. Pask, D. J. Spence, and J. A. Piper, "Efficient 5.3 W cw laser at 559 nm by intracavity frequency summation of fundamental and first-Stokes wavelengths in a self-Raman Nd:$GdVO_4$ laser," Optics Letters **35**, 682–684 (2010). 3

[23] H. M. Pask, "The design and operation of solid-state Raman lasers," Progress in Quantum Electronics **27**, 3–56 (2003). 3, 5

[24] A. S. Grabtchikov, V. A. Lisinetskii, V. A. Orlovich, M. Schmitt, R. Maksimenka, and W. Kiefer, "Multimode pumped continuous-wave solid-state Raman laser," Optics Letters **29**, 2524–2526 (2004). 4, 5, 41

[25] V. A. Lisinetskii, A. S. Grabtchikov, P. A. Apanasevich, M. Schmitt, B. Kuschner, S. Schlucker, and V. A. Orlovich, "Continuous-wave solid-state Raman laser for spectroscopic applications," Journal of Raman Spectroscopy **37**, 421–428 (2006). 4, 5, 56

[26] H. Rong, R. Jones, A. Liu, O. Cohen, D. Hak, A. Fang, and M. Paniccia, "A continuous-wave Raman silicon laser," Letters to Nature **433**, 725–728 (2005). 4, 79, 92

[27] J. K. Brasseur, K. S. Repasky, and J. L. Carlsten, "Continuous-wave raman laser in H_2," Optics Letters **23**, 367–369 (1998). 4, 92

[28] K. S. Repasky, L. Meng, J. K. Brasseur, and J. L. Carlsten, "High-efciency, continuous-wave Raman lasers," Journal of the Optical Society of America B **16**, 717–721 (1999). 56

[29] J. K. Brasseur, R. F. Teehan, P. A. Roos, B. Soucy, D. K. Neumann, and J. L. Carlsten, "High-power deuterium Raman laser at 632 nm," Applied Optics **43**, 1162–1166 (2004). 4

[30] P. A. Roos, J. K. Brasseur, and J. L. Carlsten, "Diode-pumped nonresonant continuous-wave Raman laser in H_2 with resonant optical feedback stabilization," Optics Letters **24**, 1130–1132 (1999). 4

[31] J. T. Green, D. E. Sikes, and D. D. Yavuz, "Continuous-wave high-power rotational Raman generation in molecular deuterium," Optics Express **34**, 2563–2565 (2009). 4

[32] V. R. Supradeepa and J. W. Nicholson, "Power scaling of high-efficiency 1.5 μm cascaded Raman fiber lasers," Optics Letters **38**, 2538–2541 (2013). 4, 7

[33] D. Georgiev, V. P. Gapontsev, A. G. Dronov, M. Y. Vyatkin, A. B. Rulkov, S. V. Popov, and J. R. Taylor, "Watts-level frequency doubling of a narrow line linearly polarized Raman fiber laser to 589 nm," Optics Express **13**, 6772–6776 (2005). 4

[34] Y. Feng, S. Huang, A. Shirakawa, and K. Ueda, "Multiple-color cw visible lasers by frequency sum-mixing in a cascading Raman fiber laser," Optics Express **12**, 1843–1847 (2004). 4

[35] B. A. Cumberland, S. V. Popov, J. R. Taylor, O. I. Medvedkov, S. A. Vasiliev, and E. M. Dianov, "2.1 μm continuous-wave Raman laser in GeO_2 fibre," Optics Letters **32**, 1848–1850 (2007). 4

[36] F. Couny, B. J. Mangan, A. V. Sokolov, and F. Benabid, "High power 55 watts CW Raman fiber-gas-laser," at CLEO/US, No. **CTuM3** (2010). 4

[37] J. M. Dudley and J. R. Taylor, "Ten years of nonlinear optics in photonic crystal fibre," Nature Photonics **3**, 85–90 (2009). 4

[38] F. Benabid, J. C. Knight, G. Antonopoulos, and P. S. J. Russell, "Stimulated Raman scattering in hydrogen-filled hollow-core photonic crystal fiber," Science **298**, 399–402 (2002). 4

[39] H. Rong, A. Liu, R. Jones, O. Cohen, D. Hak, R. Nicolaescu, A. Fang, and M. Paniccia, "An all-silicon Raman laser," Letters to Nature **433**, 292–294 (2005). 5, 92

[40] Y. F. Chen, "Design criteria for concentration optimization in scaling diode end-pumped lasers to high powers: Influence of thermal fracture," Journal of Quantum Electronics **35**, 234–239 (1999). 5, 6, 31

[41] R. P. Mildren and J. R. Rabeau, *Optical Engeneering of Diamond* (Wiley-VCH Verlag GmbH & Co. KGaA, 2013). 5, 6, 21, 23, 25, 27, 28, 29, 30, 40, 58, 81, 88, 92

[42] R. W. Ditchburn, "Diamond as an optical material for space optics," Journal of Modern Optics **29**, 355–359 (1982). 5

[43] J. B. Hannay, "Man-made diamonds," Proceedings of the Royal Society **30**, 188 (1880). 6

[44] S. Ferro, "Synthesis of diamond," Journal of Materials Chemistry **12**, 2843–2855 (2002). 6

[45] C. V. Burton, "Artificial diamonds," Nature **72**, 397 (1905). 6

[46] F. P. Bundy, H. T. Hall, H. M. Strong, and R. H. W. Jr, "Man-made diamonds," Nature **176**, 51–55 (1955). 6

[47] R. J. Tapper, "Diamond detectors in particle physics," Reports on Progress in Physics **63**, 1273 (2000). 6

[48] R. H. G. Dammertz, A. Meier, and M. Thumm, "CVD diamond windows studied with low- and high-power millimeter waves," Plasma Science **30**, 800–807 (2002). 6

[49] R. S. Balmer, J. R. Brandon, S. L. Clewes, H. K. Dhillon, J. M. Dodson, I. Friel, P. N. Inglis, T. D. Madgwick, M. L. Markham, T. P. Mollart, N. Perkins, G. A. Scarsbrook, D. J. Twitchen, A. J. Whitehead, J. J. Wilman, and S. M. Woollard, "Chemical vapour deposition synthetic diamond: materials, technology and applications," Journal of Physics: Condensed Matter **21**, 364221 1–23 (2009). 6

[50] I. Friel, S. L. Geoghegan, D. J. Twitchen, and G. A. Scarsbrook, "Development of high quality single crystal diamond for novel laser applications," Proceeding of SPIE **7838**, 783819 (2010). 6, 21, 24, 25, 30, 39

[51] Element Six, http://www.e6cvd.com/cvd/page.jsp?pageid=373. Accessed: 2014-03-31. 6, 24, 26

[52] A. Qureshi, W. P. Kang, J. L. Davidson, and Y. Gurbuz, "Review on carbon-derived, solid-state, micro and nano sensors for electrochemical sensing applications," Diamond and Related Materials **18**, 1401–1420 (2009). 6

[53] A. Zunger, "Practical doping principles," Applied Physics Letters **83**, 57–59 (2003). 6

[54] G. Eckhardt, D. P. Bortfeld, and M. Geller, "Stimulated emission of Stokes and anit-Stokes Raman lines from diamond, calcite, and α-sulfur single crystals," Applied Physics Letters **3**, 137–138 (1963). 6

[55] S. Ghosh, I. Calizo, D. Teweldebrhan, and E. P. Pokatilov, "Extremely high thermal conductivity of graphene: Prospects for thermal management applications in nanoelectronic circuits," Applied Physics Letters **92**, 151911–151911–3 (2008). 6

[56] S. C. Tidwell, J. F. Seamans, M. S. Bowers, and A. K. Cousins, "Scaling CW diode-end-pumped Nd:YAG lasers to high average powers," IEEE Journal of Quantum Electronics **28**, 997–1009 (1992). 6, 40

[57] W. Lubeigt, G. M. Bonner, J. E. Hastie, M. D. Dawson, D. Burns, and A. J. Kemp, "Continuous-wave diamond Raman laser," Optics Letters **35**, 2994–2996 (2010). 6, 9, 97

[58] S. A. Babin, D. V. Churkin, A. E. Ismagulov, S. I. Kablukov, and E. V. Podivilov, "Spectral broadening in Raman fiber lasers," Optics Letters **31**, 3007–3009 (2006). 7

[59] A. A. Kaminskii, V. G. Ralchenko, and V. I. Konov, "Observation of stimulated raman scattering in CVD-diamond," JETP Letters **80**, 298–301 (2004). 7

[60] A. Kaminskii, R. Hemley, J. Lai, C. Yan, H. Mao, V. Ralchenko, H. Eichler, and H. Rhee, "High-order stimulated Raman scattering in CVD single crystal diamond," Laser Physics Letters **4**, 350–353 (2007). 7

[61] R. P. Mildren, J. E. Butler, and J. R. Rabeau, "CVD-diamond external cavity Raman laser at 573 nm," Optics Express **16**, 1895–18955 (2008). 7

[62] R. P. Mildren and A. Sabella, "Highly efficient diamond Raman laser," Optics Letters **34**, 2811–2813 (2009). 7

[63] A. Sabella, J. A. Piper, and R. P. Mildren, "1240 nm diamond Raman laser operating near the quantum limit," Optics Letters **35**, 3874–3876 (2010). 7, 27, 37, 63, 66, 67, 73

[64] W. Lubeigt, G. M. Bonner, J. E. Hastie, M. D. Dawson, D. Burns, , and A. J. Kemp, "An intra-cavity Raman Laser using Synthetic Single-crystal Diamond," Optics Express **18**, 16765–16770 (2010). 8, 30, 97

[65] A. Sabella, J. A. Piper, and R. P. Mildren, "Efficient conversion of a 1.064 μm Nd:YAG laser to the eye-safe region using a diamond Raman laser," Optics Express **19**, 23554–23560 (2011). 8

[66] M. Jelinek, O. Kitzler, H. Jelinkova, J. Sulc, M. Nemec, and V. Kubecek, "CVD-diamond external cavity Raman laser operating at 1632 nm," at CLEO Pacific Rim, Sydney, NSW, Australia (2011). 8

[67] A. Sabella, J. A. Piper, and R. P. Mildren, "Mid-infrared diamond raman laser with tuneable output," at SPIE, San Francisco, California, United States (2014). 8

[68] E. Granados, D. J. Spence, and R. P. Mildren, "Deep ultraviolet diamond Raman laser," Optics Express **19**, 10857–10863 (2011). 8, 98

[69] D. J. Spence, E. Granados, and R. P. Mildren, "Mode-locked picosecond diamond Raman laser," Optics Letters **35**, 556–558 (2010). 8

[70] J. P. M. Feve, K. E. Shortoff, M. J. Bohn, and J. K. Brasseur, "High average power diamond Raman laser," Optics Express **19**, 913–922 (2011). 8, 29

[71] J. P. M. Feve, M. J. Bohn, J. K. Brasseur, and K. Shortoff, "High power Raman diamond laser," Proceeding of SPIE **7912**, 79121P (2011). 8

[72] A. McKay, H. Liu, O. Kitzler, and R. P. Mildren, "An efficient 14.5 W diamond Raman laser at high pulse repetition rate with first (1240 nm) and second (1485 nm) Stokes output," Laser Physics Letters **10**, 105801 (2013). 8

[73] D. C. Parrotta, A. J. Kemp, M. D. Dawson, and J. E. Hastie, "Tunable continuous-wave diamond Raman laser," Optics Express **19**, 24165–24170 (2011). 9, 97

[74] V. G. Savitski, J. E. Hastie, M. D. Dawson, D. Burns, and A. J. Kemp, "Multi-watt continuous-wave diamond Raman laser at 1217 nm," at CLEO/Europe and EQEC, Munich, Germany, No. **PDA.2** (2011). 9, 97

[75] V. G. Savitski, I. Friel, J. E. Hastie, M. D. Dawson, D. Burns, and A. J. Kemp, "Characterization of single-crystal synthetic diamond for multi-watt continuous-wave Raman lasers," IEEE Journal of Quantum Electronics **48**, 328–337 (2012). 9, 30, 41

[76] C. V. Raman, "On the molecular scattering of light in water and the colour of the sea," Proceedings of the Royal Society A **11**, 64–80 (1922). 11

[77] A. Smekal, "The quantum theory of dispersion," Naturwissenschaften **11**, 873 (1923). 11

[78] C. V. Raman and K. S. Krishnan, "A new class of spectra due to secondary radiation," Nature **121**, 501 (1928). 11

[79] G. Placzek, *Rayleigh-Streuung und Raman-Effekt* (Academische-Verlag: Leipzig, Germany, 1934). 11, 17

[80] T. H. Maiman, "Stimulated optical radiation in ruby," Nature **187**, 493 (1960). 11

[81] E. J. Woodbury and W. K. Ng, "Ruby laser operation in the near IR," Proceeding of the IRE **50**, 2367 (1962). 11

[82] R. W. Boyd, *Nonlinear Optics* (Acad. Press, 2003). 11, 17

[83] R. Loudon, "Theory of stimulated Raman scattering from lattice vibrations," Proceedings of the Physical Society **82**, 393–400 (1963). 14

[84] R. Loudon, "The Raman effect in crystals," Advances in Physics **13**, 423–482 (1964). 14, 22, 26, 63, 64

[85] R. L. Sutherland, *Handbook of Nonlinear Optic* (CRC Press, 2003). 18

[86] R. C. Powell, *Physics of Solid-State Laser Materials* (Springer, 1998). 19

[87] D. E. Sands, *Introduction to Crystallography* (Courier Dover Publications, 1993). 22

[88] R. J. D. Tilley, *Crystals and Crystal Structures* (John Wiley & Sons, 2006). 23

[89] D. H. Goldstein, "Mueller matrix dual rotating retarder polarimeter," Applied Optics **31**, 6676–6683 (1992). 26, 66

[90] P. A. Williams, A. H. Rose, and C. M. Wang, "Rotating-polarizer polarimeter for accurate retardance measurement," Applied Optics **36**, 6466–6472 (1997). 26, 66

[91] V. G. Savitski, D. Burns, and A. J. Kemp, "Low-loss synthetic single-crystal diamond: Raman gain measurement and high power Raman laser at 1240 nm," at CLEO/Europe and EQEC, Munich, Germany, No. **CA12.2** (2011). 27, 97

[92] V. G. Savitski, S. Reilly, and A. J. Kemp, "Steady-state Raman gain in diamond as a function of pump wavelength," IEEE Journal of Quantum Electronics **49**, 218–223 (2013). 29, 58

[93] A. K. McQuillan, W. R. L. Clements, and B. P. Stoicheff, "Stimulated Raman emission in diamond: Spectrum, gain, and angular distribution of intensity," Physical Review A. **1**, 628 (1970). 27

[94] F. C. Waldermann, B. J. Sussman, J. Nunn, V. O. Lorenz, K. C. Lee, K. Surmacz, K. H. Lee, D. Jaksch, I. A. Walmsley, P. Spizziri, P. Olivero, and S. Prawer, "Measuring phonon dephasing with ultrafast pulses using Raman spectral interference," Physical Review B **78**, 155201 1–6 (2008). 27, 44, 81

[95] A. J. Kemp, P. Millar, W. Lubeigt, J. E. Hastie, M. D. Dawson, and D. Burns, "Diamond in solid-state disk lasers: Thermal management and CW Raman generation," at Advanced Solid-State Photonics, Denver, Colorado United States, No. **WE7** (2009). 39, 97

[96] H. M. Pask, S. Myers, J. A. Piper, J. Richards, and T. McKay, "High average power, all-solid-state external resonator Raman laser," Optics Letters **28**, 435–437 (2003). 39

[97] V. Lisinetskii, T. Riesbeck, H. Rhee, H. Eichler, and V. Orlovich, "High average power generation in barium nitrate Raman laser," Applied Physics B **99**, 127–134 (2010).

[98] A. McKay, O. Kitzler, and R. P. Mildren, "Thermal lens evolution and compensation in a high power KGW Raman laser," Optics Express **22**, 6707–6718 (2014). 39, 44

[99] M. S. Liu, L. A. Bursil, and S. Prawer, "Temperature dependence of the first-order Raman phonon line of diamond," Physical Review B **61**, 3391–3395 (2000). 40

[100] J. C. Bienfang, W. Rudolph, P. A. Roos, L. S. Meng, and J. L. Carlsten, "Steady-state thermo-optic model of a continuous-wave raman laser," Journal of the Optical Society of America B **19**, 1318–1325 (2002). 40, 56

[101] D. Ran, H. Xia, S. Sun, P. Zhao, F. Liu, Z. Ling, W. Ge, H. Zhang, and J. Wang, "Optical phonon modes and transmissivity in $BaWO_4$ single crystal," Crystal Research and Technology **41**, 1189–1193 (2006). 41

[102] H. Zhanga, X. Menga, L. Zhua, and Z. Yanga, "Growth and thermal properties of Nd:$GdVO_4$ single crystal," Materials Research Bulletin **34**, 1589–1593 (1999). 41

[103] M. Frede, R. Wilhelm, M. Brendel, C. Fallnich, F. Seifert, B. Willke, and K. Danzmann, "High power fundamental mode Nd:YAG laser with efficient birefringence compensation," Optics Express **12**, 3581–3589 (2004). 42

[104] N. Kugler, S. Dong, Q. Lu, and H. Weber, "Investigation of misalignment sensitivity of a birefringence-compensated two-rod Nd:YAG laser system," Applied Optics **36**, 9359–9366 (1997). 42

[105] S. Konno, S. Fujikawa, and K. Yasui, "80 W TEM_{00} 1064 nm beam generation by use of a laser-diode-side-pumped Nd:YAG rod laser," Applied Physics Letters **70**, 2650–2651 (1997). 44

[106] Y. T. Xu, J. L. Xu, Y. D. Guo, F. T. Yang, Y. Z. Chen, J. Xu, S. Y. Xie, Y. Bo, Q. J. Peng, D. Cui, and Z. Y. Xu, "Compact high-efficiency 100-W-level diode-side-pumped Nd:YAG laser with linearly polarized TEM_{00} mode output," Applied Optics **49**, 4576–4580 (2010). 44

[107] G. D. Boyd, W. D. Johnston, and I. P. Kaminow, "Optimization of the stimulated Raman scattering threshold," Journal of Quantum Electronics **5**, 203–206 (1969). 51, 53, 54, 56

[108] S. Ding, X. Zhang, Q. Wang, F. Su, S. Li, S. Fan, S. Zhang, J. Chang, S. Wang, and Y. Liu, "Theoretical models for the extracavity Raman laser with crystalline Raman medium," Applied Physics B **85**, 89–95 (2006). 56

[109] D. J. Spence, P. Dekker, and H. M. Pask, "Modeling of continuous wave intravcavity Raman lasers," IEEE Journal of Selected Topics in Quantum Electronics **13**, 756–763 (2007). 56

[110] K. S. Repasky, J. K. Brasseur, L. Meng, and J. L. Carlsten, "Performance and design of an off-resonant continuous-wave Raman laser," Journal of the Optical Society of America B **15**, 1667–1673 (1998). 56

[111] P. Peterson, A. Gavrielides, and M. P. Sharma, "Modeling of high finesse, doubly resonant cw Raman lasers," Optics Communications **160**, 80–85 (1999). 56

[112] E. Hecht, *Optics* (Addison-Wesley Longman, Inc., 2002). 63

[113] B. E. Saleh and M. C. Teich, *Fundamentals of Photonics* (John Wilet & Sons, INC., 1991). 72

[114] R. G. Harrison and D. J. Biswas, "Demonstration of self-pulsing instability and transition to chaos in single-mode and multimode homogeneously broadened Raman laser," Physical Review Letters **55**, 63–66 (1985). 79

[115] A. T. Georges and S. N. Dixit, "Dependence of broadband Raman amplification in dispersive media on the pump–Stokes input correlation," Journal of the Optical Society of America B **8**, 780–785 (1991). 79, 80

[116] M. G. Raymer, J. Mostowski, and J. L. Carlsten, "Theory of stimulated Raman scattering with broad-band lasers," Physical Review A **19**, 2304–2316 (1979). 80, 81

[117] V. V. Bocharov, A. Z..Grasyuk, I. G. Zubarev, and V. K. Mulikov, "Stimulated Raman scattering of neodymium laser radiation in liquid nitrogen," Soviet Physics JETP **29**, 235–237 (1969). 80

[118] W. R. Trutna, Y. K. Park, and R. L. Byer, "The dependence of Raman gain on pump laser bandwidth," IEEE Journal of Quantum Electronics **15**, 648–655 (1979). 80, 81

[119] A. T. Georges, "Statistical theory of Raman amplification and spontaneous generation in dispersive media pumped with a broadband laser," Physical Review A **39**, 1879–1886 (1989). 80, 81

[120] J. Lin, *Private communication* (MQ Photonics Research Centre, Macquarie Univeristy, Sydeny NSW 2109, Australia, 2014). 87

[121] M. H. Grimsditch and A. K. Ramdas, "Brillouin scattering in diamond," Physical Review B **11**, 3139–3148 (1975). 88

[122] N. Bloembergen and Y. R. Shen, "Multimode effects in stimulated Raman emission," Physical Review Letters **13**, 720–724 (1964). 93

[123] D. C. Parrotta, A. J. Kemp, M. D. Dawson, and J. E. Hastie, "Multiwatt, continuous-wave, tunable diamond Raman laser with intracavity frequency-doubling to the visible region," Selected Topics in Quantum Electronics **19**, 1400108 (2013). 97, 98

[124] R. Royon, J. Lhermite, L. Sarger, and E. Cormier, "High power, continuous-wave ytterbium-doped fiber laser tunable from 976 to 1120 nm," Optics Express **21**, 13818–13823 (2013). 98

[125] R. P. Mildren, J. E. Downes, J. D. Brown, B. F. Johnston, E. Granados, D. J. Spence, A. Lehmann, L. Weston, and A. Bramble, "Characteristics of 2-photon ultraviolet laser etching of diamond," Optical Materials Express **1**, 576–585 (2011). 98

[126] H. M. Pask, P. Dekker, R. P. Mildren, D. J. Spence, and J. Piper, "Wavelength-versatile visible and UV sources based on crystalline Raman lasers," Progress in Quantum Electronics **32**, 121–158 (2008). 98